Cosmology from Secondary Anisotropies of the Cosmic Microwave Background

Blake Daniel Sherwin

A Dissertation
Presented to the Faculty
of Princeton University
in Candidacy for the Degree
of Doctor of Philosophy

Recommended for Acceptance
by the Department of
Physics
Adviser: Prof. David N. Spergel

September 2013

Abstract

Gravitational lensing and the Sunyaev-Zel'dovich effect introduce new intensity fluctuations, known as secondary anisotropies, into the cosmic microwave background radiation (CMB). These CMB secondary anisotropies encode a wealth of information about the distribution of dark matter and gas throughout our universe. In this thesis, we present novel measurements of CMB lensing and the Sunyaev-Zel'dovich effect in the microwave background and use them to place new constraints on cosmology.

In an early thesis chapter, we describe the first detection of the power spectrum of gravitational lensing of the CMB. The power spectrum is detected at a four sigma significance through a measurement of the four-point correlation function of Atacama Cosmology Telescope (ACT) CMB temperature maps. This first detection gravitationally probes the amplitude of large-scale structure at redshifts $\approx 1-3$ to 12% accuracy, and lies at the beginning of an exciting new field of science with the lensing power spectrum.

From this measurement of the CMB lensing power spectrum we extract first cosmological constraints. We explain in detail how the amount of dark energy in our universe affects the amplitude of the lensing signal by modifying both the geometry of the universe and the growth of structure. We then demonstrate that our lensing measurements provide, for the first time, evidence for the existence of dark energy from the CMB alone, at a 3.2 sigma significance.

We use CMB lensing measurements to study the relation of quasars to the underlying distribution of dark matter. Detecting the cross-power of CMB lensing with the spatial distribution of quasars and hence measuring the quasar bias to within 25%, we obtain a measurement of the characteristic dark matter halo mass of these objects.

CMB lensing power spectrum measurements typically require the subtraction of a simulated bias term, which complicates the analysis; we develop new techniques to obviate this bias subtraction.

Finally, we develop a novel method for measuring the Sunyaev-Zel'dovich effect through the skewness it induces in CMB temperature maps. Detecting this skewness in ACT CMB maps for the first time at five sigma significance, we demonstrate how this novel measurement constrains the amplitude of structure in our universe to within 4%.

Acknowledgements

First and foremost, I would like to thank my adviser David Spergel, as I owe nearly all my scientific achievements to his guidance and teaching. It has been a joy and a great privilege to work with him over the last few years.

I have been fortunate to collaborate with truly outstanding scientists. In particular, Sudeep Das has served as a second advisor for me in our continuing collaboration on CMB lensing and has also been responsible for much of my success. I am grateful to Matias Zaldarriaga for an interesting collaboration, for much helpful advice, and for agreeing to be a reader for my thesis. I thank Lyman Page, Jo Dunkley and everyone working on ACT for interesting and successful research collaborations as well as general advice. I thank Suzanne Staggs for collaboration and for advising my experimental project. I am also grateful to Bill Jones and Igor Klebanov for agreeing to serve on my thesis committee.

Before coming to Princeton, my interest in physics and cosmology was encouraged by a number of excellent teachers and scientists, such as Elizabeth Parr, Helmut Kuehnberger, Mike Hobson, John Kirk, Donald Lynden-Bell and Avi Loeb, and I thank them for their teaching and inspiration.

I am grateful to my friends for making graduate school enjoyable even when work was stressful. I would like to thank David McGady for his friendship and for his ability to tolerate me as an apartment-mate – not always an easy task – and am similarly grateful to Guilherme Pimentel, Halil Saka and Colin Hill (who also belongs in the outstanding collaborators paragraph). I would also like to thank Katrina Jones, Anushya Chandran, Michael Mooney, Eduardo da Silva Neto, Leah Klement, Eaming Wu and Matt Johnson for friendship and some great times.

I thank Maryam Patton for her love and encouragement, which have made the last few years some of the best of my life. Any success I have had in graduate school would not have been possible without her support.

Finally, I would like to thank my family. I am truly fortunate to have parents and a sister who have always encouraged me in my academic pursuits, no matter how obscure they may have seemed to them, and have always believed in me as a scientist and as a person. Without their support in difficult times and the knowledge that I always have a loving family to fall back on, I wouldn't have achieved much at all, let alone written a Ph.D. thesis in Physics.

In memory of my friend Arunn Mahakuperan

Relation to Published Work

This thesis consists of seven chapters. The first two chapters are introductory and summarize relevant past research on CMB secondary anisotropies; in these chapters, I thus claim originality only in the details of exposition.

The central part of this thesis is formed by chapters three through seven. These chapters have, in slightly modified form, either been published in or submitted to peer reviewed journals. I will here note the publication or submission status of each chapter. As all the projects listed here were completed as part of a research collaboration, I will also attempt to describe my own contribution to each of the chapters.

Chapter 3: Detection of the Power Spectrum of CMB Lensing with the Atacama Cosmology Telescope

Das, S., Sherwin, B. D., et al. 2011, Physical Review Letters., 112, 021301; the appendix is from Das, S. et al. 2013, arXiv:1301.1037, Journal of Cosmology and Astroparticle Physics submitted

The work described in this chapter was performed mainly by Sudeep Das and myself under the guidance of David Spergel, though it relied crucially on data taken by the Atacama Cosmology Telescope collaboration (of which I am a part). I wrote most of the core computational pipeline that performs the lensing reconstruction from high-resolution temperature maps under the guidance of Sudeep Das. I also developed and ran many of the required null and systematic tests in this paper.

Sudeep Das and I made equal contributions to the development of codes to calculate errors and biases and to compile the final results. The text was written by myself, David Spergel and Sudeep Das. The updated lensing power spectrum calculation from the new dataset and the text in the addendum to the chapter is my work, though it relies on older jointly-developed codes.

Chapter 4: Evidence for Dark Energy from the CMB Alone Using ACT Lensing Measurements

Sherwin, B. D., Dunkley, J., Das, S., et al. 2011, Physical Review Letters, 112, 021302

The work described in this chapter was performed mainly by myself, Joanna Dunkley and Sudeep Das, relying again on data from the Atacama Cosmology Telescope collaboration. I developed and tested the final form for the likelihood with Joanna Dunkley, processed and analyzed the chains, and calculated the cosmological constraints described in this paper. I also developed and tested the physical explanations of how lensing constrains dark energy, and wrote the text of the chapter. The lensing measurements underlying these results, made by Sudeep Das, myself, and others, are described in Chapter 2.

Chapter 5: Cross-correlation of CMB Lensing with the Distribution of Quasars

Sherwin, B. D., Das, S., Hajian, A. et al. 2012, Physical Review D, 86, 083006

Nearly all the results and text described in this section are my own work, under the guidance of David Spergel, though the lensing measurement again relies on data from the Atacama Cosmology Telescope, Amir Hajian constructed the quasar maps from the SDSS catalog, and Sudeep Das contributed tests of my theory curve calculation.

Chapter 6: CMB Lensing: Power Without Bias

Sherwin, B. D., & Das, S. 2010, arXiv:1011.4510

The idea for this chapter arose from conversations with Sudeep Das. I worked out the details of the no-bias method presented here, including the expansion formalism, with input from Sudeep Das and guidance from David Spergel. The testing of the method on simulations was joint work with Sudeep Das.

Chapter 7: A Measurement of the Skewness of the Thermal Sunyaev-Zeldovich Effect

Wilson, M. J., Sherwin, B. D., et al. 2012, Physical Review D, 86, 122005

This final chapter was a joint effort between Michael Wilson (an undergraduate whom I advised), myself, and Colin Hill. I developed the idea for this project and supervised Michael Wilson's work in great detail. I wrote my own codes and verified all the results Michael Wilson obtained prior to publication. I also generated the required simulations of the observed full CMB sky, relying on Sunyaev-Zel'dovich simulations by Nick Battaglia. I wrote most of the text for this chapter/publication, with contributions and editing from Colin Hill.

Appendix A: Lensing Simulation and Power Spectrum Estimation for High Resolution CMB Polarization Maps

Louis, T., Naess, S., Das, S., Dunkley, J., Sherwin, B., 2013, arXiv:1306.6692

This project was lead by Thibaut Louis and Sigurd Naess (and is hence relegated to an appendix), though I contributed to the paper: Thibaut and I independently performed all the derivations of the expressions in section A.3, and I helped develop the new method for simulating polarized lensing rapidly. In addition, the code which inverts the mode-coupling matrix is based on my work on the ACT temperature power spectrum pipeline.

Contents

Abstract iii

Acknowledgements v

Relation to Published Work viii

List of Tables xv

List of Figures xvi

1 Introduction **1**

1.1 CMB Secondary Anisotropies as a New Source of Cosmological Information 1

1.2 Overview of this Thesis 5

2 Brief Review of CMB Lensing Reconstruction Theory **8**

2.1 Lensing of the CMB 8

2.2 Lensing Reconstruction 11

3 Detection of the Power Spectrum of CMB Lensing with the Atacama Cosmology Telescope **17**

3.1 Abstract 17

3.2 Introduction 18

3.3 Data 18

3.4 Methods 19

3.5 Simulations 21

3.6 Results . . . 22
3.7 Null Tests . . . 25
3.8 Implications and Conclusions . . . 26
3.9 Acknowledgements . . . 26
3.10 Addendum: Updated Measurement of the Lensing Power Spectrum from Three Seasons of Data . . . 27

4 Evidence for Dark Energy from the CMB Alone Using ACT Lensing Measurements 33

4.1 Abstract . . . 33
4.2 Introduction . . . 34
4.3 Methodology . . . 39
4.4 Results . . . 40
4.5 Conclusions . . . 41
4.6 Acknowledgements . . . 42

5 Cross-correlation of CMB Lensing with the Distribution of Quasars 46

5.1 Abstract . . . 46
5.2 Introduction . . . 47
5.3 Theoretical Background . . . 48
5.4 Cross-correlating CMB Lensing and Quasars . . . 50
5.4.1 The ACT CMB Lensing Convergence Maps . . . 50
5.4.2 The SDSS Quasar Maps . . . 52
5.4.3 The CMB Lensing - Quasar Cross-Power Spectrum . . . 53
5.5 A Constraint on the Quasar Bias . . . 56
5.6 Testing the power spectrum . . . 58
5.6.1 Null Tests . . . 58
5.6.2 Estimating Potential Systematic Contamination . . . 58

5.7 Summary and Conclusions 61
5.8 Acknowledgements 62

6 CMB Lensing: Power Without Bias **67**
6.1 Abstract 67
6.2 Bias-free Lensing Power Spectrum Measurements 68
6.3 Acknowledgements 76

7 A Measurement of the Skewness of the Thermal Sunyaev-Zeldovich Effect **79**
7.1 Abstract 79
7.2 Introduction 80
7.3 Skewness of the tSZ Effect 83
7.4 Map Processing 87
7.4.1 Filtering the Maps 87
7.4.2 Removing Point Sources 88
7.5 Results 90
7.5.1 Evaluating the Skewness 90
7.5.2 The Origin of the Signal 92
7.5.3 Testing for Systematic Infrared Source Contamination 95
7.6 Cosmological Interpretation 97
7.7 Conclusions 101
7.8 Acknowledgements 101

A Lensing Simulation and Power Spectrum Estimation for High Resolution CMB Polarization Maps **106**
A.1 Abstract 106
A.2 Introduction 107
A.3 E/B leakage in the flat sky approximation 108

A.3.1 Notation 108
A.3.2 Partial sky coverage 110
A.3.3 Pure estimators 111
A.4 Generating gravitationally lensed simulations 113
A.5 Implementation on realistic observations 117
A.5.1 Estimated power spectra 118
A.5.2 Power spectrum uncertainties 120
A.6 Conclusions 121
A.7 Acknowledgements 123
A.8 Error Calculation 123

B Methods for CMB Lensing Estimation without Sensitivity to Foregrounds 127

B.1 Lensing Biases from Foregrounds 127
B.2 Immunizing the Lensing Estimator to Foreground Contamination . . 128
B.2.1 Poisson Foregrounds 128
B.2.2 General Foregrounds 131

List of Tables

3.1 Reconstructed $C_\ell^{\kappa\kappa}$ values. 24

7.1 Constraints on σ_8 derived from our skewness measurement using two different simulations and three different scalings of the skewness and its variance with σ_8. The top row lists the simulations used to calculate the expected skewness for $\sigma_8 = 0.8$ [35, 33]; the left column lists the pressure profiles used to calculate the scaling of the skewness and its variance with σ_8 [16, 17, 25]. The errors on σ_8 shown are the 68% and 95% confidence levels. 100

List of Figures

3.1 Mean convergence power spectrum (red points) from 480 simulated lensed maps with noise similar to our data. The solid line is the input lensing power spectrum, taken from the best-fit WMAP+ACT cosmological model. Error bars correspond to the scatter of power spectrum values obtained from individual maps. 22

3.2 Convergence power spectrum (red points) measured from ACT equatorial sky patches. The solid line is the power spectrum from the best-fit WMAP+ACT cosmological model with amplitude $A_L = 1$, which is consistent with the measured points. The error bars are from the Monte Carlo simulation results displayed in Fig. 3.1. The best-fit lensing power spectrum amplitude to our data is $A_L = 1.16 \pm 0.29$. 23

3.3 Convergence power spectrum for simulated thermal and kinematic SZ maps and point source maps [1] which are a good fit to the ACT data. Note that we only show the non-Gaussian contribution, as the Gaussian part which is of similar negligible size is automatically included in the subtracted bias generated by phase randomization. The solid line is the convergence power spectrum due to lensing in the best-fit WMAP+ACT cosmological model. 24

3.4 *Upper panel:* Mean cross-correlation power spectrum of convergence fields reconstructed from different sky patches. The result is consistent with null, as expected. *Lower panel:* Mean convergence power spectrum of noise maps constructed from the difference of half-season patches, which is consistent with a null signal. The error bars in either case are determined from Monte Carlo simulations, and those in the lower panel are much smaller as they do not contain cosmic variance. 25

3.5 CMB convergence power spectrum reconstructed from the ACT equatorial strip temperature data. The enhanced effective depth of the three-season coadded ACT equatorial map ($\simeq 18\,\mu$k-arcmin) compared to its previous version as described previously ($\simeq 23\ \mu$k-arcmin) leads to an improved detection significance. 28

4.1 Upper panel: Angular power spectra of CMB temperature fluctuations for two geometrically degenerate cosmological models, one the best-fit curved universe with no vacuum energy ($\Omega_\Lambda = 0, \Omega_m = 1.29$), and one the best-fit flat ΛCDM model with $\Omega_\Lambda = 0.73, \Omega_m = 0.27$. The seven-year WMAP temperature power spectrum data [24] are also shown; they do not significantly favor either model. Lower panel: The CMB lensing deflection power spectra are shown for the same two models. They are no longer degenerate: the $\Omega_\Lambda = 0$ universe would produce a lensing power spectrum larger than that measured by ACT ([7], also shown above). 36

4.2 Different terms in the kernel of the lensing integral of Eq. 4.1 as a function of conformal lookback distance for $\ell = 120$, for models as in Fig. 4.1. Upper panel: geometry term. Middle panel: growth term, scaled to its value at decoupling for clarity. Bottom panel: total kernel. 38

4.3 Two-dimensional marginalized posterior probability for Ω_m and Ω_Λ (68% and 95% C.L.s shown). Colored contours are for WMAP + ACT Lensing, black lines are for WMAP only. Using WMAP data alone, universes with $\Omega_\Lambda = 0$ lie within the 95% C.L. The addition of lensing data breaks the degeneracy, favoring models with dark energy. . . . 41

4.4 One-dimensional marginalized posterior probability for Ω_Λ (not normalized). An energy density of $\Omega_\Lambda \simeq 0.7$ is preferred even from WMAP alone, but when lensing data are included, an $\Omega_\Lambda = 0$ universe is strongly disfavoured. 42

5.1 The redshift distribution of SDSS quasars used to construct our maps of fractional quasar overdensity, normalized to a unit maximum. The corresponding redshift bins are shown with blue filled circles; they are interpolated to give the continuous curve used in our theory calculations (blue dashed line). For comparison, the red dotted line shows the lensing kernel $W^\kappa(z)$, again normalized to a unit maximum. 52

5.2 The CMB lensing - quasar density cross-power spectrum, with the data points shown in blue (the covariance between different data points is negligible). The significance of the detection of the cross-spectrum is 3.8σ. The green solid line is a theory line calculated assuming the fiducial bias amplitude. This theory line is reduced by 6% to account for the expected level of stellar contamination of the quasar sample. . 54

5.3 Blue dashed line: fiducial quasar bias template (interpolated from the data points of [31]), used in the theoretical calculation of the CMB lensing - quasar cross-power spectrum. Red solid line: the bias amplitude ($b/b_{\rm fid} = 1.02$) best fit by the measured cross-power spectrum; red dashed lines: the $\pm 1\sigma$ error ranges of this amplitude. Note that only one degree of freedom is constrained: the overall bias amplitude of an assumed redshift evolution. 55

5.4 Likelihood as a function of quasar bias divided by the fiducial bias, $b/b_{\rm fid}$ (we assume that the shape of the redshift dependence is constant and has the fiducial form of Fig. 3, and modify the amplitude of the bias function to calculate this likelihood.) Interpreting our measurement of $b/b_{\rm fid} = 1.02 \pm 0.24$ as a bias at $z \approx 1.4$ (the peak in the quasar distribution), we obtain $b = 2.5 \pm 0.6$ at this redshift. 57

5.5 Two successful null tests, both consistent with zero. Upper panel: the cross-power spectrum of quasar and lensing maps covering different parts of the sky (permutation null test). Lower panel: the cross-power spectrum of the reconstructed curl component of the lensing signal with the quasar maps (curl null test). 59

6.1 Graphical expansion of the naive estimator after splitting up the Fourier space into an inner and an outer annulus. We use the linearity of both operators in this expansion. The terms with Gaussian bias are shown enclosed by boxes. The underlined terms (identical by symmetry) are implemented in the simulations described in this paper to illustrate the method. 71

6.2 *Upper image:* Convergence power spectrum reconstructed with the proposed Gaussian bias-free method from four $5^\circ \times 15^\circ$ patches with simulated CMB signal with 2 μK-arcmin white noise. The blue (filled) circles show the mean of 120 Monte Carlo realizations with lensed CMB, while the green (empty) circles show the same for unlensed CMB maps. The error bars are estimated from the scatter between Monte Carlo runs and are representative of the uncertainty expected in one realization; the lensed errors are higher than the null errors due to the presence of a sample variance component. The red continuous curve is the input theory for the convergence field power spectrum. *Lower image:* Same as left, but for non-white and anisotropic noise simulations seeded by noise in ACT maps, reduced in amplitude by a factor of 3. 77

7.1 The Wiener filter applied to the ACT temperature maps before calculating the unnormalized skewness. This filter upweights scales on which the tSZ signal is large compared to other sources of anisotropy. 88

7.2 Histogram of the pixel temperature values in the filtered, masked ACT CMB temperature maps. A Gaussian curve is overlaid in red. 90

7.3 Likelihood of the skewness measurement described in the text (with Gaussian statistics assumed). 91

7.4 Plot of the skewness signal as a function of the minimum S/N of the clusters that are masked (this indicates how many known clusters are left in the data, unmasked). The blue line is calculated using the full cluster candidate catalog obtained via matched filtering, while the green line uses a catalog containing only optically-confirmed clusters [38]. Both lines have identical errors, but we only plot them for the green line for clarity. Confirmed clusters source approximately two-thirds of the signal, which provides strong evidence that it is due to the tSZ effect. Note that one expects a positive bias of $\approx 4\ \mu\mathrm{K}^3$ for the S/N = 4 point of the blue line due to impurities in the full candidate catalog masking the tail of the Gaussian distribution. 93

7.5 A test for IR source contamination: similar to the blue line in Fig. 4, but with a range of values of the cutoff used to construct an IR source mask in the 218 GHz band. Any cutoff below $\approx 3.2\sigma$ gives similarly negative results and thus appears sufficient for point source removal, where $\sigma = 10.3\ \mu$K is the standard deviation of the 148 GHz maps. For comparison, the standard deviation of the 218 GHz maps is ≈ 2.2 times larger. The percentages of the map which are removed for the masking levels shown, from the least to the most strict cut, are 0.7, 2.5, 8.4, 14.5, 23.7, and 36.6%. 94

A.1 Effect of sky cuts on the polarization pattern. A pure E-mode signal on the sky is observed through a window with a point source mask (left) leading to the estimated E-mode (centre) and B-mode (right) maps. The leaked E-modes show up as spurious signal in the B-mode map localized around the discontinuities of the window function. 111

A.2 Convergence of the Taylor series in pixel space. We represent the contribution of each higher order term of the Taylor series by showing the histogram of its pixel distribution. The convergence of the series is fast, each term being ≈ 60 times smaller than the preceding one. The contribution of the third order term is of order $10^{-1}\mu$K for T and $10^{-2}\mu$K for Q and U. 114

A.3 Convergence of the Taylor series: power spectra. We compute the temperature (TT) and polarization (EE, BB) power spectra of the series truncated at different orders. Convergence is achieved by second order in the expansion. 116

A.4 Realization of the noise, for a U and Q map (centre and right) generated using a simulated pixel weight map (left). This represents the number of observations per pixel for an inhomogeneous survey, and is taken from a simulation for the ACTPol experiment. 118

A.5 Power spectra estimated from temperature and polarization maps. This shows the average binned spectra estimated from 720 Monte Carlo simulations, with errors estimated from the 1σ dispersion. The B-mode spectra are derived using the pure estimator, to avoid leakage from the E-mode spectrum. 120

A.6 Comparison between Monte Carlo scatter and analytic errors for each cross spectrum for one of the patches. They agree at the 15 per cent level for $500 < \ell < 6000$, indicating that all sources of leakage are subdominant for these modes, The analytic estimate does not include the non-Gaussian contribution from lensing, but the noise in our simulation is high enough for this effect to be subdominant. 122

Chapter 1

Introduction

1.1 CMB Secondary Anisotropies as a New Source of Cosmological Information

A striking fact about our universe is how much of it we cannot see. More than four-fifths of the matter in our universe is not visible atomic matter, as found in gas and stars, but instead consists of dark matter, an invisible substance of unknown composition. Still more mysteriously, most of the energy in our universe is dark energy, an invisible phenomenon which causes the universe to accelerate apart, unlike normal forms of energy which cause the universe to contract through the attractive force of gravity. Invisible, poorly understood particles known as neutrinos stream through every cubic centimeter of the universe. Even most of the normal atomic matter in our universe has not yet been observed or located.

Given that it is impossible to directly see more than a few percent of the contents of our universe, the goal of studying its "dark" components in great detail seems perhaps overly ambitious. Yet advances in the study of the cosmic microwave background (CMB) – relic radiation left over from the primordial "fireball" that was the hot early universe, last scattered just 380000 years after the Big Bang – have allowed us to make

remarkable progress in this effort. Measurements of the variations of the brightness of this radiation, the so-called anisotropies in the cosmic microwave background, have allowed us (in combination with observations of the cosmic expansion history) to determine the precise amount of the universe that consists of dark matter and dark energy. Only recently, however, have we been able to use the cosmic microwave background to study the *distribution* of invisible dark matter and gas throughout the entire universe. The CMB encodes information about the cosmic distribution of dark matter and gas because large structures of matter affect the CMB radiation and introduce new patterns into the CMB brightness fluctuations, known as CMB secondary anisotropies (in contrast to the primary anisotropies, which are imprinted in the CMB very early on).

To understand how the large-scale distribution of matter and gas affects the CMB, it is helpful to consider the trajectory of CMB photons as they travel to us from the hot, distant early universe. As the universe cools, the opaque primordial plasma of electrons and protons undergoes a rapid transition, with protons capturing electrons to form transparent hydrogen gas. The photons of the CMB, which were trapped in the hot plasma, are now free to travel through the newly-transparent universe. Not everywhere is the CMB radiation equally bright: where the primordial plasma is denser, the radiation emitted is slightly brighter on small scales (this causes the primary anisotropies in the CMB brightness); the variations in brightness are tiny, at a level of only one part in a hundred thousand. For the first billion years after streaming out of the primordial plasma, the photons of the CMB travel in a straight line through the universe, without being deflected. Yet over time, the universe undergoes dramatic changes. Regions where there is initially a small overdensity in the dark matter and gas experience runaway growth, as dense regions gravitationally attract more matter and thereby become still more dense. This gravitational instability leads to the formation of immense structures of dark matter into which gas falls, thereby

forming galaxy clusters, galaxies and stars. Through their gravitational pull, these structures of dark and atomic matter deflect the CMB photons as they travel past. This effect is known as gravitational lensing. By the time a CMB photon finally reaches our telescope, it has experienced many small gravitational lensing deflections, which result in a net change in direction of typically one twentieth of a degree.

Lensing deflection is not the only effect experienced by CMB photons as they cross the cosmos. As the dark matter and gas structures grow, the gas which falls into the largest "clumps" of dark matter, known as galaxy clusters, heats up to millions of degrees Kelvin. This gas in galaxy clusters is so hot that it occasionally (inverse-Compton) scatters a low-frequency CMB photon to a higher frequency. This phenomenon is known as the Sunyaev-Zel'dovich (SZ) effect. The CMB radiation is thus "missing" low frequency photons after passing through a galaxy cluster.

How do gravitational lensing and the SZ effect modify the appearance of the cosmic microwave background sky which we observe today in CMB telescopes? As gravitational lensing merely deflects the photons of the CMB, this effect remaps and shifts the pattern of CMB anisotropies. In particular, a large dark matter structure deflects light in exactly the same way as a magnifying glass, enlarging the CMB anisotropies that lie behind it. In contrast, the SZ effect does not simply remap and magnify the original anisotropies, but introduces new brightness fluctuations; as the photons that have been scattered to higher frequencies are missed by typical experiments sensitive to a limited range of frequencies, an SZ cluster filled with hot gas appears as a "shadow" on the CMB sky.

We can use the changes gravitational lensing induces in the CMB to determine the cosmic distribution of mass. By measuring how much the anisotropies, whose unlensed characteristic size is well understood, have been magnified and stretched, we can determine the (projected) distribution of matter which is responsible for the gravitational lensing. Determining the lensing and the matter distribution in this

way is known as lensing reconstruction. Measurements of the SZ "shadows" in the CMB can similarly provide information about the distribution of matter and gas in our universe.

Such studies are of great scientific value. As the cosmic matter distribution bears the imprints of dark energy and neutrinos and drives the formation of galaxies and quasars, it encodes answers to a number of important new questions in both fundamental physics and astrophysics: What are the properties of dark energy? What are the masses of neutrinos? What is the relation between dark matter and luminous matter in stars and gas, and how do galaxies and quasars form and evolve? Similarly, studies of the SZ effect give insight into the properties of gas in galaxy clusters, the amplitude of structure in the universe, and the properties of neutrinos.

Only in the past five years have accurate CMB lensing measurements become experimentally feasible. While detections of lensing in cross-correlation were reported at moderate significance [1, 2] from WMAP satellite CMB data, newer CMB telescopes such as the Atacama Cosmology Telescope (ACT), South Pole Telescope (SPT) and Planck have now observed the CMB at higher (1-5 arcminute) resolution, which increases the sensitivity to the arcminute-scale lensing effect and hence allows an internal, higher significance detection of CMB lensing [3, 4, 5, 6, 7]. High resolution CMB measurements have also begun a new era of cluster cosmology, allowing us to discover hundreds of galaxy clusters using the SZ effect (e.g., [8]) and perform novel measurements with the statistics of the SZ signal [9, 10, 11, 12]. Yet current measurements lie only at the beginning of a promising new field. With upcoming data from new high-resolution polarization-sensitive experiments such as ACTPol, POLARBEAR and SPTpol [13, 14, 15], the ability of CMB secondary anisotropies to probe the distribution of matter in our universe and to constrain both fundamental physics and extragalactic astrophysics will continue to increase dramatically.

1.2 Overview of this Thesis

This thesis aims to contribute to the development of CMB lensing into a powerful new cosmological probe. It also introduces novel methods of extracting cosmological information from the SZ signal.

In Chapter 2 we will review the theory of CMB lensing reconstruction in technical detail. In Chapter 3, we report the first detection of the power spectrum of CMB lensing with the Atacama Cosmology Telescope (ACT). We use these CMB lensing measurements to obtain first evidence for dark energy from the CMB alone, as described in Chapter 4. In Chapter 5, we use CMB lensing measurements to calculate the bias parameters and host dark matter halo masses of high redshift quasars. In Chapter 6, we derive a new reconstruction method which can make CMB lensing measurements more robust. In Chapter 7, we introduce a novel way of studying cosmology and galaxy clusters by measuring the skewness of the Sunyaev-Zel'dovich effect in ACT CMB temperature maps.

References

[1] Smith, K. M., Zahn, O., & Doré, O. 2007, Phys. Rev. D, 76, 043510

[2] Hirata, C. M., Ho, S., Padmanabhan, N., Seljak, U., & Bahcall, N. A. 2008, Phys. Rev. D, 78, 043520

[3] Das, S., Sherwin, B. D., Aguirre, P., et al. 2011, Physical Review Letters, 107, 021301

[4] van Engelen, A., Keisler, R., Zahn, O., et al. 2012, ApJ, 756, 142

[5] Bleem, L. E., van Engelen, A., Holder, G. P., et al. 2012, ApJ, 753, L9

[6] Planck Collaboration, Ade, P. A. R., Aghanim, N., et al. 2013, arXiv:1303.5077

[7] Planck Collaboration, Ade, P. A. R., Aghanim, N., et al. 2013, arXiv:1303.5078

[8] Hasselfield, M., Hilton, M., Marriage, T. A., et al. 2013, arXiv:1301.0816

[9] Wilson, M. J., Sherwin, B. D., Hill, J. C., et al. 2012, Phys. Rev. D, 86, 122005

[10] Hill, J. C., & Sherwin, B. D. 2013, Phys. Rev. D, 87, 023527

[11] Bhattacharya, S., Nagai, D., Shaw, L., Crawford, T., & Holder, G. P. 2012, ApJ, 760, 5

[12] Crawford, T. M., Schaffer, K. K., Bhattacharya, S., et al. 2013, arXiv:1303.3535

[13] Niemack, M. D. et al., 2010, SPIE Conference Series, 7741

[14] Lee, A. T., et al., 2008, in AIP Conference Series, 1040

[15] McMahon, J. J. et al., 2009, in AIP Conference Series, 1185

Chapter 2

Brief Review of CMB Lensing Reconstruction Theory

We will here briefly review the theoretical background of lensing reconstruction. This review is intended to complement the broad, generally accessible overview of lensing reconstruction presented in the introduction of this thesis. The discussion in this section follows [1, 3] and unpublished notes written in collaboration with Sudeep Das (these references can be consulted for further details on derivations presented here).

2.1 Lensing of the CMB

The cosmic microwave background anisotropies can be described by their temperature as a function of direction $\hat{\mathbf{n}}$, $T(\hat{\mathbf{n}})$, as well as two Stokes parameters describing their linear polarization $Q(\hat{\mathbf{n}})$ and $U(\hat{\mathbf{n}})$.

The anisotropies are often described as a function of scale instead of position on the sky. In the limit of a small patch of flat sky on which curvature is unimportant, we can describe the structures on the sky with Fourier modes:

$$T(\mathbf{l}) = \int d^2\hat{\mathbf{n}}\; T(\hat{\mathbf{n}}) \exp(i\hat{\mathbf{n}} \cdot \mathbf{l}) \tag{2.1}$$

$$E(\mathbf{l}) \pm iB(\mathbf{l}) = \int d^2\hat{\mathbf{n}}\; [Q(\hat{\mathbf{n}}) \pm iU(\hat{\mathbf{n}})] \exp\left(i\hat{\mathbf{n}} \cdot \mathbf{l} \mp i2\theta_{\mathbf{l}}\right) \tag{2.2}$$

where $\mathbf{l}$ is the Fourier space coordinate conjugate to position $\hat{\mathbf{n}}$ on the sky and $\theta_{\mathbf{l}}$ is the angle spanned by $\mathbf{l}$ and the l_x axis.

We define the angular power spectrum of the CMB temperature C_l through the equation

$$\langle T^*(\mathbf{l}) T(\mathbf{l}') \rangle_{\mathrm{CMB}} = (2\pi)^2 C_l \delta(\mathbf{l} - \mathbf{l}'). \tag{2.3}$$

The polarization power spectra are defined analogously.

Propagating through the universe, the polarized radiation of the microwave background is gravitationally lensed by the intervening large scale structure, which results in a remapping of the observed CMB sky. This remapping can be described by a two-dimensional vector field $\mathbf{d}(\hat{\mathbf{n}})$ on the sky, the lensing deflection field, which points from the direction in which a CMB photon was received to the direction in which it was originally emitted.

Hence if we denote the lensed temperature and polarization fields by T, Q, U and the unlensed fields by $\tilde{T}, \tilde{Q}, \tilde{U}$, they are related through the lensing deflection angle field $\mathbf{d}(\hat{\mathbf{n}}) = \nabla\phi$ as

$$T(\hat{\mathbf{n}}) = \tilde{T}(\hat{\mathbf{n}} + \mathbf{d}(\hat{\mathbf{n}})), \tag{2.4}$$

$$Q(\hat{\mathbf{n}}) = \tilde{Q}(\hat{\mathbf{n}} + \mathbf{d}(\hat{\mathbf{n}})) \tag{2.5}$$

and

$$U(\hat{\mathbf{n}}) = \tilde{U}(\hat{\mathbf{n}} + \mathbf{d}(\hat{\mathbf{n}})). \tag{2.6}$$

The lensing deflection field $\mathbf{d}$ is given by the sum of all small deflections of the CMB photons along their path from the CMB last scattering surface. Writing this sum as an integral along the unperturbed photon path (i.e. applying the Born approximation), the lensing deflection is given by

$$\mathbf{d}(\hat{\mathbf{n}}) = -2 \int_0^{\eta_{LS}} d\eta \frac{\eta_{LS} - \eta}{\eta_{LS}} \nabla_\perp \Psi(\hat{\mathbf{n}}; \eta) \tag{2.7}$$

where Ψ is the Weyl potential (at a point on the photon path specified by $\hat{\mathbf{n}}, \eta$), η is the comoving distance from the observer, η_{LS} is the distance to the CMB last scattering surface, and $\nabla_\perp$ is the gradient taken perpendicular to the line of sight.

This allows us to define a lensing potential ϕ

$$\phi(\hat{\mathbf{n}}) = -2 \int_0^{\eta_{LS}} d\eta \left(\frac{\eta_{LS} - \eta}{\eta_{LS}\eta} \right) \Psi(\hat{\mathbf{n}}; \eta) \tag{2.8}$$

which is related to the deflection field by

$$\mathbf{d} = \nabla\phi \tag{2.9}$$

where the gradient is taken in the two-dimensional plane of the sky.

Another convenient observable is the lensing convergence κ, defined as

$$\kappa(\hat{\mathbf{n}}) = -\nabla \cdot \mathbf{d}(\hat{\mathbf{n}})/2 = -\nabla^2\phi(\hat{\mathbf{n}})/2 \tag{2.10}$$

which depends on the projected matter overdensity instead of the projected Weyl potential.

The deflection field, the lensing potential or the lensing convergence can all be used to describe the lensing effect; one can easily convert from one to the other (with simple gradient operations or Fourier space multiplications), and they are completely equivalent for our purposes (as we are only describing perturbations and are not interested in a constant average mass). We will use the lensing potential in our derivations as it is the simplest to calculate with. Our measurements will often be phrased in terms of the lensing convergence as it can be most directly related to the projected matter overdensity.

2.2 Lensing Reconstruction

We will here present a basic derivation of the methods of lensing reconstruction – the estimation of a CMB lensing map from microwave background maps – using a quadratic estimator. For simplicity, we will only consider lensing reconstruction from CMB temperature data, but the derivation can be easily extended to polarization data as in [3].

As discussed earlier, the lensed and unlensed CMB temperature are related by

$$T(\hat{\mathbf{n}}) = \tilde{T}(\hat{\mathbf{n}} + \nabla\phi\,(\hat{\mathbf{n}})). \tag{2.11}$$

This can be expanded to lowest order in the lensing potential as

$$T(\hat{\mathbf{n}}) \simeq \tilde{T}(\hat{\mathbf{n}}) + \tilde{\nabla}T \cdot \nabla\phi. \tag{2.12}$$

In Fourier space, the above equation reads,

$$T(\mathbf{l}) = \tilde{T}(\mathbf{l}) - \int \frac{d^2\mathbf{l}'}{(2\pi)^2}\mathbf{l}' \cdot (\mathbf{l} - \mathbf{l}')\tilde{T}(\mathbf{l}')\phi(\mathbf{l} - \mathbf{l}'). \tag{2.13}$$

The lensing thus correlates modes such that the correlation is proportional to the lensing potential (averaging only over CMB realizations, which is permissible because the large-scale-structure is effectively uncorrelated with the CMB on small scales):

$$\langle T(\mathbf{l})T(\mathbf{L}-\mathbf{l})\rangle_{\rm CMB} = \left[(\mathbf{L}-\mathbf{l})\cdot\mathbf{L}\;\tilde{C}_{\mathbf{l}-\mathbf{L}} + \mathbf{l}\cdot\mathbf{L}\;\tilde{C}_l\right]\phi(\mathbf{L}) \equiv K(\mathbf{l},\mathbf{L})\phi(\mathbf{L}).$$

We can thus derive an estimator for the lensing potential that sums over pairs of modes:

$$\hat{\phi}(\mathbf{L}) = \int \frac{d^2\mathbf{l}}{(2\pi)^2} f(\mathbf{l},\mathbf{L})T(\mathbf{l})T(\mathbf{L}-\mathbf{l}) \tag{2.14}$$

where we have introduced a function f which weights these pairs of modes. We now derive this function. The function must obviously give an unbiased estimator with the property

$$\phi(\mathbf{L}) = \left\langle \hat{\phi}(\mathbf{L}) \right\rangle_{\rm CMB}. \tag{2.15}$$

Hence there is a constraint on f:

$$I[f] \equiv \int \frac{d^2\mathbf{l}}{(2\pi)^2} f(\mathbf{l},\mathbf{L})K(\mathbf{l},\mathbf{L}) = 1. \tag{2.16}$$

We would also like to have the estimator to have as little variance per mode as possible. This variance $V[f](\mathbf{L})$ is given by:

$$\begin{aligned}
&\left\langle \hat{\phi}^*(\mathbf{L})\hat{\phi}(\mathbf{L}')\right\rangle_{\rm CMB} - \phi^*(\mathbf{L})\phi(\mathbf{L}') = (2\pi)^2\ V[f](\mathbf{L})\ \delta(\mathbf{L}-\mathbf{L}') \qquad (2.17)\\
= &\int \frac{d^2\mathbf{l}}{(2\pi)^2}\frac{d^2\mathbf{l}'}{(2\pi)^2} f^*(\mathbf{l},\mathbf{L}')f(\mathbf{l}',\mathbf{L})\ \langle T^*(\mathbf{l})T^*(\mathbf{L}-\mathbf{l})T(\mathbf{l}')T(\mathbf{L}-\mathbf{l}')\rangle_{\rm CMB} - \phi^*(\mathbf{L})\phi(\mathbf{L}')\\
= &\int \frac{d^2\mathbf{l}}{(2\pi)^2}\frac{d^2\mathbf{l}'}{(2\pi)^2} f^*(\mathbf{l},\mathbf{L})f(\mathbf{l}',\mathbf{L}')[\langle T^*(\mathbf{l})T^*(\mathbf{L}-\mathbf{l})\rangle_{\rm CMB}\langle T(\mathbf{l}')T(\mathbf{L}'-\mathbf{l}')\rangle_{\rm CMB}\\
&+\langle T^*(\mathbf{l})T(\mathbf{l}')\rangle_{\rm CMB}\langle T^*(\mathbf{L}-\mathbf{l})T(\mathbf{L}'-\mathbf{l}')\rangle_{\rm CMB}\\
&+\langle T^*(\mathbf{l})T(\mathbf{L}'-\mathbf{l}')\rangle_{\rm CMB}\langle T^*(\mathbf{L}-\mathbf{l})T(\mathbf{l}')\rangle_{\rm CMB}] - \phi^*(\mathbf{L})\phi(\mathbf{L}')\\
= &\int \frac{d^2\mathbf{l}}{(2\pi)^2}\frac{d^2\mathbf{l}'}{(2\pi)^2} f^*(\mathbf{l},\mathbf{L})f(\mathbf{l}',\mathbf{L}')[K^*(\mathbf{l},\mathbf{L})\phi^*(\mathbf{L})K(\mathbf{l}',\mathbf{L}')\phi(\mathbf{L}')\\
&+(2\pi)^2C_l\delta(\mathbf{l}-\mathbf{l}')(2\pi)^2C_{|\mathbf{L}-\mathbf{l}|}\delta(\mathbf{L}-\mathbf{L}') + (2\pi)^2C_l\delta(\mathbf{L}'-\mathbf{l}-\mathbf{l}')(2\pi)^2C_{|\mathbf{L}-\mathbf{l}|}\delta(\mathbf{l}+\mathbf{l}'-\mathbf{L})\\
&+\{\text{terms linear in }\phi\} + O(\phi^2)] - \phi^*(\mathbf{L})\phi(\mathbf{L}')\\
= &(2\pi)^2\int \frac{d^2\mathbf{l}}{(2\pi)^2}\left[|f(\mathbf{l},\mathbf{L})|^2 C_lC_{|\mathbf{L}-\mathbf{l}|} + f^*(\mathbf{l},\mathbf{L})f(\mathbf{L}-\mathbf{l},\mathbf{L})C_lC_{|\mathbf{L}-\mathbf{l}|}\right]\delta(\mathbf{L}-\mathbf{L}')
\end{aligned}$$

where we have used Wick's Theorem and ignored terms linear in ϕ because they do not contribute when averaged over lensing realizations. We also neglect the terms of order ϕ^2 arising from the final two terms of the Wick's Theorem contractions, as they can be shown to be subdominant (see [2]). Note that from Eq. (2.14), we can assume without loss of generality that f is unchanged under exchanging $\mathbf{l}$ and $\mathbf{L}-\mathbf{l}$ so we obtain an expression for the variance as a functional of f

$$V[f](\mathbf{L}) \;=\; 2\int \frac{d^2\mathbf{l}}{(2\pi)^2} f^2(\mathbf{l},\mathbf{L})C_lC_{|\mathbf{L}-\mathbf{l}|} \qquad (2.18)$$

(note also that the constraint equation (2.16) implies that we can set f to be real). We can thus solve for f by minimizing the variance $V[f](L)$ subject to the constraint $I[f]=1$. We can do this by introducing a Lagrange multiplyer λ and minimizing

$$V[f] - \lambda I[f] \tag{2.19}$$

with respect to f. Minimizing this expression and applying the constraint equation $I = 1$ to solve for λ we obtain:

$$f(\mathbf{l}, \mathbf{L}) = \frac{K(\mathbf{l}, \mathbf{L})}{2C_l C_{|\mathbf{L}-\mathbf{l}|}} N(L) \equiv g(\mathbf{l}, \mathbf{L}) N(L) \tag{2.20}$$

where

$$N(L) = \left[\int \frac{d^2\mathbf{l}}{(2\pi)^2} \frac{K^2(\mathbf{l}, \mathbf{L})}{2C_l C_{|\mathbf{L}-\mathbf{l}|}} \right]^{-1} \tag{2.21}$$

and this equation defines the unnormalized filter function g.

This definition of f optimizes the quadratic estimator for the lensing potential introduced in equation (2.14):

$$\hat{\phi}(\mathbf{L}) = N(L) \int \frac{d^2\mathbf{l}}{(2\pi)^2} g(\mathbf{l}, \mathbf{L}) T(\mathbf{l}) T(\mathbf{L} - \mathbf{l}). \tag{2.22}$$

We can easily convert this to an estimator for the lensing convergence by noting that $\kappa = -\nabla^2\phi/2$. Defining $N^\kappa(L) = L^2 N(L)/2$, we obtain

$$\hat{\kappa}(\mathbf{L}) = N^\kappa(L) \int \frac{d^2\mathbf{l}}{(2\pi)^2} g(\mathbf{l}, \mathbf{L}) T(\mathbf{l}) T(\mathbf{L} - \mathbf{l}). \tag{2.23}$$

In later chapters of this thesis, we will use this estimator to measure a map of the lensing convergence from high-resolution CMB data.

As described in more detail in Chapter 6, the naive estimator for the lensing power spectrum $C_l^{\kappa\kappa}$, $\hat{\kappa}^*\hat{\kappa}$, is biased high: the square of the quadratic estimator for the lensing convergence is a four-point function which is non-zero even in the absence of lensing, due to the contribution of the unwanted Gaussian part of the four-point function. To recover an unbiased estimator, one must hence subtract off

this "Gaussian bias" or N_0 bias (however, one can modify the estimator to avoid this bias, as described in Chapter 6). The final estimator for the lensing power spectrum, which we will use in subsequent chapters of this thesis, is hence:

$$\begin{aligned}(2\pi)^2\delta(\mathbf{L} \;-\; \mathbf{L}')\;\hat{C}_L^{\kappa\kappa} = |N^\kappa(\mathbf{L})|^2 \int \frac{d^2\mathbf{l}}{(2\pi)^2} \int \frac{d^2\mathbf{l}'}{(2\pi)^2} |g(\mathbf{l},\mathbf{L})|^2 \\ \times \Big[T^*(\mathbf{l})\; T^*(\mathbf{L}-\mathbf{l})\; T(\mathbf{l}')\; T(\mathbf{L}'-\mathbf{l}') \\ - \langle T^*(\mathbf{l})\; T^*(\mathbf{L}-\mathbf{l})\; T(\mathbf{l}')\; T(\mathbf{L}'-\mathbf{l}') \rangle_{\text{Gauss}} \Big] \end{aligned} \tag{2.24}$$

where $\langle\rangle_{\text{Gauss}}$ indicates all Wick's Theorem contractions of the four-point-correlation function.

References

[1] Hanson, D., Challinor, A., Efstathiou, G., & Bielewicz, P. 2011, Phys. Rev. D, 83, 043005

[2] Kesden, M., Cooray, A., Kamionkowski, M., Phys. Rev. D, 67, 123507

[3] Hu, W., & Okamoto, T. 2002, ApJ, 574, 566

Chapter 3

Detection of the Power Spectrum of CMB Lensing with the Atacama Cosmology Telescope

3.1 Abstract

We report the first detection of the gravitational lensing of the cosmic microwave background through a measurement of the four-point correlation function in the temperature maps made by the Atacama Cosmology Telescope. We verify our detection by calculating the levels of potential contaminants and performing a number of null tests. The resulting convergence power spectrum at 2-degree angular scales measures the amplitude of matter density fluctuations on comoving length scales of around 100 Mpc at redshifts around 0.5 to 3. The measured amplitude of the signal agrees with Lambda Cold Dark Matter cosmology predictions. Since the amplitude of the convergence power spectrum scales as the square of the amplitude of the density fluctuations, the 4-sigma detection of the lensing signal measures the amplitude of density fluctuations to 12%.

3.2 Introduction

The large-scale distribution of matter deflects the paths of microwave background photons by roughly $3'$ [2, 3, 4, 5], a scale larger than the $\lesssim 1.4'$ angular resolution of the Atacama Cosmology Telescope (ACT). This gravitational lensing imprints a distinctive non-Gaussian signature on the temperature pattern of the microwave sky [6, 7, 8]. Since the cosmic microwave background (CMB) temperature fluctuations are very nearly Gaussian [9, 10, 11] with a power spectrum now well characterized by WMAP [12] and ground-based experiments [13, 14, 15, 16, 17, 18], measurements of the distinctive four-point correlation function due to lensing yield a direct determination of the integrated mass fluctuations along the line of sight [6].

Previous analyses have detected the lensing signature on the microwave sky through cross-correlations of large-scale structure tracers with WMAP data [19, 20], or seen the signature of lensing in the temperature power spectrum at $\lesssim 3\ \sigma$ [15, 18]. Here, we report the first measurement of the lensing signature using only the CMB temperature four-point function and constrain the amplitude of the projected matter power spectrum.

3.3 Data

ACT is a six-meter telescope operating in the Atacama Desert of Chile at an altitude of 5200 meters. The telescope has three 1024-element arrays of superconducting transition-edge sensing bolometers, one each operating at 148 GHz, 218 GHz, and 277 GHz. Previous ACT team publications describe the instrument, observations, and data reduction and initial scientific results [21, 22, 18, 23, 24, 25, 26, 27, 28, 29]. The analysis presented here is done on a 324-square-degree stripe of average noise level $\simeq 23\ \mu$K-arcmin, made from three seasons of 148 GHz observations of the celestial equator. The region is cut into six equally sized (3×18 degree) patches on which we

perform lensing reconstruction separately, and then combine the results with inverse variance weighting.

The ACT temperature maps (made as in [18]) are further processed to minimize the effects of atmospheric noise and point sources. Temperature modes below $\ell = 500$ as well as a 'stripe' of width $\ell = 180$ along the Fourier axis corresponding to map declination are filtered out to reduce the effects of non-white atmospheric noise and scan-synchronous noise respectively [18]. Resolved point sources with a signal-to-noise (S/N) greater than 5 are identified in a match-filtered map [26]. An ACT beam template scaled to the peak brightness of each of these sources is subtracted from the raw data. Using an algorithm inspired by the CLEAN algorithm [30], we repeat this filtering, source identification, and subtraction until there are no S/N>5 identifications. Because the 148 GHz data also contains temperature decrements from the thermal Sunyaev-Zel'dovich (SZ) effect in galaxy clusters, the entire subtraction algorithm is also run on the negative of the map. The effect of unresolved point sources is minimized by filtering out all data above $\ell = 2300$.

3.4 Methods

Gravitational lensing remaps the CMB temperature fluctuations on the sky: $T(\hat{\mathbf{n}}) = \tilde{T}(\hat{\mathbf{n}} + \mathbf{d}(\hat{\mathbf{n}}))$, where $\mathbf{d}(\hat{\mathbf{n}})$ is the deflection field and unlensed quantities are denoted by a tilde. In this chapter, we compute the power spectrum of the convergence field, $\kappa = -\frac{1}{2}\nabla \cdot \mathbf{d}$, using an optimal quadratic estimator [31]:

$$\begin{aligned}(2\pi)^2\delta(\mathbf{L} - \mathbf{L}')\, \hat{C}_L^{\kappa\kappa} = |N^\kappa(\mathbf{L})|^2 \int \frac{d^2\mathbf{l}}{(2\pi)^2} \int \frac{d^2\mathbf{l}'}{(2\pi)^2} |g(\mathbf{l}, \mathbf{L})|^2 \\ \times \Big[T^*(\mathbf{l})\, T^*(\mathbf{L}-\mathbf{l})\, T(\mathbf{l}')\, T(\mathbf{L}'-\mathbf{l}') \\ - \langle T^*(\mathbf{l})\, T^*(\mathbf{L}-\mathbf{l})\, T(\mathbf{l}')\, T(\mathbf{L}'-\mathbf{l}') \rangle_{\text{Gauss}} \Big] \end{aligned} \tag{3.1}$$

where $\mathbf{l}, \mathbf{l}', \mathbf{L}, \mathbf{L}'$ are coordinates in Fourier space (using the flat-sky approximation), g defines filters that can be tuned to optimize signal-to-noise, N is a normalization, and the second term is the Gaussian part of the four-point function. We will refer to the second term as the "Gaussian bias", as it is a Gaussian term one subtracts from the full four-point function to obtain the non-Gaussian lensing signal. We normalize the estimator applying the standard formula in [31, 32] using the mean cross-power spectrum estimated from season-splits of the data.

While the optimal quadratic estimator has the advantage of maximizing the signal-to-noise, an experimental measurement of its amplitude involves subtracting two large numbers (the full four-point function and the bias). Depending on the quality of data and the relevant length scales, this Gaussian four-point bias term can be up to an order of magnitude larger than the lensing convergence spectrum. As the size of the Gaussian bias term depends sensitively on the CMB temperature power spectrum, foregrounds and noise, calculating it to sufficient accuracy using the standard simulation or theory approach is very difficult, and can lead to large discrepancies. Smidt et al. [33] use this standard approach for an analysis of the WMAP data, and report a detection significance larger than expected from Fisher information theory. An alternative approach that does not require this subtraction is presented in [34] (see Chapter 6).

In this analysis, we use the data themselves to obtain a first approximation to the Gaussian bias part of the four-point function, then compute a small correction using Monte Carlo simulations. We first generate multiple randomized versions of the original data map. The Fourier modes of these randomized maps have the same amplitude as the original map, but with their phases randomized. This destroys any non-Gaussian lensing correlation between modes, yet approximately preserves the Gaussian part of the four point function we wish to model. By then averaging the Gaussian biases calculated for many realizations of randomized maps, we obtain a

good estimate of the second term in Eq. (2.1). The small correction we subtract from our estimator (a "null bias" at high ℓ due to spatially varying noise and window functions) is easily calculated from Monte-Carlo simulations. A similar approach has been suggested by [35, 36].

3.5 Simulations

We test our lensing reconstruction pipeline by analyzing a large number of simulated lensed and unlensed maps. The simulated maps are obtained by generating Gaussian random fields with the best fit WMAP+ACT temperature power spectrum [18, 23], which includes foreground models, on maps with the ACT pixelization. We then generate lensed maps from these unlensed maps by oversampling the unlensed map to five times finer resolution, and displacing the pixels according to Gaussian random deflection fields realized from an input theory. Finally, we convolve the maps with the ACT beam, and add simulated noise with the same statistical properties as the ACT data, seeded by season-split difference maps [18].

We apply our lensing estimator to 480 simulations of the equatorial ACT temperature map. For each simulated map we estimate the full four-point function and subtract the Gaussian and null bias terms obtained from 15 realizations of the random phase maps. With 15 realizations, the error on the bias contributes $\sim 15\%$ to the total error bars. We thus obtain a mean reconstructed lensing power spectrum, Eq. (2.1), as well as the standard error on each reconstructed point of the power spectrum. The red points in Fig. 3.1 show the estimated mean convergence power spectrum from the lensed simulations; it can be seen that the input (theory) convergence power spectrum is reconstructed accurately by our pipeline.

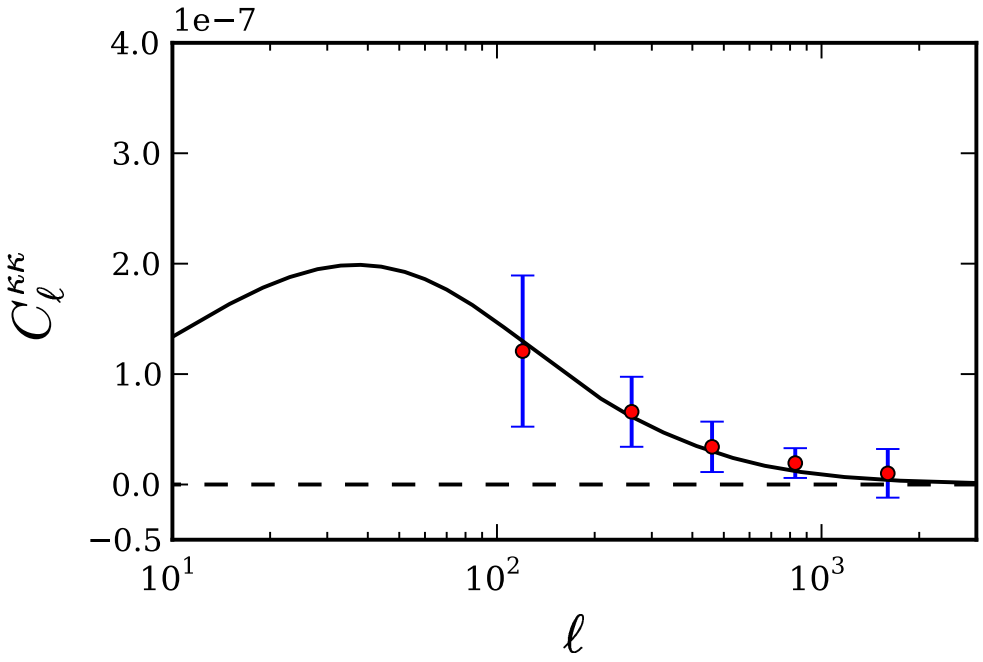

Figure 3.1: Mean convergence power spectrum (red points) from 480 simulated lensed maps with noise similar to our data. The solid line is the input lensing power spectrum, taken from the best-fit WMAP+ACT cosmological model. Error bars correspond to the scatter of power spectrum values obtained from individual maps.

3.6 Results

Fig. 3.2 shows the lensing convergence power spectrum estimated from the ACT equatorial data, using the value of the Gaussian term as well as the null bias obtained from the Monte Carlo simulations previously described. The error bars are obtained from the scatter of simulations shown in Fig. 3.1.

Here, we introduce the parameter A_L as a lensing convergence power spectrum amplitude, defined such that $A_L = 1$ corresponds to the best-fit WMAP+ACT ΛCDM model (with $\sigma_8 = 0.813$). The reconstructed points are consistent with the theoretical expectation for the convergence power spectrum. From our results we obtain a value of $A_L = 1.16 \pm 0.29$, a 4-σ detection. If we restrict our analysis to the first three points, we find $A_L = 0.96 \pm 0.31$. Fitting our five points to the theory, we calculate $\chi^2/\mathrm{dof} = 6.4/4$. Since the lensing kernel has a broad peak at $z \simeq 2$ and a conformal

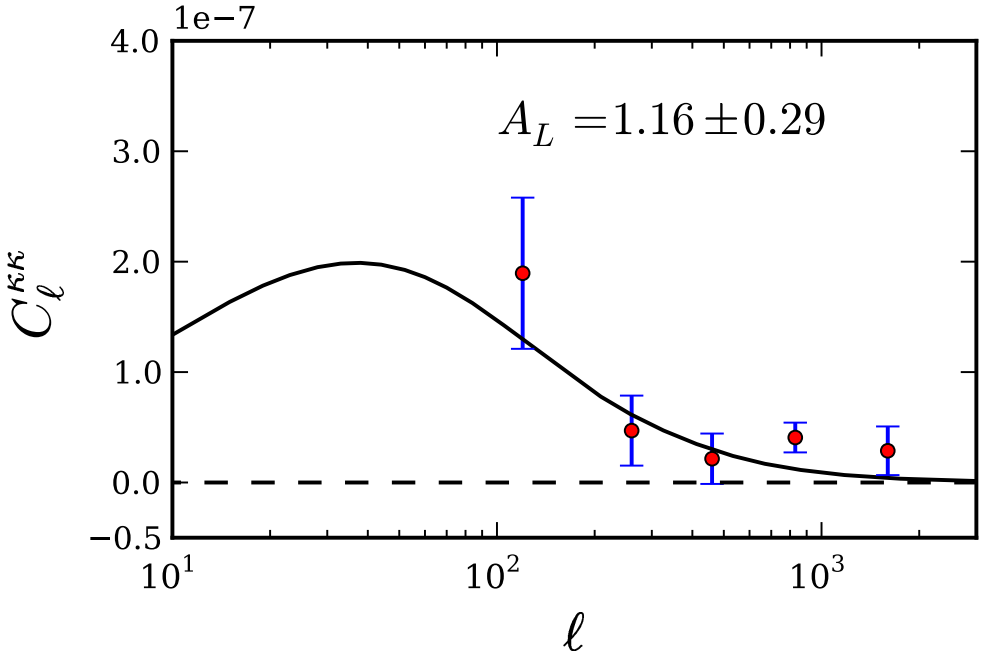

Figure 3.2: Convergence power spectrum (red points) measured from ACT equatorial sky patches. The solid line is the power spectrum from the best-fit WMAP+ACT cosmological model with amplitude $A_L = 1$, which is consistent with the measured points. The error bars are from the Monte Carlo simulation results displayed in Fig. 3.1. The best-fit lensing power spectrum amplitude to our data is $A_L = 1.16 \pm 0.29$

distance of $\simeq 5000$ Mpc, our 4-σ detection is a direct measurement of the amplitude of matter fluctuations at a comoving wavenumber $k \sim 0.02\text{Mpc}^{-1}$ around this redshift.

We estimate potential contamination by point sources and SZ clusters by running our reconstruction pipeline on simulated patches which contain only IR point sources or only thermal or kinetic SZ signal [1], while keeping the filters and the normalization the same as for the data run. Fig. 3.3 shows that the estimated spurious convergence power is at least two orders of magnitude below the predicted signal, due partially to our use of only temperature modes with $\ell < 2300$. We have also verified that reconstruction on simulated maps containing all foregrounds (unresolved point sources and SZ) and lensed CMB was unbiased. We found no evidence of artifacts in the reconstructed convergence power maps.

Table 3.1: Reconstructed $C_\ell^{\kappa\kappa}$ values.

ℓ Range	Central ℓ_b	$C_b^{\kappa\kappa}$ ($\times 10^{-8}$)	$\sigma(C_b^{\kappa\kappa})$ ($\times 10^{-8}$)
75–150	120	19.0	6.8
150–350	260	4.7	3.2
350–550	460	2.2	2.3
550–1050	830	4.1	1.3
1050–2050	1600	2.9	2.2

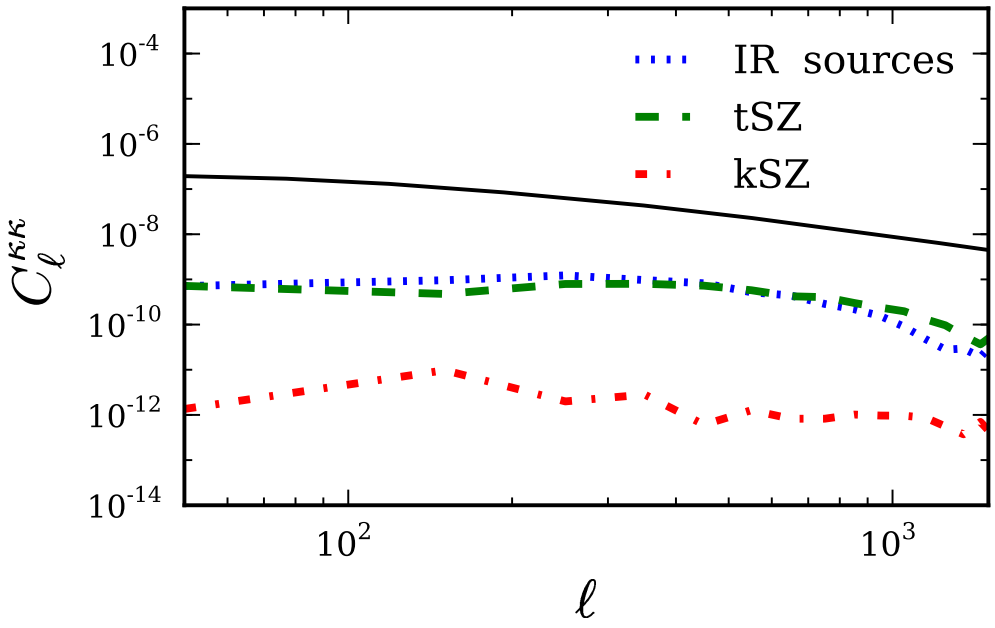

Figure 3.3: Convergence power spectrum for simulated thermal and kinematic SZ maps and point source maps [1] which are a good fit to the ACT data. Note that we only show the non-Gaussian contribution, as the Gaussian part which is of similar negligible size is automatically included in the subtracted bias generated by phase randomization. The solid line is the convergence power spectrum due to lensing in the best-fit WMAP+ACT cosmological model.

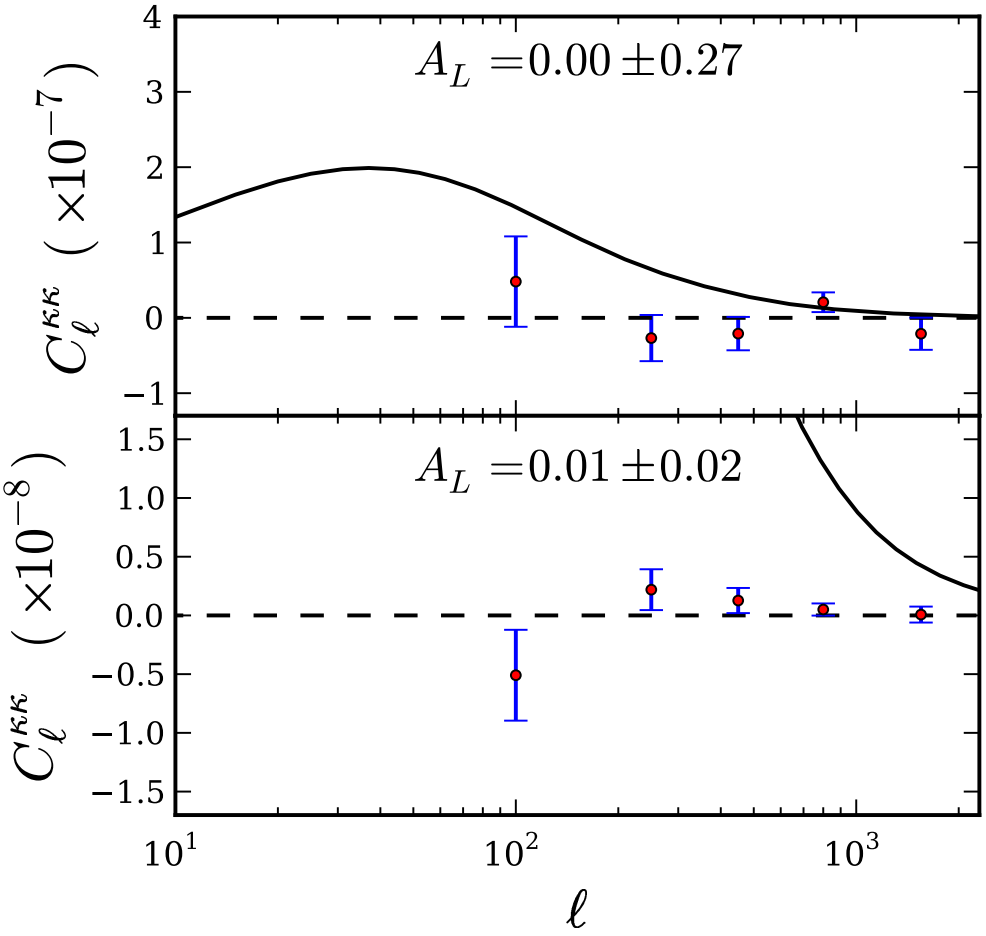

Figure 3.4: *Upper panel:* Mean cross-correlation power spectrum of convergence fields reconstructed from different sky patches. The result is consistent with null, as expected. *Lower panel:* Mean convergence power spectrum of noise maps constructed from the difference of half-season patches, which is consistent with a null signal. The error bars in either case are determined from Monte Carlo simulations, and those in the lower panel are much smaller as they do not contain cosmic variance.

3.7 Null Tests

We compute a mean cross-correlation power of convergence maps reconstructed from neighboring patches of the data map, which is expected to be zero as these patches should be uncorrelated. We find a $\chi^2/\mathrm{dof} = 5.8/4$ for a fit to zero signal (Fig. 3.4, upper panel). For the second null test we construct a noise map for each sky patch

by taking the difference of maps made from the first half and second half of the season's data, and run our lensing estimator. Fig. 3.4, lower panel, shows the mean reconstructed convergence power spectrum for these noise-only maps. Fitting to null we calculate $\chi^2 = 5.7$ for 4 degrees of freedom. The null test is consistent with zero, showing that the contamination of our lensing reconstruction by noise is minimal. We also tested our phase randomization scheme by randomizing the phases on a map, using it to reconstruct a convergence map, and cross correlating it with a reconstruction from the same map but with a different phase randomization; our results were consistent with null as expected.

3.8 Implications and Conclusions

We have reported a first detection of the convergence power spectrum of the cosmic microwave background due to gravitational lensing. The inferred amplitude of the lensing signal is consistent with theoretical expectations of the basic cosmological model. A detection is also anticipated from the South Pole Telescope team. Data from the Planck satellite [37], and CMB polarization measurements with ACTPol, SPTPol, PolarBear and other next generation experiments [38, 39, 40] will yield even more accurate measurements of CMB lensing. Such measurements are also an important goal for a future polarization satellite mission [41]. This work is the first step of an exciting research program.

3.9 Acknowledgements

This work was supported by the U.S. NSF through awards AST-0408698 for the ACT project, and PHY-0355328, AST-0707731 and PIRE-0507768, as well as by Princeton Univ. and the Univ. of Pennsylvania, RCUK Fellowship, NASA grant NNX08AH30G, NSERC PGSD scholarship, NSF AST-0546035 and AST-0807790, NSF Physics Fron-

tier Center grant PHY-0114422, KICP Fellowship, SLAC no.DE-AC3-76SF00515, and the BCCP. Computations were performed on the GPC supercomputer at the SciNet HPC Consortium. Funding at the PUC from FONDAP, Basal, and the Centre AIUC is acknowledged. We thank B. Berger, R. Escribano, T. Evans, D. Faber, P. Gallardo, A. Gomez, M. Gordon, D. Holtz, M. McLaren, W. Page, R. Plimpton, D. Sanchez, O. Stryzak, M. Uehara, and the Astro-Norte group for assistance with ACT observations. We thank Thibaut Louis, Oliver Zahn and Duncan Hanson, and Kendrick Smith for discussions and draft comments.

3.10 Addendum: Updated Measurement of the Lensing Power Spectrum from Three Seasons of Data

In this addendum we present an updated measurement of the lensing power spectrum using improved ACT maps on the same ACT equatorial strip region. The maps used in this analysis derive from three seasons of observations from 2008 to 2010 and thus have significantly reduced noise levels – $\simeq 18$ μK-arcmin instead of $\simeq 23$ μK-arcmin – as well as improvements to the mapmaking. The details of the improved measurements, data reduction and mapmaking are described in [42].

Our new measurement of lensing uses the same methodology as previously described in this chapter. Lensing is again measured using a quadratic estimator in temperature; the power spectrum of the CMB lensing convergence is thus a temperature four-point function measurement, with the required filtering, normalization, and bias subtraction performed exactly as described for the earlier measurement.

Systematic contamination of the estimator by SZ signal and IR sources was estimated earlier in this chapter using the simulations from Sehgal et al. [1]. We found

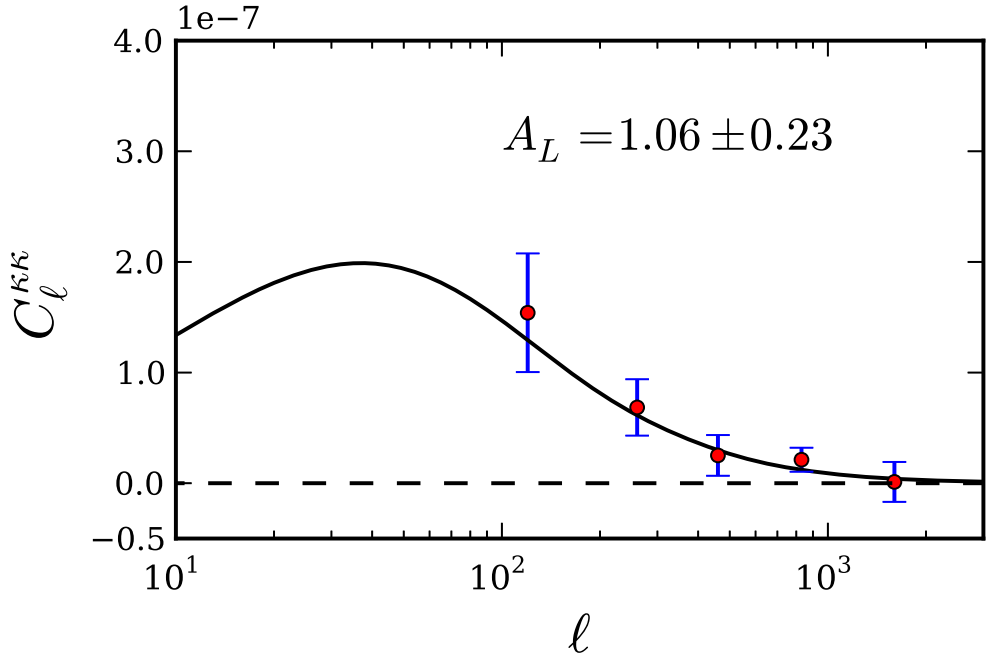

Figure 3.5: CMB convergence power spectrum reconstructed from the ACT equatorial strip temperature data. The enhanced effective depth of the three-season coadded ACT equatorial map ($\simeq 18$ μk-arcmin) compared to its previous version as described previously ($\simeq 23$ μk-arcmin) leads to an improved detection significance.

that, with the ACT lensing pipeline as used in this work, the contamination is smaller than the signal by two orders of magnitude and can thus be neglected. This result appears well-motivated for two reasons, which also apply to our updated analysis with the improved data: first, in the analysis we only use the signal-dominated scales below $\ell = 2300$, at which SZ, IR and radio power are subdominant; second, by using the data to estimate the bias, our estimator automatically subtracts the Gaussian part of the contamination, so that only a very small non-Gaussian residual remains. The previously described contamination estimates are not strictly applicable to this new lensing estimate, because the filters used here contain somewhat lower noise, and thus admit slightly more signal at higher ℓs; however, estimates by the SPT collaboration (van Engelen et al. 2012) with similar noise levels and filters also find negligible

contamination. The contamination levels in our improved analysis are thus expected to be negligible.

The measured CMB lensing power spectrum, detected at 4.6σ, is shown in Fig. 3.5, along with a theory curve showing the convergence power spectrum for a fiducial ΛCDM model defined by the parameter set $(\Omega_b, \Omega_m, \Omega_\Lambda, h, n_s, \sigma_8) = (0.044,\ 0.264,\ 0.736,\ 0.71,\ 0.96,\ 0.80)$. Constraining the conventional lensing parameter A_L that rescales the fiducial convergence power spectrum ($C_\ell^{\kappa\kappa} \rightarrow A_L C_\ell^{\kappa\kappa}$) we obtain $A_L = 1.06 \pm 0.23$. The data are thus a good fit to the ΛCDM prediction for the amplitude of CMB lensing. We find the spectrum to have Gaussian errors, uncorrelated between bins.

References

[1] Sehgal, N. et al., 2010, ApJ, 709, 920

[2] Cole, S. & Efstathiou, G., 1989, Mon. Not. R. Astron. Soc, 239, 195

[3] Linder, E. V. et al., 1990, Mon. Not. R. Astron. Soc, 243, 353

[4] Seljak, U., 1996, ApJ, 463, 1

[5] Bernardeau, F., 1997, A&A, 324, 15

[6] Zaldarriaga, M. & Seljak, U., 1999, Phys. Rev. D, 123507

[7] Hu, W. & Okamoto, T., 2002, Phys. Rev. D, 083002

[8] Challinor, A. & Lewis, A., 2003, Physics Reports, 429, 1

[9] Komatsu, E. et al., 2003, ApJS, 148, 119

[10] Spergel, D. N. et al., 2007, ApJS, 170, 377

[11] Bennett, C. L. et al., 2011, 192, 17

[12] Larson, D. et al., 2011, ApJS, 192, 16

[13] Brown, M. L. et al., 2009, ApJ, 705, 978

[14] Friedman, R. B. et al., 2009, 700, 187

[15] Reichardt, C. L. et al., 2009, ApJ, 694, 1200

[16] Sievers, J. L. et al., 2009, arXiv:0901.4540

[17] Lueker, M. et al., 2010, ApJ, 719, 1045

[18] Das, S. et al., 2011, ApJ, 729, 62

[19] Smith, K. M., Zahn, O., & Doré, O., 2007, Phys. Rev. D, 76, 043510

[20] Hirata, C. M., Ho, S., Padmanabhan, N., Seljak, U., and Bahcall, N. A., 2008, Phys. Rev. D, 78, 043520

[21] Fowler, J. W. et al., 2010, ApJ, 722, 1148

[22] Swetz, D. S. et al., 2010, arXiv:1007.0290

[23] Dunkley, J. et al., 2010, arXiv:1009.0866

[24] Hajian, A., et al., 2010, arXiv:1009.0777

[25] Marriage, T. A., et al., 2010, arXiv:1007.5256

[26] Marriage, T. A., et al. 2010, arXiv:1010.1065

[27] Menanteau, F. et al., 2010, ApJ, 723, 1523

[28] Sehgal, N. et al., 2010, arXiv:1010.1025

[29] Hand, N. et al., 2011, arXiv:1101.1951

[30] Högbom, J. A. et al., A&AS, 1974, 15, 417

[31] Hu, W. & Okamoto, T., 2002, ApJ, 574, 566

[32] Kesden, M., Cooray, A., Kamionkowski, M., 2003, Phys. Rev. D, 67, 123507

[33] Smidt, J., et al., 2011, ApJ, 728, 1

[34] Sherwin, B. D., & Das, S., 2010, arXiv:1011.4510

[35] Dvorkin, C., & Smith, K. M., 2009, Phys. Rev. D, 79, 043003

[36] Hanson, D., Challinor, A., Efstathiou, G., & Bielewicz, P., 2011, Phys. Rev. D, 83, 043005

[37] Perotto, L., Bobin, J., Plaszczynski, S., Starck, J., & Lavabre, A. A&A, 519, A4

[38] Niemack, M. D. et al., 2010, SPIE Conference Series, 7741

[39] McMahon, J. J. et al., 2009, in AIP Conference Series, 1185

[40] Lee, A. T., et al., 2008, in AIP Conference Series, 1040

[41] Smith, K. M. et al., 2008, arXiv:0811.3916

[42] Das, S. et al., 2013, arXiv:1301.1037

Chapter 4

Evidence for Dark Energy from the CMB Alone Using ACT Lensing Measurements

4.1 Abstract

For the first time, measurements of the cosmic microwave background radiation (CMB) alone favor cosmologies with $w = -1$ dark energy over models without dark energy at a 3.2-sigma level. We demonstrate this by combining the CMB lensing deflection power spectrum from the Atacama Cosmology Telescope with temperature and polarization power spectra from the Wilkinson Microwave Anisotropy Probe. The lensing data break the geometric degeneracy of different cosmological models with similar CMB temperature power spectra. Our CMB-only measurement of the dark energy density Ω_Λ confirms other measurements from supernovae, galaxy clusters and baryon acoustic oscillations, and demonstrates the power of CMB lensing as a new cosmological tool.

4.2 Introduction

Observations made over the past two decades suggest a standard cosmological model for the contents and geometry of the universe, as well as for the initial fluctuations that seeded cosmic structure [4, 5, 6]. The data imply that our universe at the present epoch has a dominant stress-energy component with negative pressure, known as "dark energy", and has zero mean spatial curvature. The cosmic microwave background (CMB) has played a crucial role in constraining the fractional energy densities in matter, Ω_m, and in dark energy or the cosmological constant, Ω_Λ (or equivalently in curvature $\Omega_K = 1 - \Omega_\Lambda - \Omega_m$) [e.g., 33]. Throughout this chapter, we restrict our analysis to the simplest dark energy models with equation of state parameter $w = -1$.

The existence of dark energy, first directly observed by supernova measurements [4, 5], is required [6] by the combination of CMB power spectrum measurements and any *one* of the following low redshift observations [10, 11, 13, 14, 12]: measurements of the Hubble constant, measurements of the galaxy power spectrum, galaxy cluster abundances, or supernova measurements of the redshift-distance relation. At present, the combination of low-redshift astronomical observations with CMB data can constrain cosmological parameters in a universe with both vacuum energy and curvature to better than a few percent [33].

However, from the CMB alone, it has not been possible to convincingly demonstrate the existence of a dark energy component, or that the universe is geometrically flat [6, 33]. This is due to the "geometric degeneracy" which prevents both the curvature and expansion rate from being determined simultaneously from the CMB alone [1, 2, 3]. The degeneracy can be understood as follows. The first peak of the CMB temperature power spectrum measures the angular size of a known physical scale: the sound horizon at decoupling, when the CMB was last scattered by free electrons. However, very different cosmologies can project this sound horizon onto the same degree-scale angle on the sky: from a young universe with a large vacuum energy and

negative spatial curvature, to the standard spatially flat cosmological model, to an old universe with no vacuum energy, positive spatial curvature, and a small Hubble constant [22]. These models, therefore, cannot be significantly distinguished using only primordial CMB power spectrum measurements.

By observing the CMB at higher resolution, however, one can break the geometric degeneracy using the effect of gravity on the CMB [20]: the deflection of CMB photons on arcminute scales due to gravitational lensing by large scale structure. This lensing of the CMB can be described by a deflection field $\mathbf{d}(\mathbf{n})$ which relates the lensed and unlensed temperature fluctuations $\delta T, \delta\tilde{T}$ in a direction $\mathbf{n}$ as $\delta T(\mathbf{n}) = \delta\tilde{T}(\mathbf{n} + \mathbf{d})$. The lensing signal, first detected at 3.4σ from the cross-correlation of radio sources with WMAP data [23] and at 4σ from the CMB alone by the Atacama Cosmology Telescope (ACT) [7], is sensitive to both the growth of structure in recent epochs and the geometry of the universe [1]. Combining the low-redshift information from CMB lensing with CMB power spectrum data gives significant constraints on Ω_Λ, which the power spectrum alone is unable to provide.

The constraining power of the CMB lensing measurements is apparent in a comparison between two models consistent with the CMB temperature power spectrum (see Fig. 4.1): the spatially flat ΛCDM model with dark energy which best fits the WMAP seven-year data [24] and a model with positive spatial curvature but without dark energy.

The two theory temperature spectra and the temperature-polarization cross-correlation spectra differ only at the largest scales with multipoles $\ell < 10$, where the cosmic variance errors are large. (The differences are due to the Integrated Sachs-Wolfe (ISW) effect, a large-scale CMB distortion induced by decaying gravitational potentials in the presence of dark energy [17] or, with the opposite sign, induced by growing potentials in the presence of positive curvature.) Though the temperature-

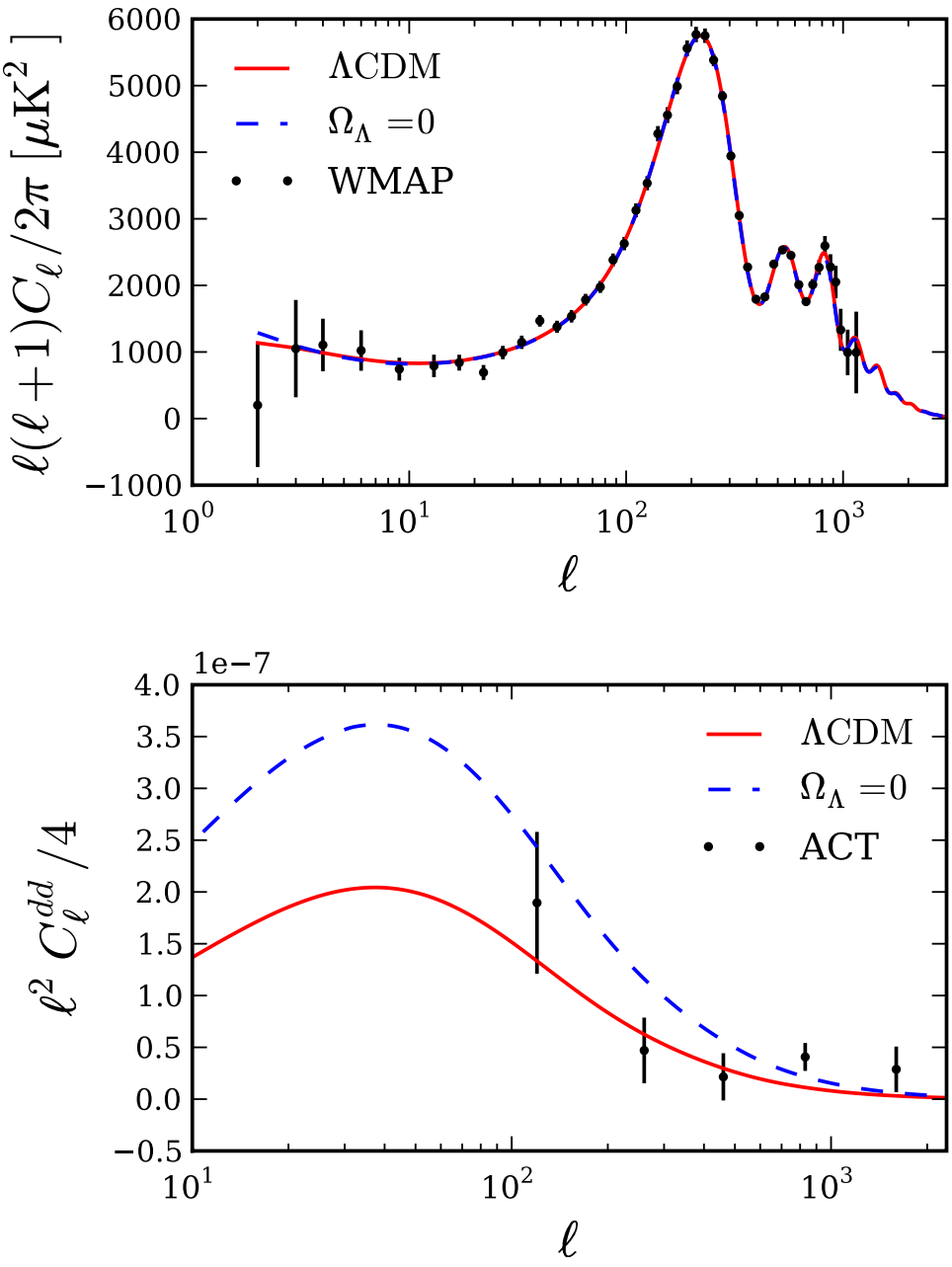

Figure 4.1: Upper panel: Angular power spectra of CMB temperature fluctuations for two geometrically degenerate cosmological models, one the best-fit curved universe with no vacuum energy ($\Omega_\Lambda = 0, \Omega_m = 1.29$), and one the best-fit flat ΛCDM model with $\Omega_\Lambda = 0.73, \Omega_m = 0.27$. The seven-year WMAP temperature power spectrum data [24] are also shown; they do not significantly favor either model. Lower panel: The CMB lensing deflection power spectra are shown for the same two models. They are no longer degenerate: the $\Omega_\Lambda = 0$ universe would produce a lensing power spectrum larger than that measured by ACT ([7], also shown above).

polarization cross-spectra differ somewhat at low ℓ, overall the polarization spectra in the two models are also very similar on all scales.

However, these two cosmologies predict significantly different CMB lensing deflection power spectra C_ℓ^{dd}. Fig. 4.1 shows that the universe with $\Omega_\Lambda = 0$ produces more lensing on all scales. The ACT measurements shown in Fig. 4.1 are a better fit to the model with vacuum energy than to the model without dark energy.

Why is the lensing power spectrum higher in a universe without dark energy but with the same primordial CMB spectrum? This can be understood from the expression for the power spectrum of lensing deflection angles [1]:

$$\frac{\ell^2}{4} C_\ell^{dd} = \int_0^{\eta_*} d\eta \underbrace{W^2(\eta)}_{\text{geometry}} \underbrace{\left[D\left(\eta\right)/a(\eta)\right]^2}_{\text{growth}} \tag{4.1}$$

where η is conformal lookback distance, η_* is the conformal distance to the CMB last scattering surface, D is the growth factor of matter perturbations since decoupling, a is the scale factor, and $W(\eta)$ is a geometry and projection term given by

$$W(\eta) = \frac{3}{2}\Omega_m H_0^2 \, \frac{d_A(\eta_* - \eta)}{d_A(\eta_*)} \, P^{1/2}\left(k = \frac{\ell + 1/2}{d_A(\eta)}, \eta_*\right).$$

where H_0 is the Hubble constant, d_A is comoving angular diameter distance, $P(k, \eta_*)$ is the matter power spectrum at decoupling and k is the comoving wavenumber.

A plot of the kernel of the lensing integral in this equation, as well as its constituent "geometry" and "growth" terms, is shown in Fig. 4.2 for both ΛCDM and $\Omega_\Lambda = 0$ models. This figure shows that increased lensing in universes without dark energy is due to three effects: (1) CMB photons in a universe without dark energy spend more time at lower redshifts where structure is larger; (2) structure and potentials grow more in a universe with $\Omega_\Lambda = 0$ and positive curvature; (3) in a universe without dark energy, projection effects pick out longer wavelength fluctuations which are larger for most lensing scales.

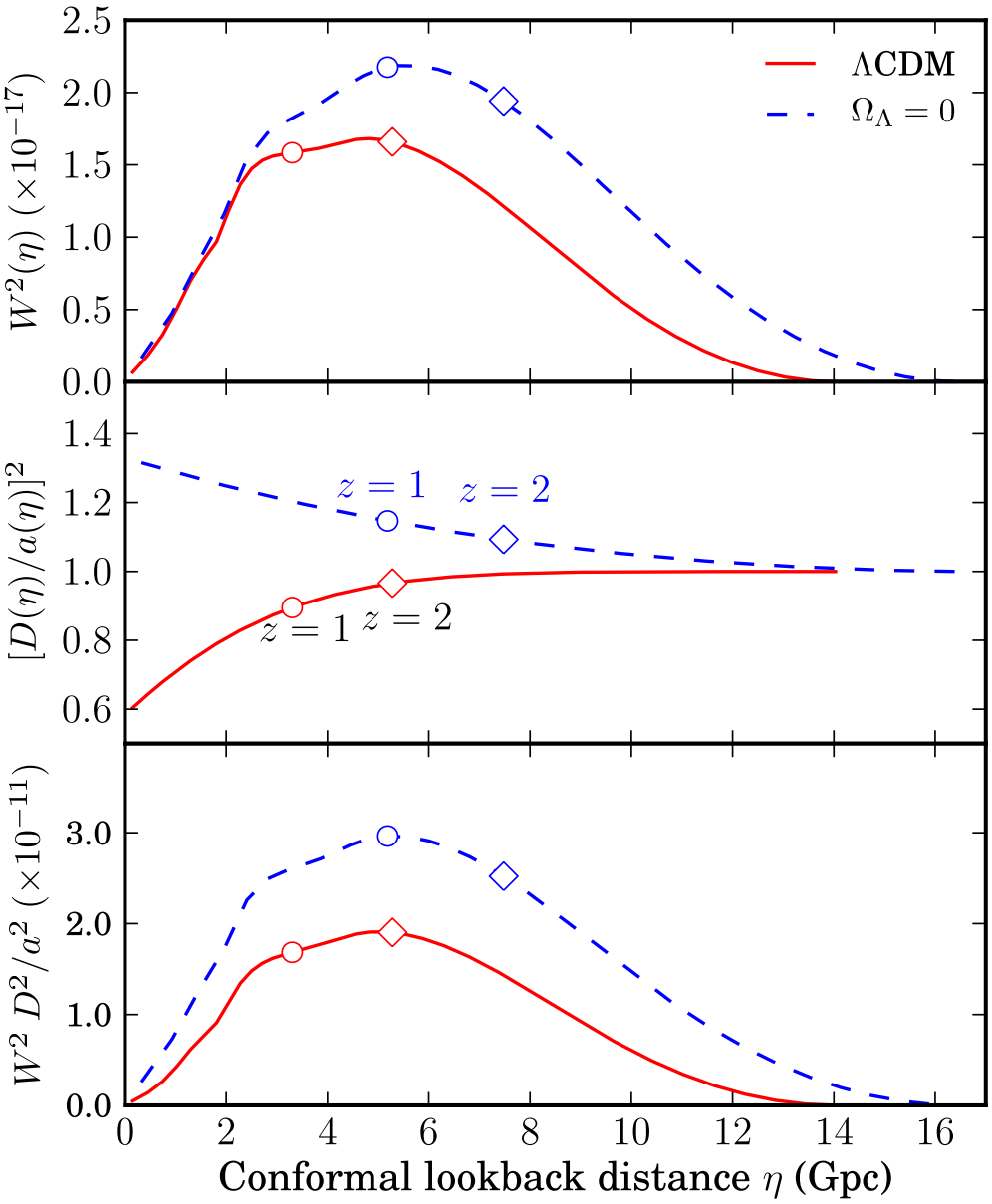

Figure 4.2: Different terms in the kernel of the lensing integral of Eq. 4.1 as a function of conformal lookback distance for $\ell = 120$, for models as in Fig. 4.1. Upper panel: geometry term. Middle panel: growth term, scaled to its value at decoupling for clarity. Bottom panel: total kernel.

As the amplitude of the lensing signal is sensitive to $z < 5$ physics, measurements of CMB lensing break the geometric degeneracy and improve constraints on cosmological parameters. In this chapter, we construct a likelihood function by com-

bining ACT lensing measurements and WMAP power spectra, and explore the new CMB-only parameter constraints resulting from the inclusion of lensing data.

4.3 Methodology

We fit a joint distribution for a set of cosmological parameters θ to our data D (see, e.g. [24]). In our analysis, we consider the following cosmological parameters:

$$\theta = \{\Omega_\Lambda, \Omega_K, \Omega_b h^2, \Omega_c h^2, n_s, \Delta^2_{\mathcal{R}}, \tau, A_{\rm SZ}\} \tag{4.2}$$

where $\Omega_b h^2$ is the baryon density, $\Omega_c h^2$ is the cold dark matter (CDM) density, n_s is the spectral tilt of the density fluctuations, $\Delta^2_{\mathcal{R}}$ is their amplitude (defined at pivot scale $k_0 = 0.002$/Mpc), τ is the optical depth to reionization, and $A_{\rm SZ}$ is the amplitude of the WMAP V-band SZ template [31]. The Hubble constant, $H_0 \equiv 100\ h$ km/s/Mpc, can be derived from these parameters. The estimated distribution is the product of the likelihood $p(D|C_\ell(\theta))$ and the prior $p(\theta)$. Here $C_\ell(\theta)$ is the set of theoretical angular power spectra (CMB temperature power spectrum C_ℓ^{TT}, CMB polarization power spectra C_ℓ^{TE} and C_ℓ^{EE}, and lensing deflection angle power spectrum C_ℓ^{dd}) derived from the parameters θ. Uniform priors are placed on all sampled parameters. We use data from the WMAP seven-year temperature and polarization observations [24], which map the CMB anisotropy over the full sky. These are combined with the ACT lensing deflection power spectrum described in [7], obtained from a measurement of the lensing non-Gaussianity in a 324 deg^2 patch of the ACT equatorial CMB maps. The data were found to be effectively free of contamination from astrophysical sources or noise, with errors that were estimated to be Gaussian and uncorrelated. Since the correlation between the datasets is negligible, the likelihood is the product of the WMAP likelihood, $p(D_{\rm WMAP}|{C_\ell}^{\rm TT,TE,EE}(\theta))$, described in [24], and the ACT lensing likelihood, $p(D_{\rm ACT}|{C_\ell}^{dd}(\theta))$ [7].

Theoretical CMB temperature and lensing power spectra are computed using the CAMB code [26]. We follow the same approach as [22, 24] to map out the posterior distribution of the parameters.

4.4 Results

The two-dimensional marginalized distribution for Ω_Λ and $\Omega_m = 1-\Omega_K-\Omega_\Lambda$ is shown in Fig. 4.3, with 68% and 95% confidence levels, indicating the effect of adding the ACT lensing data.

The distribution for WMAP alone is limited by the ISW effect in both the TE and TT power, but is still unbounded at $\Omega_\Lambda = 0$. It is truncated with the addition of the lensing data, resulting in a two-dimensional 95% confidence level that excludes $\Omega_\Lambda = 0$. The one-dimensional probability density for Ω_Λ, shown in Fig. 4.4, further demonstrates how the CMB lensing data reduce the low-Ω_Λ tail of the probability distribution and break the geometric degeneracy. A universe without dark energy would give too large a lensing signal to be consistent with the data. With lensing data, the new confidence intervals for Ω_Λ are $0.61^{+0.14}_{-0.06}$ at 1σ (68% C.L.), $0.61^{+0.23}_{-0.29}$ at 2σ (95% C.L.) and $0.61^{+0.25}_{-0.53}$ at 3σ (99.7% C.L.), favoring a model with dark energy. Comparing the likelihood value for the best-fit ΛCDM model with the likelihood for the best-fit $\Omega_\Lambda = 0$ model, we find that $\Omega_\Lambda = 0$ is disfavored at 3.2σ ($\Delta\chi^2 \approx 11$, of which $\Delta\chi^2 \approx 5$ arises from the WMAP spectra, mainly due to differences in the TE and TT power spectra for $\ell < 10$). The parameters of the best-fit ΛCDM model are consistent with constraints from other datasets such as the WMAP+BAO+H_0 constraints of [33]. The effect of massive neutrinos on the lensing spectrum is different from the effect of Ω_Λ; neutrino masses within the current bounds can only modify the shape of the spectrum by $< 5\%$ [30], whereas the reduction in Ω_Λ considered here increases the spectrum on all scales by a much larger amount.

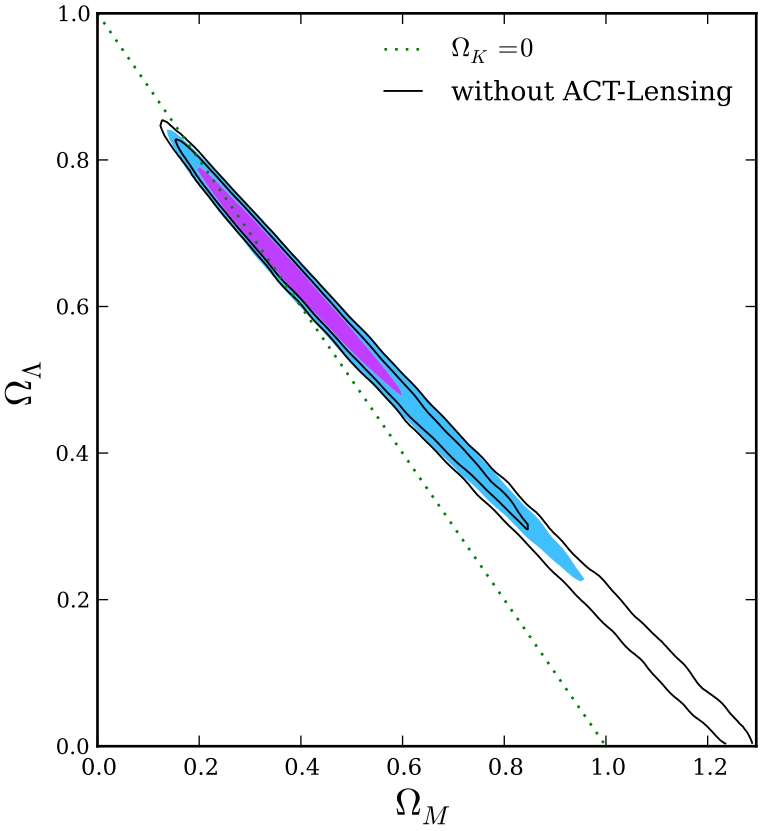

Figure 4.3: Two-dimensional marginalized posterior probability for Ω_m and Ω_Λ (68% and 95% C.L.s shown). Colored contours are for WMAP + ACT Lensing, black lines are for WMAP only. Using WMAP data alone, universes with $\Omega_\Lambda = 0$ lie within the 95% C.L. The addition of lensing data breaks the degeneracy, favoring models with dark energy.

4.5 Conclusions

We find that a dark energy component Ω_Λ is required at a 3.2σ level from CMB data alone. This constraint is due to the inclusion of CMB lensing power spectrum data, which probe structure formation and geometry long after decoupling and so break the CMB geometric degeneracy. Our analysis provides the first demonstration of the ability of the CMB lensing power spectrum to constrain cosmological parameters. It provides a clean verification of other measurements of dark energy. In future work, our analysis can be easily extended to give constraints on more complex forms of dark energy with $w \neq -1$. With much more accurate measurements of CMB lensing

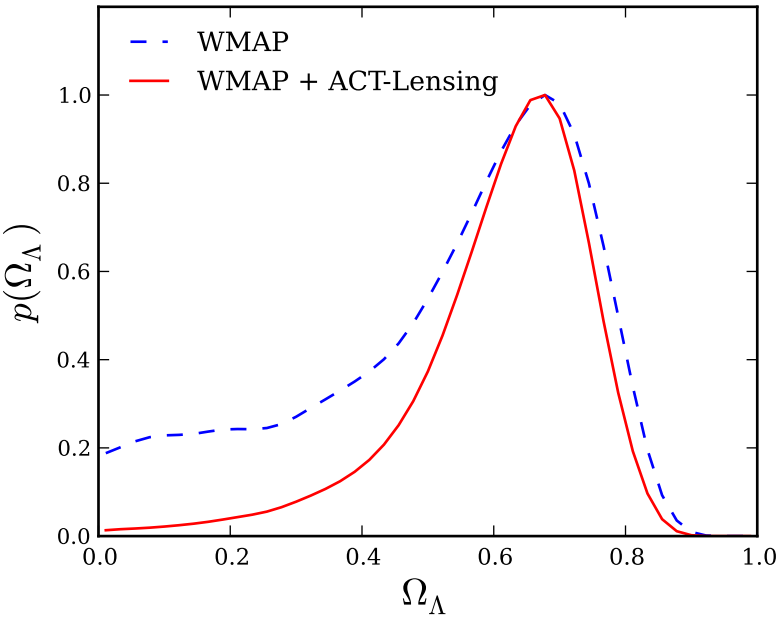

Figure 4.4: One-dimensional marginalized posterior probability for Ω_Λ (not normalized). An energy density of $\Omega_\Lambda \simeq 0.7$ is preferred even from WMAP alone, but when lensing data are included, an $\Omega_\Lambda = 0$ universe is strongly disfavoured.

expected from ACT, SPT [27], Planck [28], and upcoming polarization experiments including ACTPol [29], lensing reconstruction promises to further elucidate the properties of dark energy and dark matter [32].

4.6 Acknowledgements

This work was supported by the U.S. NSF through awards AST-0408698, PHY-0355328, AST-0707731 and PIRE-0507768, as well as by Princeton Univ., the Univ. of Pennsylvania, FONDAP, Basal, Centre AIUC, RCUK Fellowship, NASA grant NNX08AH30G, NSERC PGSD, the Rhodes Trust, NSF AST-0546035 and AST-0807790, NSF PFC grant PHY-0114422, KICP Fellowship, SLAC no. DE-AC3-76SF00515, ERC grant 259505, BCCP, and the NSF GRFP. We thank B. Berger, R. Escribano, T. Evans, D. Faber, P. Gallardo, A. Gomez, M. Gordon, D. Holtz, M. McLaren, W. Page, R. Plimpton, D. Sanchez, O. Stryzak, M. Uehara, and Astro-

Norte for assistance with ACT. ACT operates in the Parque Astronómico Atacama in northern Chile under the auspices of Programa de Astronomía, a program of the Comisión Nacional de Investigación Científica y Tecnológica de Chile (CONICYT). We thank Alex van Engelen for discussions and thank Matias Zaldarriaga and Duncan Hanson for comments on the draft.

References

[1] Doroshkevich, A. G., Zel'dovich, Y. B. & Sunyaev, R. A. 1978, Soviet Astronomy, 22, 523

[2] Bond, J. R., Efstathiou, G. & Tegmark, M., 1997, Mon. Not. R. Astron. Soc, 291, L33

[3] Zaldarriaga, M., Spergel, D. N. & Seljak, U., 1997, ApJ, 488, 1

[4] Riess, A. G. et al. , 1998, AJ, 116, 1009

[5] Perlmutter S. et al., 1999, ApJ, 517, 565

[6] Spergel D. N. et al., 2003, ApJS, 148, 175

[7] Smoot G. F. et al., 1992, ApJ, 396, L1

[8] Miller A. D. et al., 1999, ApJ, 524, L1

[9] Komatsu E. et al., 2009, ApJS, 180, 330

[10] Hicken, M. et al., 2009, 700, 1097

[11] Kessler, R. et al., 2009, ApJS, 185, 32

[12] Vikhlinin, A. et al., 2009, ApJ, 692, 1060

[13] Reid, B. A. et al., 2010, Mon. Not. R. Astron. Soc, 404, 60

[14] Riess, A. G. et al., 2009, ApJ, 699, 539

[15] Das, S. et al., 2011, PRL in press

[16] Komatsu, E. et al., 2010, ApJS

[17] Boughn, S. P., Crittenden, R. G. & Turok, N. G., 1998, New Astronomy, 3, 275

[18] Boughn, S. & Crittenden, R., 2004, Nature, 427, 45

[19] Lewis, A. & Challinor, A., 2006, 429, 1

[20] Stompor, R. & Efstathiou, G., 1999, Mon. Not. R. Astron. Soc, 302, 735

[21] Zaldarriaga, M. & Seljak, U., 1998, Phys. Rev. D, 58, 023003

[22] Dunkley, J. et al., 2009, 180, 306

[23] Smith, K. M., Zahn, O. & Doré, O., 2007, 76, 043510

[24] Larson, D. et al., 2010, arxiv

[25] Dunkley, J. et al., 2010, arXiv:1009.0866D

[26] Lewis, A., Challinor, A. & Lasenby, A., 2000, ApJ, 658, 473

[27] Carlstrom, J. E. et al., 2009, arXiv:0907.4445C

[28] Perotto, L. et al., 2010, A&A, 519, A4

[29] Niemack, M. D. et al., 2010, Proc. SPIE, 7741

[30] Lesgourgues, J., Perotto, L., Pastor, S. & Piat, M., 2006, Phys. Rev. D, 73, 4

[31] Komatsu, E. & Seljak, U., 2002, Mon. Not. R. Astron. Soc, 336, 1256

[32] Galli, S. et al., 2010, Phys. Rev. D, 82, 123504

[33] Komatsu, E. et al., ApJS, 192, 18

Chapter 5

Cross-correlation of CMB Lensing with the Distribution of Quasars

5.1 Abstract

We measure the cross-correlation of Atacama Cosmology Telescope CMB lensing convergence maps with quasar maps made from the Sloan Digital Sky Survey DR8 SDSS-XDQSO photometric catalog. The CMB lensing-quasar cross-power spectrum is detected for the first time at a significance of 3.8σ, which directly confirms that the quasar distribution traces the mass distribution at high redshifts $z > 1$. Our detection passes a number of null tests and systematic checks. Using this cross-power spectrum, we measure the amplitude of the linear quasar bias assuming a template for its redshift dependence, and find the amplitude to be consistent with an earlier measurement from clustering; at redshift $z \approx 1.4$, the peak of the distribution of quasars in our maps, our measurement corresponds to a bias of $b = 2.5 \pm 0.6$. With the signal-to-noise ratio on CMB lensing measurements likely to improve by an order of magnitude over the next few years, our results demonstrate the potential of CMB lensing cross-correlations to probe astrophysics at high redshifts.

5.2 Introduction

As the photons of the cosmic microwave background (CMB) travel through the universe, they are gravitationally deflected by the web of matter through which they pass. In the CMB sky we observe today, these deflections are imprinted as arcminute-scale distortions of small scale temperature fluctuations [1, 2]. The microwave background thus contains not only information about the primordial universe at redshift ≈ 1100, but also about the matter density fluctuations in the lower redshift universe.

CMB lensing measurements are a powerful cosmological probe [10] because they are sensitive to both the growth of density fluctuations and the geometry and size of the universe, yet are relatively insensitive to both instrumental and astrophysical systematic errors [6, 7]. Lensing measurements can constrain the properties of dark energy [18], the amplitude of density fluctuations and the masses of neutrinos [11]. They can also constrain the properties of biased tracers of the matter distribution. The focus of this chapter is the cross-correlation of CMB lensing maps with one such tracer – quasars.

Quasars are among the most luminous objects in the universe. Their immense luminosity is believed to be powered by accreting supermassive black holes [12, 13] which reside at the center of almost every massive galaxy [14]. As the activity of quasars and the rate of star formation appear to be linked [15], they are a crucial element in our present understanding of galaxy evolution. Measurements of the relation between dark matter and the distribution of quasars can inform us about quasar properties such as the masses of the dark matter halos that host the quasars, the scatter in the quasar-halo mass relation and the quasar duty cycle (see e.g. [16]). Such measurements of quasar properties will, in turn, improve our understanding of structure formation and galaxy evolution.

Both the number density of quasars and the strength of CMB lensing in a certain direction depend on the projected dark matter density in this direction, and quasars

are most common at the redshifts that produce the largest lensing deflections. This implies that the CMB lensing and quasar fields should be strongly correlated [17]. Measuring the cross-power spectrum and comparing it to theoretical calculations, we can determine the proportionality factor which relates a fluctuation in matter density to a fluctuation in quasar number density. This proportionality factor is known as the quasar linear bias b (defined as $b \equiv \delta_q/\delta$ where δ_q and δ are the fractional spatial overdensities of quasars and matter respectively).

In this work we present the first measurement of the CMB lensing-quasar cross-power spectrum, and use it to derive a constraint on the quasar bias. The chapter is organized as follows. Section II presents the theoretical background underlying the CMB lensing-quasar cross-correlation. Section III explains how the lensing and quasar maps used in our analysis are constructed, and describes the resulting cross-spectrum measurement. The constraint on quasar linear bias we obtain from the cross-power spectrum is presented in section IV. Null tests and systematic checks are discussed in section V. All calculations assume a ΛCDM cosmology with WMAP5 parameters [19] and $\sigma_8 = 0.819$.

5.3 Theoretical Background

Cosmological weak lensing effects can be described using the convergence field κ, which is equal to a weighted projection of the matter overdensity δ [1]

$$\kappa(\hat{\mathbf{n}}) = \int_0^{z_{LS}} dz W^{\kappa}(z)\delta(\eta(z)\hat{\mathbf{n}}, z). \tag{5.1}$$

The relevant kernel (assuming a flat universe) is

$$W^{\kappa}(z) = \frac{3}{2H(z)}\Omega_0 H_0^2(1+z)\eta(z)\frac{\left(\eta^{LS} - \eta(z)\right)}{\eta^{LS}} \tag{5.2}$$

where $\eta(z)$ is the comoving distance to redshift z, $\hat{\mathbf{n}}$ is a direction on the sky, η^{LS} is the comoving distance to the last scattering surface, z_{LS} is the redshift of the last scattering surface, $H(z)$ is the Hubble parameter, and Ω_0 and H_0 represent the present values of the matter density parameter and the Hubble parameter, respectively.

The fractional overdensity of quasars in a direction $\hat{\mathbf{n}}$ is given by $q(\hat{\mathbf{n}})$, which – assuming a linear bias relation between the distribution of matter and quasars – is given by

$$q(\hat{\mathbf{n}}) = \int_0^{z_{LS}} dz W^q(z)\delta(\eta(z)\hat{\mathbf{n}}, z), \tag{5.3}$$

where the kernel is

$$W^q(z) = \frac{b(z)\frac{dN}{dz}}{\left[\int dz' \frac{dN}{dz'}\right]} + \frac{3}{2H(z)}\Omega_0 H_0^2 (1+z) g(z)(5s-2) \tag{5.4}$$

and

$$g(z) = \eta(z)\int_z^{z_{LS}} dz'(1-\eta(z)/\eta(z'))\frac{\frac{dN}{dz'}}{\left[\int dz'' \frac{dN}{dz''}\right]} \tag{5.5}$$

(see [17]). Here b is the linear bias, dN/dz is the redshift distribution of quasars, and s is the variation of the number counts of quasars $N(< m)$ with the limiting magnitude m at the faint limit of the quasar catalog, $s \equiv d\log_{10} N/dm$. The second term in Eq. 4 is the magnification bias: the change in source density in a certain direction induced by lensing magnification. For the quasar catalog used in this work (which has $s \approx 0.043$) this term is significantly smaller than the first term ($\approx 15\%$ of its magnitude) and is negative.

Combining Eqs. 1 and 3 gives the expected lensing-quasar cross-power spectrum in the Limber approximation [20]:

$$C_\ell^{\kappa q} = \int \frac{dz H(z)}{\eta^2(z)} W^\kappa(z) W^q(z) P(k = \ell/\eta(z), z), \tag{5.6}$$

where $P(k, z)$ is the matter power spectrum at wavenumber k and redshift z.

5.4 Cross-correlating CMB Lensing and Quasars

5.4.1 The ACT CMB Lensing Convergence Maps

The lensing convergence fields used in our analysis are reconstructed from CMB temperature maps made by the Atacama Cosmology Telescope (ACT) [23, 24, 25], a 6m telescope operating in the Atacama desert in Chile. These CMB temperature maps are obtained from observations made during 2008-2010 in the 148 GHz frequency band and calibrated as in [26]. The maps consist of six patches, each of size 3×18 degrees, in the Sloan Digital Sky Survey (SDSS) Stripe 82 region [27], with a map-averaged white noise level of 21 μK arcmin. Radio and IR point sources as well as Sunyaev-Zel'dovich (SZ) clusters detected with a matched filter at a signal-to-noise ratio greater than 5 as in [6] are masked and inpainted using the methods of [9].

The convergence maps are reconstructed from the CMB temperature maps as in [6] using the minimum variance quadratic estimator procedure described in [3]. The estimator works as follows. While the unlensed CMB is statistically isotropic, any lensing deflection imprints a preferred direction into the statistical properties of the CMB. This corresponds mathematically to the fact that formerly uncorrelated modes of the isotropic unlensed CMB temperature field are correlated by lensing, with the correlation proportional to the lensing deflection. We can hence estimate the lensing convergence by measuring the correlation between pairs of Fourier modes using a quadratic estimator:

$$\hat{\kappa}(\mathbf{L}) = N(\mathbf{L}) \int \mathrm{d}^2\mathbf{l}\; f(\mathbf{L},\mathbf{l})\; T(\mathbf{l})T(\mathbf{L}-\mathbf{l}). \tag{5.7}$$

Here $\mathbf{l}, \mathbf{L}$ are Fourier space coordinates, N is the normalization function (which ensures that the estimator is unbiased) and f is a weighting such that the signal-to-noise ratio on the reconstructed convergence is maximized in the case of isotropic noise

with full sky coverage (see [3] for the details of these functions). The weighting uses a smoothed version of the observed anisotropic noise power. To calculate the normalization function we multiply a first-approximation normalization which uses the data power spectrum by a small L-dependent correction factor. This factor is obtained from Monte-Carlo simulations by requiring that on average the cross-power of the reconstructed convergence with the true simulation convergence be equal to the true convergence power spectrum. The simulated maps used in this Monte-Carlo calculation are constructed to match ACT data in both signal and noise properties as in [6]. In our lensing reconstruction, we use a wider range of scales in the temperature map than in [6], filtering out modes below $\ell = 500$ and above $\ell = 4000$. As can be seen in Eq. 7, lensing information at a scale ℓ is obtained from two temperature modes *separated* by ℓ, so that this filtering does not preclude us from obtaining small-ℓ lensing modes. Intuitively, this is because we deduce the distribution of large scale lenses from the distortion of small scale temperature fluctuations.

We subtract from the reconstructed ACT convergence maps a simulated mean field map $\langle\hat{\kappa}\rangle$, obtained from 480 realizations of simulated reconstructed lensing maps. This map is non-zero due to correlations induced by window functions and noise which, to the convergence estimator, appears as a small spurious lensing signal which must be subtracted.

We can thus estimate the CMB lensing-quasar cross power spectrum by calculating

$$C_\ell^{\kappa q} = \langle \mathrm{Re}[(\hat{\kappa}(\mathbf{l}) - \langle\hat{\kappa}\rangle(\mathbf{l}))^* q(\mathbf{l})]\rangle_{\mathbf{l}\in\ell} \tag{5.8}$$

where the outer average is over all pixels with Fourier coordinates $\mathbf{l}$ which lie within the bandpower corresponding to ℓ.

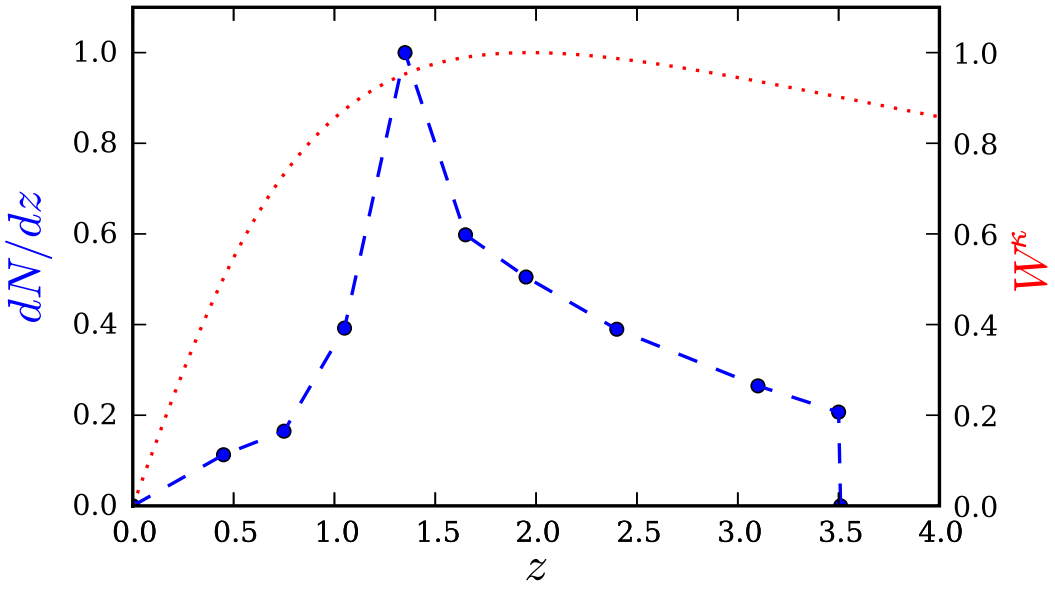

Figure 5.1: The redshift distribution of SDSS quasars used to construct our maps of fractional quasar overdensity, normalized to a unit maximum. The corresponding redshift bins are shown with blue filled circles; they are interpolated to give the continuous curve used in our theory calculations (blue dashed line). For comparison, the red dotted line shows the lensing kernel $W^{\kappa}(z)$, again normalized to a unit maximum.

5.4.2 The SDSS Quasar Maps

In this work we use the SDSS-XDQSO photometric quasar catalog [21, 22], extracted from the SDSS Data Release 8. The analysis used in this catalog separates the population of quasars and foreground stars using a probabilistic model in flux space. This analysis assigns a probability of being a quasar to every point-source with de-reddened i-band magnitude between 17.75 and 22.45 mag in the SDSS imaging. Though the catalog extends out to $z > 4$, we do not use the highest-redshift sources with redshifts $z > 3.5$. This reduces the shot noise error on our measurement, as there are very few such sources. Using this catalog, we construct a map of the fractional overdensity q of quasars across the same 324 square degrees on which we perform our lensing reconstruction. We include in our quasar maps, with unit weight, all point sources with a

greater than $p = 0.68$ probability of being a quasar. As the probability distribution is non-uniform, the residual level of stellar contamination can be calculated from the catalog probabilities to be 6% (we discuss later how this is accounted for in our theoretical calculations). A spectroscopic quasar sample at high redshifts ($2.2 < z < 3.5$) does show a contamination fraction which is $\approx 15\%$ larger than that predicted by the catalog (see [22]); however, the majority of the quasars we consider are at lower redshift where the XDQSO model estimates should be significantly more accurate (high redshift quasar selection is less accurate because at $z \approx 2.8$ the quasar and stellar loci cross in color space). We neglect the error on the stellar contamination fraction, which is any case smaller than the statistical error (and would only reduce the measured signal, not increase it). The area covered by our quasar maps contains on average 75 quasars per square degree. The redshift distribution of the quasars in our maps is shown in Fig. 1, along with the CMB lensing kernel, which has a very similar redshift distribution.

5.4.3 The CMB Lensing - Quasar Cross-Power Spectrum

The cross-power spectrum of the ACT CMB lensing maps and the SDSS quasar maps is shown in Fig. 2.

The error bars on the data points are calculated theoretically as proportional to $\sqrt{C_\ell^{\kappa\kappa} C_\ell^{qq}}$, with an additional factor calculated from the number of independent pixels in the bin corresponding to each data point. The spectra used in this calculation are the full data spectra which include both signal and noise (including Poisson noise). Bootstrap error estimates from splits of our data are consistent with this calculation. For comparison, we also calculate error bars using Monte-Carlo methods, cross correlating 480 realizations of simulated reconstructed lensing maps (containing signal and realistic noise) with the quasar data maps. Both methods assume the two maps are uncorrelated; such calculations are very good approximations to the true error

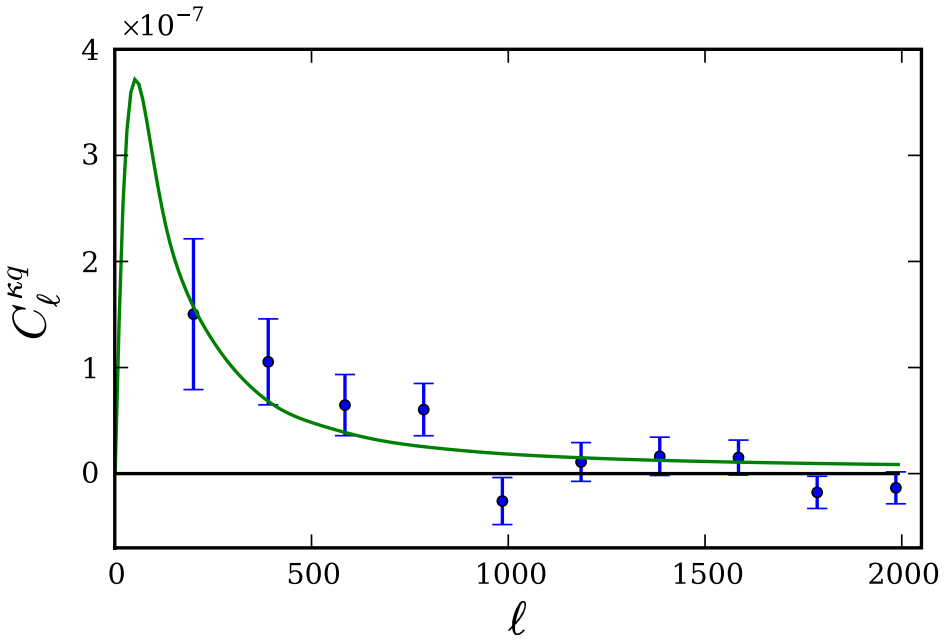

Figure 5.2: The CMB lensing - quasar density cross-power spectrum, with the data points shown in blue (the covariance between different data points is negligible). The significance of the detection of the cross-spectrum is 3.8σ. The green solid line is a theory line calculated assuming the fiducial bias amplitude. This theory line is reduced by 6% to account for the expected level of stellar contamination of the quasar sample.

on the cross-correlation because both maps are noisy so that $C_\ell^{\kappa\kappa} C_\ell^{qq} \gg (C_\ell^{\kappa q})^2$. The error bars obtained from Monte-Carlo methods are nearly indistinguishable from the theory error bars, and lead to the same detection significance. (We also verified that replacing the quasar data maps with 480 simulated maps with the same number of randomly distributed sources leads to similar, though slightly smaller, errors.) The Monte-Carlo estimates of the errors also allow us to calculate the full covariance matrix. The off-diagonal elements are negligible compared to the diagonal elements; for every bin, the covariance between neighboring bins was less than 4% of the bin autocorrelation. We thus neglect covariance between different data points in our analysis.

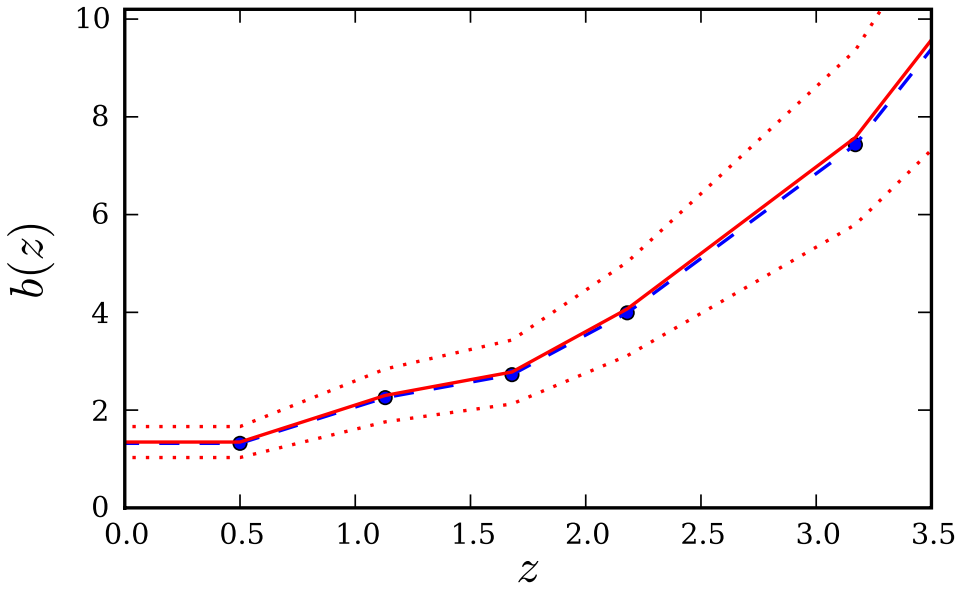

Figure 5.3: Blue dashed line: fiducial quasar bias template (interpolated from the data points of [31]), used in the theoretical calculation of the CMB lensing - quasar cross-power spectrum. Red solid line: the bias amplitude ($b/b_{\rm fid} = 1.02$) best fit by the measured cross-power spectrum; red dashed lines: the $\pm 1\sigma$ error ranges of this amplitude. Note that only one degree of freedom is constrained: the overall bias amplitude of an assumed redshift evolution.

Also shown in Fig. 2 is a theoretical calculation of the expected cross-power spectrum obtained from Eq. 6. In this calculation the matter power spectrum was computed using the CAMB software [29]. The non-linear (HALOFIT, [30]) matter power spectrum was used; however, using a linear matter power spectrum instead only slightly changed the computed cross-spectrum (as most of the signal arises from angular scales corresponding to linear scales in the matter power spectrum, where the linear and non-linear matter power spectra hardly differ). We use the quasar redshift distribution as shown in Fig. 1 in this calculation. As the integration kernel is slowly varying, the theory curve is insensitive to the binning and interpolation of this redshift distribution. A fiducial bias model for this calculation is obtained by interpolating the central measured bias values of [31] (averaging the values obtained

with and without the inclusion of negative points in the correlation function). The fractional error on these central bias values is below 10% at low redshifts $z < 2$, but rises to $\sim 20\%$ at $z \sim 4 - 5$. The values were obtained from measurements of the amplitude of the quasar correlation function (which is sensitive to the bias) for an SDSS spectroscopic quasar sample. This fiducial bias model is shown in Fig. 3. As the theoretical cross power spectrum does not depend strongly on the detailed form of the bias model, we use this measurement as a convenient fiducial template, though the spectroscopic catalog used in this measurement does not extend to as faint a magnitude as the photometric catalog we use to make quasar maps. Despite this, the quasar power spectrum predicted by this fiducial bias model is consistent with the power spectrum of our quasar maps. The calculated theoretical cross-power spectrum is reduced by 6% to account for stellar contamination; while stars are uncorrelated with lensing, they contribute to the average density of sources, and so cause us to calculate a fractional quasar overdensity that is 6% too small.

The data fit the theory curve (which assumes the fiducial bias model) well, with a chi-squared value for this curve of $\chi^2_{\rm theory} = 13.2$ for 10 degrees of freedom. We obtain the significance of our detection of the cross-power spectrum by calculating $\sqrt{\chi^2_{\rm null} - \chi^2_{\rm theory}}$, where $\chi^2_{\rm null}$ is calculated for the null line. The significance of the detection is found to be 3.8σ.

5.5 A Constraint on the Quasar Bias

We calculate a constraint on the linear bias of quasars from the lensing-quasar cross-power spectrum. To do so we assume a bias template of the fiducial shape shown in Fig. 3, but rescaled by a constant factor for all redshifts. We calculate the likelihood as a function of this scaling parameter $b/b_{\rm fid}$ and plot it in Fig. 4. Our result, $b/b_{\rm fid} = 1.02 \pm 0.24$, is consistent with the fiducial bias model, i.e. a value of unity. (Due to

the small negative magnification bias, $b/b_{\rm fid} = 0$ does not correspond exactly to the null line.) As the redshift distribution is peaked at $z = 1.4$, $b/b_{\rm fid}$ can be interpreted as approximately parametrizing the amplitude of the bias at redshift 1.4. From this interpretation we obtain a value of the bias at $z \approx 1.4$ of $b = 2.5 \pm 0.6$, which is in good agreement with previous measurements from quasar clustering [31]. We can associate this bias with a host halo mass M_{200}: using the bias model of [32], we obtain a halo mass of $\log_{10}(M_{200}/M_{\odot}) = 12.9^{+0.3}_{-0.5}$, consistent with previous estimates [31, 16]. We also verify that the cross-power calculated using only a low ($z < 2.2$) or high ($z > 2.2$) redshift quasar sub-sample is consistent with the bias given by the fiducial model; however, we defer a detailed calculation of bias constraints using multiple quasar sub-samples to future work with a higher signal-to-noise ratio.

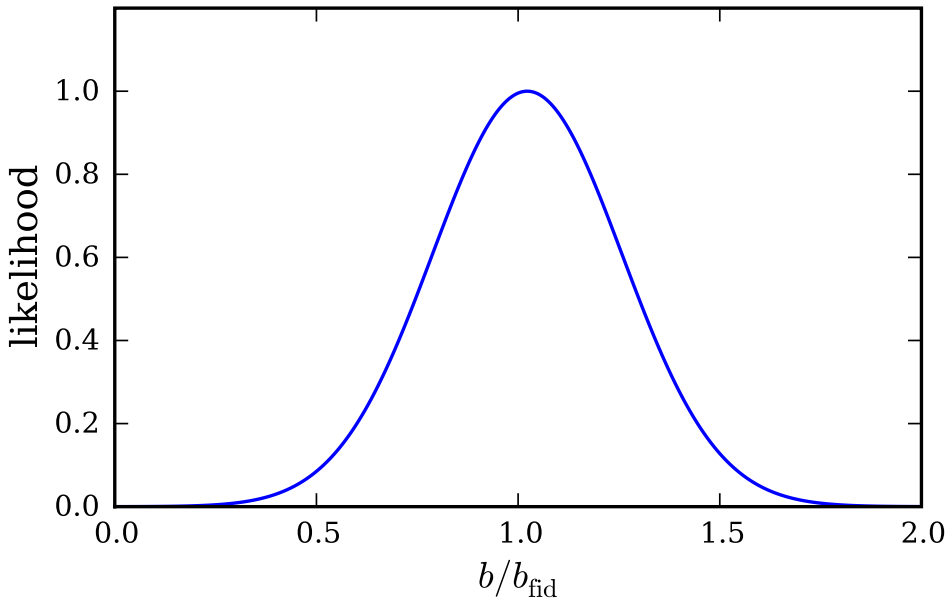

Figure 5.4: Likelihood as a function of quasar bias divided by the fiducial bias, $b/b_{\rm fid}$ (we assume that the shape of the redshift dependence is constant and has the fiducial form of Fig. 3, and modify the amplitude of the bias function to calculate this likelihood.) Interpreting our measurement of $b/b_{\rm fid} = 1.02 \pm 0.24$ as a bias at $z \approx 1.4$ (the peak in the quasar distribution), we obtain $b = 2.5 \pm 0.6$ at this redshift.

5.6 Testing the power spectrum

5.6.1 Null Tests

We check our result and our pipeline with a number of null tests. In a simple first test, we cross-correlate the quasar distribution in one part of the sky with the lensing convergence in another; as seen in Fig. 5, the results are consistent with null as expected, with $\chi^2 = 6.5$ for 10 degrees of freedom for a fit to null. A more sophisticated test is to calculate the cross-correlation of the quasar maps with the curl component of the lensing deflection (this differs from the convergence reconstructed earlier, which is gradient-like). The reconstructed curl map is expected to be zero (though it should contain reconstruction noise), and hence the cross-correlation with the quasar maps should be zero as well. We reconstruct the curl component of the estimator as in [7] (though keeping the normalization and filters unchanged from the earlier convergence reconstruction, and simply replacing the dot product in $f(\mathbf{L}, \mathbf{l})$ of Eq. 7 with a cross product projected onto the $\hat{\mathbf{l}}_\mathbf{x} \times \hat{\mathbf{l}}_\mathbf{y}$ direction). The cross-correlation of the lensing curl component with the quasar maps is also shown in Fig. 5. The error bars are calculated from theory as before. As expected, this test is consistent with a null result, with a (somewhat low) value of $\chi^2 = 3.5$ for 10 degrees of freedom.

5.6.2 Estimating Potential Systematic Contamination

We estimate the magnitude of what are expected to be the largest contaminants: infrared (IR) sources, SZ clusters and galactic cirrus, which contribute flux to the CMB temperature maps. (The level of radio source power is much smaller as we can resolve and mask such sources down to low flux levels.) Contamination of the cross-power spectrum is conceivable because the sources of IR and SZ signal trace the underlying matter field as the quasars do, and galactic cirrus could reduce observed quasar counts by extinction. As explained in [8], any IR or SZ contamination

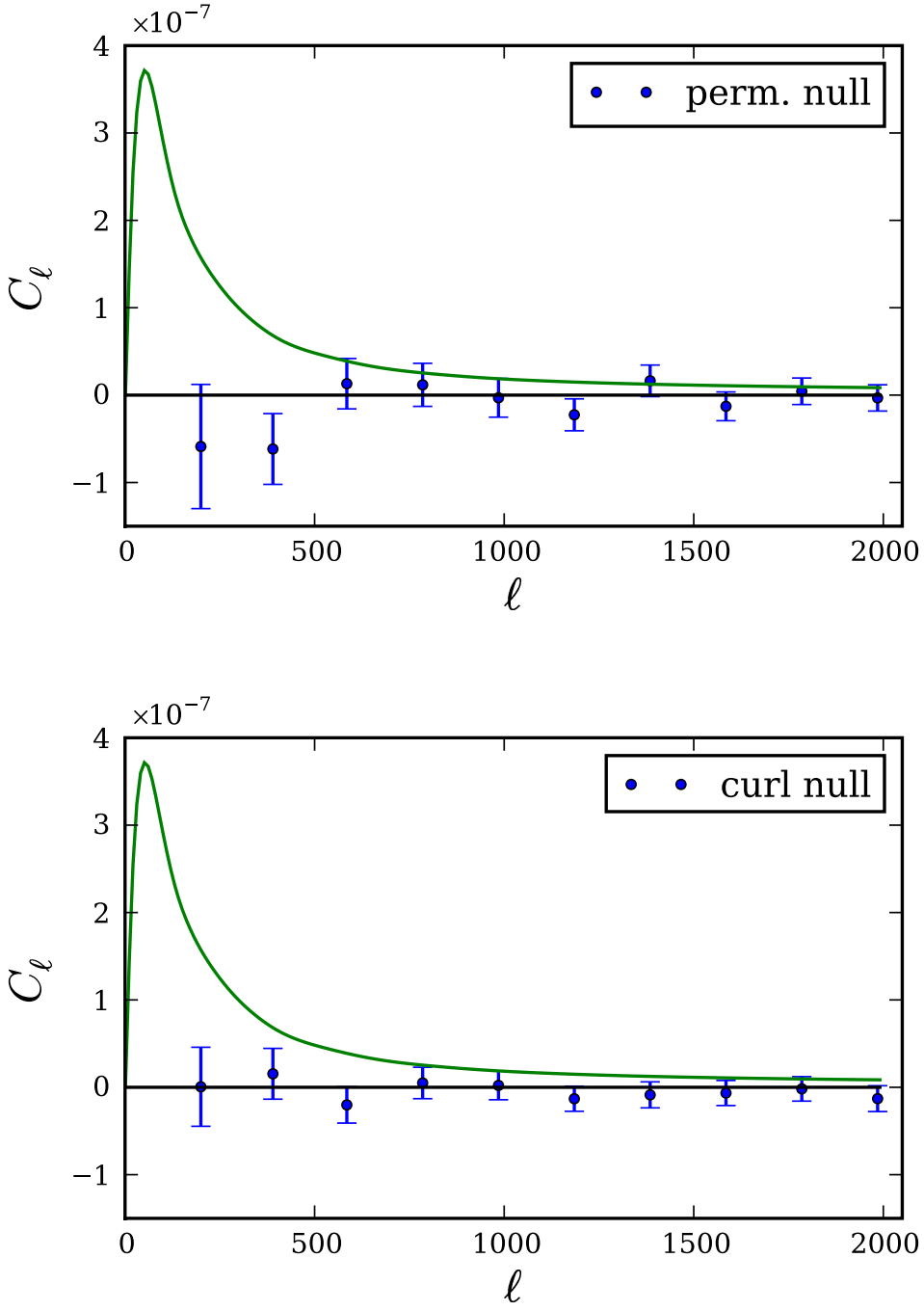

Figure 5.5: Two successful null tests, both consistent with zero. Upper panel: the cross-power spectrum of quasar and lensing maps covering different parts of the sky (permutation null test). Lower panel: the cross-power spectrum of the reconstructed curl component of the lensing signal with the quasar maps (curl null test).

would appear as a negative bias, as a large IR or SZ signal in a certain direction increases local gradients; the lensing estimator falsely interprets this as a signature of demagnification of the CMB and hence estimates a spurious underdensity in this direction.

To obtain an estimate of the contribution of IR and SZ contamination to the measured cross-power spectrum, we construct simulated quasar maps which are correlated with the IR and SZ maps of the simulations of [28]. The quasar maps are constructed by randomly populating all halo positions (listed for all halos with masses greater than $6.8 \times 10^{12} M_{\odot}$ in the catalog supplied with [28]) with quasars. In populating the halos we use a redshift-dependent probability of occupation such that the final simulated quasar map has the correct redshift distribution. Cross-correlating this quasar map with the true convergence maps of the same simulation, the signal is consistent with the theory line of Fig. 2, which confirms that our simple simulation has approximately the correct bias (this is due to the average mass in the halo catalog being similar to the typical halo mass of a linear bias model consistent with the fiducial model).

The level of systematic contamination in our estimator can be obtained from these simulated quasar, IR, and SZ maps. Keeping the same filtering and normalization as in our data, we reconstruct the IR contaminant to the lensing signal by replacing the temperature maps in Eq. 7 with the simulated IR maps (which we rescaled using an appropriate factor as in [7] to match more recent constraints on IR source flux). The cross-spectrum of the resulting map with the simulated quasar maps gives a negative spurious signal which is $\approx 7\%$ of the theoretical prediction for the lensing-quasar cross-correlation. Repeating this analysis with the thermal SZ simulations gives a similar negative contamination of order $\approx 5\%$ of theory. (The analysis should overestimate the contamination, as the simulated quasars are placed exactly in the centers of the same halos that source the SZ and IR signal, neglecting any mis-centering effects.)

Any systematic error in our measurement of the lensing-quasar cross-power spectrum due to contamination from both IR and SZ sources should thus be significantly smaller than the size of the statistical error. In addition, the fact that these contamination signals are negative means that our detection of a positive lensing-quasar cross-power spectrum cannot be due to such systematics.

Finally, we estimate the level of contamination from galactic cirrus using the dust maps of [34]. We subtract a map of the signal at 148GHz induced by the dust (obtained from [28]) from the ACT temperature data, reconstruct lensing, and re-estimate the lensing-quasar cross-power spectrum. We find that the change in the cross-power spectrum is very small, of order 3% of the theoretical prediction for the lensing-quasar cross-spectrum. (This is unsurprising, as in our analysis large scale power below $\ell = 500$ has been filtered out of the temperature maps.) Contamination of the cross-power by galactic cirrus is thus negligible.

5.7 Summary and Conclusions

In this work we measure the cross-correlation between ACT CMB lensing maps and maps of the quasar distribution made from the SDSS-XDQSO catalog. We detect the cross-power spectrum at 3.8σ significance, directly confirming that quasars trace mass. We check our detection with null tests including a cross-correlation of quasars with the reconstructed curl component of lensing, which is found to be null as expected. Potential systematic contamination is estimated and found to be negligible. From our detection we estimate the quasar bias. We measure $b/b_{\rm fid} = 1.02 \pm 0.24$; interpreting this as a bias at $z \approx 1.4$ (the peak in the quasar distribution), we obtain $b = 2.5 \pm 0.6$ at this redshift (which corresponds to a host halo mass of $\log_{10}(M_{200}/M_\odot) = 12.9^{+0.3}_{-0.5}$). Unlike measurements from clustering, this lensing measurement involves a

direct comparison of the quasar distribution with the mass distribution, with little modeling required.

The study of high-redshift mass tracers with CMB lensing is a new field. In the next few years, the signal-to-noise ratio on lensing measurements should improve by an order of magnitude with data from experiments such as Planck, ACTPol and SPTPol [37, 35, 36]. ACTPol in particular should provide high signal-to-noise ratio lensing measurements which have considerable overlap with SDSS quasar fields. Higher signal-to-noise will allow constraints on quasar biases as a function of redshift, luminosity, color or other properties and will thus provide a wealth of information on the properties of quasars and the halos that host them. More precise bias measurements of both quasars and galaxies will also allow tests of dark energy properties [39] and modified gravity [38]. This work lies at the beginning of an exciting research program: the study of astrophysics and cosmology with CMB lensing cross-correlations.

5.8 Acknowledgements

We thank Jo Bovy and Michael Strauss for discussions and helpful comments on the draft, and acknowledge useful discussions with Kendrick Smith and Alex van Engelen. This work was supported by the U.S. NSF through awards AST-0408698, PHY-0355328, AST-0707731 and PIRE-0507768, as well as by Princeton Univ., the Univ. of Pennsylvania, FONDAP, Basal, Centre AIUC, RCUK Fellowship, NASA grant NNX08AH30G, NSERC PGSD, NSF PFC grant PHY-0114422, KICP Fellowship, SLAC no. DE-AC3-76SF00515, ERC grant 259505, BCCP, and the NSF GRFP. We thank B. Berger, R. Escribano, T. Evans, D. Faber, P. Gallardo, A. Gomez, M. Gordon, D. Holtz, M. McLaren, W. Page, R. Plimpton, D. Sanchez, O. Stryzak, M. Uehara, and Astro-Norte for assistance with ACT. ACT operates in the Parque Astronómico Atacama in northern Chile under the auspices of Programa de Astronomía,

a program of the Comisión Nacional de Investigación Científica y Tecnológica de Chile (CONICYT). Computations were performed on the GPC supercomputer at the SciNet HPC Consortium. SciNet is funded by the CFI under the auspices of Compute Canada, the Government of Ontario, the Ontario Research Fund – Research Excellence; and the University of Toronto.

References

[1] Lewis, A., & Challinor, A. 2006, Physics Reports, 429, 1

[2] Hanson, D., Challinor, A., Efstathiou, G., & Bielewicz, P. 2011, Phys. Rev. D, 83, 043005

[3] Hu, W., & Okamoto, T. 2002, ApJ, 574, 566

[4] Smith, K. M., Zahn, O., & Doré, O. 2007, Phys. Rev. D, 76, 043510

[5] Hirata, C. M., Ho, S., Padmanabhan, N., Seljak, U., & Bahcall, N. A. 2008, Phys. Rev. D, 78, 043520

[6] Das, S., Sherwin, B. D., Aguirre, P., et al. 2011, Physical Review Letters, 107, 021301

[7] van Engelen, A., Keisler, R., Zahn, O., et al. 2012, arXiv:1202.0546

[8] Bleem, L. E., van Engelen, A., Holder, G. P., et al. 2012, arXiv:1203.4808

[9] Bucher, M., & Louis, T. 2011, arXiv:1109.0286

[10] de Putter, R., Zahn, O., & Linder, E. V. 2009, Phys. Rev. D, 79, 065033

[11] Lesgourgues, J., Perotto, L., Pastor, S., & Piat, M. 2006, Phys. Rev. D, 73, 045021

[12] Salpeter, E. E. 1964, ApJ, 140, 796

[13] Lynden-Bell, D. 1969, Nature, 223, 690

[14] Kormendy, J., & Richstone, D. 1995, ARA&A, 33, 581

[15] Nandra, K., Georgakakis, A., Willmer, C. N. A., et al. 2007, ApJ, 660, L11

[16] White, M., Myers, A. D., Ross, N. P., et al. 2012, Mon. Not. R. Astron. Soc, 424, 933

[17] Peiris, H. V., & Spergel, D. N. 2000, ApJ, 540, 605

[18] Sherwin, B. D., Dunkley, J., Das, S., et al. 2011, Physical Review Letters, 107, 021302

[19] Komatsu, E., Dunkley, J., Nolta, M. R., et al. 2009, ApJS, 180, 330

[20] Limber, D. N. 1954, ApJ, 119, 655

[21] Bovy, J., Hennawi, J. F., Hogg, D. W., et al. 2011, ApJ, 729, 141

[22] Bovy, J., Myers, A. D., Hennawi, J. F., et al. 2012, ApJ, 749, 41

[23] Fowler, J. W., Niemack, M. D., Dicker, S. R., et al. 2007, Applied Optics, 46, 3444

[24] Dunner, R., Hasselfield, M., Marriage, T. M., et al. in prep.

[25] Swetz, D. S., Ade, P. A. R., Amiri, M., et al. 2011, ApJS, 194, 41

[26] Hajian, A., Acquaviva, V., Ade, P. A. R., et al. 2011, ApJ, 740, 86

[27] Annis, J., Soares-Santos, M., Strauss, M. A., et al. 2011, arXiv:1111.6619

[28] Sehgal, N., Bode, P., Das, S., et al. 2010, ApJ, 709, 920

[29] Lewis, A., Challinor, A., & Lasenby, A. 2000, ApJ, 538, 473

[30] Smith, R. E., Peacock, J. A., Jenkins, A., et al. 2003, Mon. Not. R. Astron. Soc, 341, 1311

[31] Shen, Y., Strauss, M. A., Ross, N. P., et al. 2009, ApJ, 697, 1656

[32] Tinker, J. L., Robertson, B. E., Kravtsov, A. V., et al. 2010, ApJ, 724, 878

[33] Reichardt, C. L., Shaw, L., Zahn, O., et al. 2011, arXiv:1111.0932

[34] Schlegel, D. J., Finkbeiner, D. P., & Davis, M. 1998, ApJ, 500, 525

[35] Niemack, M. D., Ade, P. A. R., Aguirre, J., et al. 2010, Proc. SPIE, 7741

[36] McMahon, J. J., Aird, K. A., Benson, B. A., et al. 2009, American Institute of Physics Conference Series, 1185, 511

[37] Planck Collaboration XVIII 2011, A&A, 536, A18

[38] Acquaviva, V., Hajian, A., Spergel, D. N., & Das, S. 2008, Phys. Rev. D, 78, 043514

[39] Das, S., & Spergel, D. N. 2009, Phys. Rev. D, 79, 043509

Chapter 6

CMB Lensing: Power Without Bias

6.1 Abstract

We propose a novel bias-free method for reconstructing the power spectrum of the weak lensing deflection field from cosmic microwave background (CMB) observations. The proposed method is in contrast to the standard method of CMB lensing reconstruction where a reconstruction bias needs to be subtracted to estimate the lensing power spectrum. This bias depends very sensitively on the modeling of the signal and noise properties of the survey, and a misestimate can lead to significantly inaccurate results. Our method obviates this bias and hence the need to characterize the detailed noise properties of the CMB experiment. We illustrate our method with simulated lensed CMB maps with realistic noise distributions. This bias-free method can also be extended to create much more reliable estimators for other four-point functions in cosmology, such as those appearing in primordial non-Gaussianity estimators.

6.2 Bias-free Lensing Power Spectrum Measurements

The power spectrum of the lensing deflection field is sensitive to both the geometry of the universe and the growth of structure over a broad redshift range ($z \sim 0.5-5$). As such, knowledge of the convergence field can provide strong constraints on parameters that affect geometry or the growth at later times, such as the sum of neutrino masses and parametrizations of non-standard dark energy behavior [2]. These constraints are complementary to those obtained directly from the primordial CMB anisotropies. In the very near future, ongoing and upcoming CMB experiments, such as Planck, ACT, SPT, PolarBear, ACTPol and SPTPol will produce datasets with sufficient resolution and sensitivity to begin the mapping of the deflection field and realize the cosmological potential of CMB lensing science. Robust algorithms that are insensitive to the details of the noise properties of the survey will be essential for accurate determination of the deflection power spectrum.

In this Chapter, we propose a novel and *bias-free* technique for the measurement of the lensing deflection power spectrum. This is in contrast to the standard optimal quadratic estimator (OQE) method where a bias term, comparable to and often much larger than the signal, has to be subtracted (for details, see [3, 4]). This bias, which is a temperature-field four point function that depends on noise and foregrounds, must typically be computed or simulated to an accuracy of a few percent in order to get reliable estimation of the signal. Because of our limited knowledge of the temperature and polarization foregrounds, and the typically complicated noise properties of CMB experiments, modeling this bias term sufficiently accurately for a robust detection of lensing may be difficult.

To discuss how this bias appears and can be avoided, we will review some lensing theory here. The lensed and unlensed temperature fields (unlensed quantities will be

denoted by a tilde) are related by $T(\hat{\mathbf{n}}) = \tilde{T}(\hat{\mathbf{n}} + \mathbf{d}(\hat{\mathbf{n}}))$, where $\mathbf{d}(\hat{\mathbf{n}})$ is the deflection field and $\kappa = -\frac{1}{2}\nabla \cdot \mathbf{d}$ is the convergence field. In the flat sky approximation, the temperature field can be expanded as a Taylor series in Fourier space [5, 6]:

$$T(\mathbf{l}) = \tilde{T}(\mathbf{l}) + 2\int \frac{d^2\mathbf{l}'}{(2\pi)^2} \frac{\mathbf{l}' \cdot (\mathbf{l} - \mathbf{l}')}{|\mathbf{l} - \mathbf{l}'|^2} \kappa(\mathbf{l} - \mathbf{l}')\tilde{T}(\mathbf{l}') + O(\kappa^2). \tag{6.1}$$

Thus, gravitational lensing introduces correlations between the formerly independent modes of the temperature field, which can be used to construct a quadratic estimator for κ:

$$\begin{aligned} \hat{\kappa}(\mathbf{L}) &= N^{\kappa}(\mathbf{L}) \int \frac{d^2\mathbf{l}}{(2\pi)^2}\, \mathbf{L} \cdot (\mathbf{L} - \mathbf{l}) \\ &\quad \times F_W(\mathbf{l}) T(\mathbf{l}) F_G(|\mathbf{L} - \mathbf{l}|) T(\mathbf{L} - \mathbf{l}). \end{aligned} \tag{6.2}$$

where N^{κ} is a normalization that ensures that the estimator is unbiased (i.e., $\langle \hat{\kappa} \rangle_{\mathrm{CMB}} = \kappa$) and F_W and F_G are filters that can be tuned to minimize its variance [3]. Here we will use notation from [4] and denote ensemble averages over CMB realizations with the large scale structure (LSS) fixed as $\langle ... \rangle_{\mathrm{CMB}}$, and averages over LSS realizations as $\langle ... \rangle_{\mathrm{LSS}}$, and use $\langle ... \rangle$ to denote ensemble averages over both, i.e., $\langle \langle ... \rangle_{\mathrm{CMB}} \rangle_{\mathrm{LSS}}$.

While equation (6.2) provides an unbiased estimate of the convergence field, the naive lensing power spectrum estimator $\hat{\kappa}^*(\mathbf{L})\hat{\kappa}(\mathbf{L})$ is highly biased:

$$\begin{aligned}
\langle\hat{\kappa}^*(\mathbf{L})\hat{\kappa}(\mathbf{L}')\rangle &= N^{\kappa*}(\mathbf{L})N^{\kappa}(\mathbf{L}') \\
&\quad \int\frac{d^2\mathbf{l}}{(2\pi)^2}\int\frac{d^2\mathbf{l}'}{(2\pi)^2}g(\mathbf{l},\mathbf{L})g(\mathbf{l}',\mathbf{L}') \\
&\quad \times\langle\langle T^*(\mathbf{l})\,T^*(\mathbf{L}-\mathbf{l})\,T(\mathbf{l}')\,T(\mathbf{L}'-\mathbf{l}')\rangle_{\rm CMB}\rangle_{\rm LSS} \qquad (6.3)\\
&\simeq (2\pi)^2\delta(\mathbf{L}-\mathbf{L}')C_L^{\kappa} \\
&\quad + N^{\kappa*}(\mathbf{L})N^{\kappa}(\mathbf{L}') \\
&\quad \times\int\frac{d^2\mathbf{l}}{(2\pi)^2}\int\frac{d^2\mathbf{l}'}{(2\pi)^2}g(\mathbf{l},\mathbf{L})g(\mathbf{l}',\mathbf{L}') \\
&\quad \times\left\langle\tilde{T}^*(\mathbf{l})\,\tilde{T}^*(\mathbf{L}-\mathbf{l})\,\tilde{T}(\mathbf{l}')\,\tilde{T}(\mathbf{L}'-\mathbf{l}')\right\rangle_{\rm CMB} \qquad (6.4)
\end{aligned}$$

where $g(\mathbf{l},\mathbf{L}) = \mathbf{L}\cdot(\mathbf{L}-\mathbf{l})F_W(\mathbf{l})F_G(|\mathbf{L}-\mathbf{l}|)$. In going from the first equality above to the second, we have neglected a few terms that appear involving integrals over the convergence power spectrum. These higher order terms are computed in [4] and are subdominant compared to the Gaussian four point term above. Applying Wick's theorem contractions to the four-point term, the above equation can be reduced to:

$$\langle\hat{\kappa}^*(\mathbf{L})\hat{\kappa}(\mathbf{L}')\rangle = (2\pi)^2\delta(\mathbf{L}-\mathbf{L}')(C_L^{\kappa}+C_L^{\kappa,\rm Gauss}),$$

where

$$\begin{aligned}
C_{\mathbf{L}}^{\kappa,\rm Gauss} &= N^{\kappa*}(\mathbf{L})N^{\kappa}(\mathbf{L})\int\frac{d^2\mathbf{l}}{(2\pi)^2}\int\frac{d^2\mathbf{l}'}{(2\pi)^2}f(\mathbf{l},\mathbf{l}',\mathbf{L}) \\
&\quad \big[C_{\mathbf{l}}C_{\mathbf{L}-\mathbf{l}}(2\pi)^2\delta(\mathbf{l}'-\mathbf{l}) \\
&\quad +C_{\mathbf{l}}C_{\mathbf{L}-\mathbf{l}}(2\pi)^2\delta\left(\mathbf{l}'-(\mathbf{L}-\mathbf{l})\right)\big]\,, \qquad (6.5)
\end{aligned}$$

with $f(\mathbf{l},\mathbf{l}',\mathbf{L}) = g(\mathbf{l},\mathbf{L})\;g(\mathbf{l}',\mathbf{L}')$. This expression shows that the Gaussian bias $C_{\mathbf{L}}^{\kappa,\rm Gauss}$ depends on the map power spectrum estimate which is usually a sum of

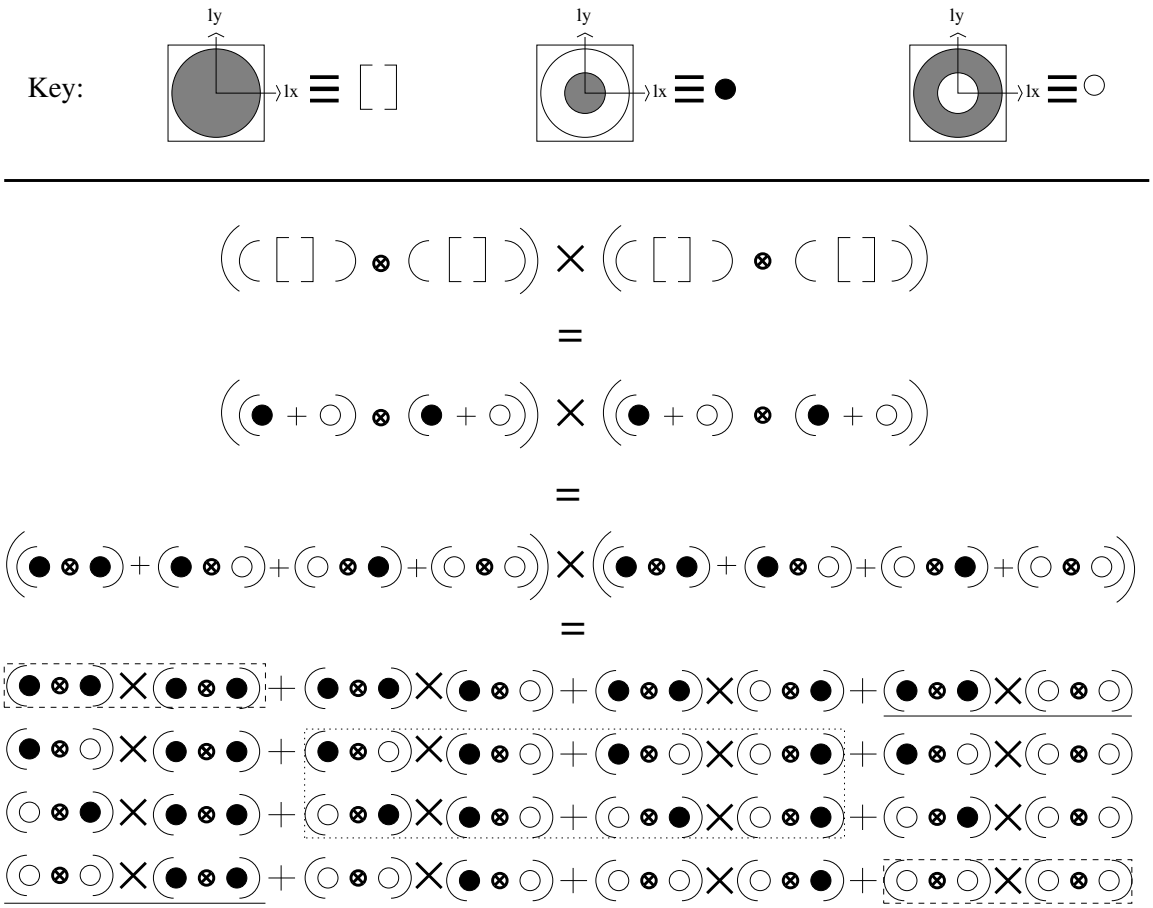

Figure 6.1: Graphical expansion of the naive estimator after splitting up the Fourier space into an inner and an outer annulus. We use the linearity of both operators in this expansion. The terms with Gaussian bias are shown enclosed by boxes. The underlined terms (identical by symmetry) are implemented in the simulations described in this paper to illustrate the method.

the CMB temperature power spectrum, foregrounds, and noise. Since the Gaussian bias term is typically more than an order of magnitude larger than the intrinsic lensing signal C_ℓ^κ, the standard approach to estimating lensing requires a detailed understanding of each of these contributions.

The goal of this paper is to eliminate the need to compute this Gaussian bias term at the percent level by eliminating the bias altogether. One way to achieve this would be to perform the double two-dimensional integral explicitly in (6.3) with the

following conditions imposed on the function f:

$$f(\mathbf{l},\mathbf{l}',\mathbf{L}) = \begin{cases} 0 & \text{if } \mathbf{l}' = \mathbf{l} \text{ or } \mathbf{l}' = \mathbf{L}-\mathbf{l} \\ f(\mathbf{l},\mathbf{l}',\mathbf{L}) & \text{otherwise.} \end{cases} \tag{6.6}$$

which is equivalent to using the power spectrum of the measured data to calculate the bias. However, in realistic maps with window functions and anisotropic noise even this expression may not be precisely correct. A different method of eliminating the bias, which can also be used as a test of other methods of estimation, would be to partition the Fourier space into non-overlapping annuli, and cross correlate the $\kappa(\mathbf{L})$'s reconstructed from temperature modes in two disjoint annuli. To formulate this fully, let us introduce some compact notation. Let us denote the operation of reconstructing κ from two temperature maps, equation (6.2), as $\kappa = (T \otimes T)$ where all quantities are understood to be in Fourier ($\mathbf{l}$) space. Now, the naive estimator for the convergence power spectrum (6.3) can be written as $\hat{\kappa}^*\hat{\kappa} = (T \otimes T) \times (T \otimes T)$. Now consider breaking up $T(\mathbf{l})$ into two Fourier space maps, one which has non-zero elements only with an annulus $\ell_0 < \ell < \ell_1$ (the "in-annulus") and another which has non-zero values in $\ell_1 < \ell < \ell_2$ (the "out-annulus"), where $\ell_0 < \ell_1 < \ell_2$. Writing $T(\mathbf{l}) = T_{\rm in}(\mathbf{l}) + T_{\rm out}(\mathbf{l})$, the naive power spectrum estimator can be written out as,

$$\begin{aligned} \hat{C}_{\mathbf{l}}^{\kappa,\rm naive} &= (T \otimes T) \times (T \otimes T) \\ &= ((T_{in} + T_{out}) \otimes (T_{in} + T_{out})) \\ &\times ((T_{in} + T_{out}) \otimes (T_{in} + T_{out})). \end{aligned} \tag{6.7}$$

We have expanded this out graphically in Fig. 6.1. In this figure, we represent the in-annulus by a filled circle and the out-annulus by an empty circle. The expansion leads to 16 terms, some of which are identical due to symmetry. Note that the Gaussian bias associated with each term evaluates to a sum of two terms from two possible

Wick's theorem pairings (one member of the pair being taken from either side of the "×" sign). Those terms (e.g. $(T_{in} \otimes T_{in}) \times (T_{out} \otimes T_{out})$, underlined in Fig. 6.1) where either pairing leads to at least one product of an out-annulus with an in-annulus will have contributions to the bias which evaluate out to zero. We find 10 such terms in Fig. 6.1; the remaining 6 terms' biases have non-zero expectation value and hence contribute to the total bias (these terms are shown enclosed by boxes). Therefore, one can construct a new estimator for the convergence power spectrum by applying these annular filters and optimally combining the 10 terms (some of these are identical) that are bias-free. Of course, eliminating bias comes at the cost of reducing the signal-to-noise because we throw out a fraction of terms with information. In principle, higher signal-to-noise can be achieved by further subdividing each annulus into an inner and an outer part, and iterating the method, thereby reducing the ratio of the number of biased to bias-free terms.

There are a few details that need to be taken into account when applying this method to a real experiment. For a partial sky map, nearby Fourier modes will be coupled by the power spectrum of the data-window with some characteristic width $\Delta\ell$. There can be additional effects such as coupling of nearby modes induced by anisotropic noise. In general, if the effective width $\Delta\ell$ of such correlations is known, the above method needs to modified by separating the two annuli by some small multiple of $\Delta\ell$. This will ensure that our annular method for eliminating the Gaussian bias works despite these correllations due to systematics.

Due to the annuli being separated by $\Delta\ell$, all the terms involving a convergence map obtained from an innner annulus as well as an outer annulus are undefined for $\ell < \Delta\ell$ (as can be deduced from equation 6.2). Hence, for a simple bias-free estimator we used only the terms underlined in Fig. 6.1: those with one "in–in" convergence map crossed with one "out–out" convergence map, so that the new bias free estimator

is:

$$\hat{C}_{\mathbf{l}}^{\kappa,\mathrm{bias-free}} = (T_{in} \otimes T_{in}) \times (T_{out} \otimes T_{out}) \tag{6.8}$$

There is one further subtlety to the reconstruction of the convergence power spectrum. Window function correlations due to finite maps and anisotropic noise not only affect the Gaussian bias, but also appear more directly as a spurious lensing signal in the reconstructed convergence maps. This spurious convergence, $\langle\tilde{\kappa}\rangle$, needs to be simulated and subtracted off from the reconstructed $\hat{\kappa}$ map. To determine whether the reconstructed convergence power is sensitive to the accuracy of the simulation of $\langle\tilde{\kappa}\rangle$, we must determine the magnitude of $C_{\mathbf{l}}^{\langle\tilde{\kappa}\rangle_{in,in}\langle\tilde{\kappa}\rangle_{out,out}}$ (where one must distinguish between the two $\langle\tilde{\kappa}\rangle$ fields because they are simulated with different annular filters). From our Monte Carlo simulations, which we describe below, we find the following: for our bias-free lensing estimators, $C_{\mathbf{l}}^{\langle\tilde{\kappa}\rangle_{in,in}\langle\tilde{\kappa}\rangle_{out,out}}$ appears consistent with null and is typically two orders of magnitude smaller than the true convergence power C_ℓ^κ and three orders of magnitude smaller than the previously discussed reconstruction bias. We also verified that the results of our simulations plotted below are the same whether or not we subtract $\langle\tilde{\kappa}\rangle$ from $\hat{\kappa}$. The accuracy of the simulation of the spurious signal $\langle\tilde{\kappa}\rangle$ thus seems to only have a negligible influence on how well the lensing power spectrum is reconstructed.

We illustrate our method for bias-free lensing power reconstruction by performing Monte Carlo simulations, loosely modeled on the observations made by the Atacama Cosmology Telescope (ACT). We choose our survey geometry to be an oblong $5^\circ \times 60^\circ$ stripe, divided into four adjacent patches of $5^\circ \times 15^\circ$ each. We simulate convergence maps on these patches from an input power spectrum, and generate deflection fields from the convergence maps. We also generate Gaussian random realizations of unlensed CMB maps from an input power spectrum, which we subsequently lens using the simulated deflection field. Then we smooth the maps with the ACT beam (1.4 arcmin full-width-half-maximum), and add noise. We perform two variations on the

noise. In the first version, we add white noise at the level of 2 μK-arcmin. In the second version, we simulate noise seeded by the noise power spectrum realized in the maps from ACT. These simulations capture the non-white and anisotropic aspects of the noise in ACT maps (for the detailed procedure see [7]). To ensure that the reconstructed convergence power spectrum is not too noisy (so that the Monte Carlo simulations rapidly converge), we reduce the amplitude of the simulated noise by a factor of three over what is observed in ACT maps. These maps are roughly 10 μK-arcmin in noise. For each type of noise, we simulate 120 realizations of the full map by randomizing the CMB, the convergence and the noise. We then apply the bias-free convergence power spectrum estimator method to each random realization of the noisy maps. We apply this both to lensed maps with noise and as a null test also to unlensed maps with noise. We define our annular filters such that the inner annulus is $\ell = (500 - 1500)$, the outer annulus is $\ell = (1900 - 3300)$, so that $\Delta\ell = 400$.

The results are shown in Fig. 6.2. This figure shows that in both cases our method is able to extract the convergence power spectrum without bias (note that a small amount of bias from higher order terms discussed in Kesden et al. [4] is present in the reconstruction). The figure also shows that with noisy but unlensed CMB maps, the measurements are consistent with a null signal.

Finally, we should point out some caveats. Here we have assumed CMB as the only signal. In reality, emission from point sources and the thermal and kinetic Sunyaev-Zeldovich effects contribute to mm-wave maps. Also, noise correlations in real experiments can be more complicated than what is simulated here. There are also other subdominant sources of reconstruction bias, such as those discussed in [4] and [8]. More work will be needed to characterize these foregrounds and biases in context of our new method. These will be discussed in a future, more detailed work.

It should be noted that our approach for bias-free lensing convergence reconstruction can be easily extended to estimating other four-point-functions in cosmology, such as the estimators of primordial non-Gaussianity.

6.3 Acknowledgements

BDS and SD would like to acknowledge fruitful discussions with Kavilan Moodley and thank David Spergel, Kendrick Smith, Lyman Page and Suzanne Staggs for their advice and feedback. BDS also acknowledges the hospitality of the BCCP during the development of this paper. Computations were performed on the GPC supercomputer at the SciNet HPC Consortium. SciNet is funded by: the Canada Foundation for Innovation under the auspices of Compute Canada; the Government of Ontario; Ontario Research Fund - Research Excellence; and the University of Toronto. This project was partially supported by NSF grant 0707731 and NASA grant NNX08AH30G. BDS is supported by a National Science Foundation Graduate Research Fellowship. SD is supported by a Berkeley Center for Cosmological Physics postdoctoral fellowship.

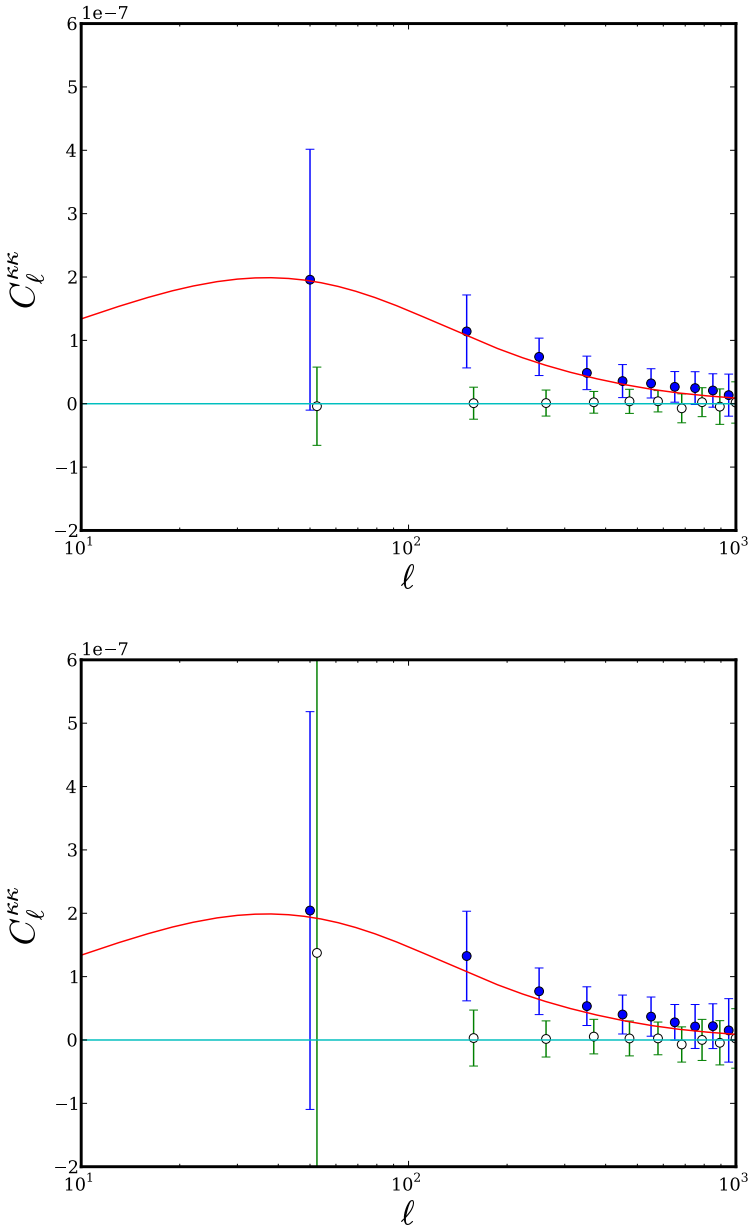

Figure 6.2: *Upper image:* Convergence power spectrum reconstructed with the proposed Gaussian bias-free method from four $5^\circ \times 15^\circ$ patches with simulated CMB signal with 2 μK-arcmin white noise. The blue (filled) circles show the mean of 120 Monte Carlo realizations with lensed CMB, while the green (empty) circles show the same for unlensed CMB maps. The error bars are estimated from the scatter between Monte Carlo runs and are representative of the uncertainty expected in one realization; the lensed errors are higher than the null errors due to the presence of a sample variance component. The red continuous curve is the input theory for the convergence field power spectrum. *Lower image:* Same as left, but for non-white and anisotropic noise simulations seeded by noise in ACT maps, reduced in amplitude by a factor of 3.

References

[1] Lewis, A., & Challinor, A., 2006, Physics Reports, 429, 1

[2] Smith, K. M. et al., 2008, arXiv:0811.3916

[3] Hu, W. & Okamoto, T., 2002, Phys. Rev. D, 083002

[4] Kesden, M., Cooray, A., Kamionkowski, M., 2003, Phys. Rev. D, 67, 123507

[5] Zaldarriaga, M. & Seljak, U., 1998, Phys. Rev. D, 58, 023003

[6] Seljak, U., & Zaldarriaga, M., 1999, Phys. Rev. Lett., 82, 2636

[7] Das, S. et al., 2011, ApJ, 729, 62

[8] Hanson, D., Challinor, A., Efstathiou, G., & Bielewicz, P., 2011, Phys. Rev. D, 83, 043005

Chapter 7

A Measurement of the Skewness of the Thermal Sunyaev-Zeldovich Effect

7.1 Abstract

We present a detection of the unnormalized skewness $\left\langle \tilde{T}^3(\hat{\mathbf{n}}) \right\rangle$ induced by the thermal Sunyaev-Zel'dovich (tSZ) effect in filtered Atacama Cosmology Telescope (ACT) 148 GHz cosmic microwave background temperature maps. Contamination due to infrared and radio sources is minimized by template subtraction of resolved sources and by constructing a mask using outlying values in the 218 GHz (tSZ-null) ACT maps. We measure $\left\langle \tilde{T}^3(\hat{\mathbf{n}}) \right\rangle = -31 \pm 6\ \mu\mathrm{K}^3$ (Gaussian statistics assumed) or $\pm 14\ \mu\mathrm{K}^3$ (including non-Gaussian corrections) in the filtered ACT data, a 5σ detection. We show that the skewness is a sensitive probe of σ_8, and use analytic calculations and tSZ simulations to obtain cosmological constraints from this measurement. From this signal alone we infer a value of $\sigma_8 = 0.79^{+0.03}_{-0.03}$ (68% C.L.) $^{+0.06}_{-0.06}$ (95% C.L.). Our re-

sults demonstrate that measurements of non-Gaussianity can be a useful method for characterizing the tSZ effect and extracting the underlying cosmological information.

7.2 Introduction

Current observations of the cosmic microwave background (CMB) anisotropies on arcminute scales using experiments such as the Atacama Cosmology Telescope [ACT; 1, 3, 2] and the South Pole Telescope [SPT; 4, 5] probe not only the primordial microwave background fluctuations sourced 13.7 billion years ago, but also measure secondary anisotropies caused by more recent and less distant physical processes. Such secondary anisotropies are induced by infrared (IR) dusty galaxies and radio sources, gravitational lensing, and the Sunyaev-Zel'dovich (SZ) effect. The SZ effect [6, 7] arises due to the inverse Compton scattering of CMB photons off high energy electrons located predominantly in hot gas in galaxy clusters (the intra-cluster medium, or ICM). This scattering modifies the spectrum of CMB photons in the direction of a cluster in a way that depends on both the thermal energy contained in the ICM (the thermal SZ effect) as well as the peculiar velocity of the cluster with respect to the CMB rest frame (the kinetic SZ effect). The kinetic SZ effect simply increases or decreases the amplitude of the CMB spectrum in the direction of a cluster, but the thermal SZ (tSZ) effect modifies the CMB spectrum in a frequency-dependent manner. The tSZ effect is characterized by a decrease (increase) in the observed CMB temperature at frequencies below (above) 218 GHz in the direction of a galaxy cluster due to inverse Compton scattering. The thermal effect is generally at least an order of magnitude larger than the kinetic effect for a typical massive cluster at 148 GHz. Measurements of the tSZ signal, which is proportional to the integrated ICM pressure along the line of sight, can be used to observe the high redshift universe, constrain

cosmological parameters – in particular σ_8, the variance of matter fluctuations on scales of 8 Mpc/h – and probe baryonic physics in the ICM.

The tSZ signal has so far primarily been studied either by directly resolving individual clusters in arcminute-scale CMB maps [8, 9, 10, 11, 12] or by measuring it statistically through its presence in the small-scale CMB power spectrum [13, 14]. However, it is by no means obvious that the power spectrum is the best way to characterize the statistical properties of the tSZ field. Indeed, measuring the tSZ signal in the power spectrum is challenging because there are many other sources of CMB power on arcminute scales: primordial CMB fluctuations, CMB lensing, instrumental noise, dusty star-forming IR galaxies, and radio sources. In order to disentangle these contributions to the power spectrum and isolate the amplitude of the tSZ signal, a sophisticated multifrequency analysis is required, which involves modeling the power spectrum contribution of each of these components in at least two frequency bands.

In this paper we instead measure the tSZ signal using the unnormalized skewness of the filtered temperature fluctuation $\left\langle \tilde{T}^3(\hat{\mathbf{n}}) \right\rangle$. This quantity has the significant advantage that, unlike measurements of the tSZ effect through the power spectrum, its measurement does not require the subtraction of Gaussian contributions, because it is only sensitive to non-Gaussian signals with non-zero skewness. The primordial CMB (which is assumed to be Gaussian on these scales) and instrumental noise (which is Gaussian) hence do not contribute to it. In addition, CMB lensing and the kinetic SZ effect do not induce skewness (as they are equally likely to produce positive and negative fluctuations), and so do not contribute either. The primary contributions to this quantity are thus only the tSZ effect and point sources. These signals have a different frequency dependence. Furthermore, the tSZ signal contributes negative skewness, whereas radio and IR point sources contribute positive skewness. These characteristics allow the tSZ signal to be effectively isolated and studied, as first pointed out in [15].

Measurements of the skewness also possess significant advantages from an astrophysical perspective. A consistent problem plaguing studies of the tSZ power spectrum has been theoretical uncertainty in the ICM electron pressure profile [16, 17, 18], especially in the low-mass, high-redshift groups and clusters that contribute much of the signal. As discussed in the following section in detail, the tSZ skewness signal is dominated by characteristically higher-mass, lower-redshift clusters than those that source the power spectrum signal. The ICM astrophysics for these objects is better constrained by X-ray observations and they are less sensitive to energy input from non-gravitational sources [18, 19]. Thus, the theoretical systematic uncertainty in modeling the tSZ skewness is correspondingly lower as well. In addition, at 148 GHz, dusty star-forming galaxies are less prevalent in massive, low-redshift clusters (which contribute more to the skewness) than in high-redshift groups and clusters (which contribute more to the tSZ power spectrum) [20]. Thus, we expect the correlation between tSZ signal and dusty galaxy emission, which can complicate analyses of the tSZ effect, to be smaller for a measurement of the skewness.

Moreover, the tSZ skewness scales with a higher power of σ_8 than the tSZ power spectrum amplitude. This result is precisely what one would expect if the signal were dominated by higher-mass, rarer objects, as the high-mass tail of the mass function is particularly sensitive to a change in σ_8. This provides the prospect of tight constraints on cosmological parameters from the skewness that are competitive with constraints from the power spectrum.

In this paper, we first explain the usefulness of the skewness as a cosmological probe by theoretically deriving its scaling with σ_8 as well as the characteristic masses of the objects sourcing the signal. Subsequent sections of the paper describe how we measured this skewness in the ACT data. We describe how the ACT temperature maps are processed in order to make a reliable measurement of the unnormalized skewness due to the tSZ effect, and discuss how contamination from IR dusty galaxies

and radio point sources is minimized. We report the measurement results and discuss how the errors are calculated. Finally, we discuss the cosmological constraints and associated uncertainties derived from this measurement.

We assume a flat ΛCDM cosmology throughout, with parameters set to their WMAP5 values [21] unless otherwise specified. All masses are quoted in units of $M_\odot/h$, where $h \equiv H_0/(100\,\mathrm{km\,s^{-1}\,Mpc^{-1}})$ and H_0 is the Hubble parameter today.

7.3 Skewness of the tSZ Effect

In this section, we investigate the N^{th} moments of the pixel probability density function, $\langle T^N \rangle \equiv \langle T(\hat{\mathbf{n}})^N \rangle$, focusing on the specific case of the unnormalized skewness $\langle T^3 \rangle$. We show that the unnormalized skewness $\langle T^3 \rangle$ has a steeper scaling with σ_8 than the power spectrum amplitude and is dominated by characteristically higher-mass, lower-redshift clusters, for which the ICM astrophysics is better constrained and modeled. As explained earlier, these characteristics make tSZ skewness measurements a useful cosmological probe.

In order to calculate the N^{th} moment of the tSZ field, we assume the distribution of clusters on the sky can be adequately described by a Poisson distribution (and that contributions due to clustering and overlapping sources are negligible [22]). The N^{th} moment is then given by

$$\langle T^N \rangle = \int dz \frac{dV}{dz} \int dM \frac{dn(M,z)}{dM} \int d^2\boldsymbol{\theta}\, T(\boldsymbol{\theta}; M, z)^N \,, \tag{7.1}$$

where $T(\boldsymbol{\theta}; M, z)$ is the tSZ temperature decrement at position $\boldsymbol{\theta}$ on the sky with respect to the center of a cluster of mass M at redshift z:

$$\begin{aligned} T(\boldsymbol{\theta}; M, z) &= g(\nu) T_{\rm CMB} \frac{\sigma_T}{m_e c^2} \\ &\times \int P_e\left(\sqrt{l^2 + d_A^2(z)|\boldsymbol{\theta}|^2}; M, z\right) dl\,, \end{aligned} \tag{7.2}$$

where $g(\nu)$ is the spectral function of the tSZ effect, $d_A(z)$ is the angular diameter distance to redshift z, and the integral is taken over the electron pressure profile $P_e(\boldsymbol{r}; M, z)$ along the line of sight.

For a given cosmology, Eqs. (7.1) and (7.2) show that there are two ingredients needed to calculate the $N^{\rm th}$ tSZ moment (in addition to the comoving volume per steradian dV/dz, which can be calculated easily): (1) the halo mass function $dn(M, z)/dM$ and (2) the electron pressure profile $P_e(\boldsymbol{r}; M, z)$ for halos of mass M at redshift z. We use the halo mass function of [23] with the redshift-dependent parameters given in their Eqs. (5)–(8). While uncertainties in tSZ calculations due to the mass function are often neglected, they may be more important for the skewness than the power spectrum, as the skewness is more sensitive to the high-mass exponential tail of the mass function. We estimate the uncertainty arising from the mass function by performing alternate calculations with the mass function of [24], which predicts more massive clusters at low redshift than [23] for the same cosmology. As an example, the predicted skewness calculated using the pressure profile of [16] with the mass function of [23] is $\approx 35\%$ lower than the equivalent result using the mass function of [24]. However, the derived scalings of the variance and skewness with σ_8 computed using [24] are identical to those found below using [23]. Thus, the scalings calculated below are robust to uncertainties in the mass function, and we use them later to interpret our skewness measurement. However, we rely on cosmological sim-

ulations to obtain predicted values of the tSZ skewness. We do not consider alternate mass functions any further in our analytic calculations.

We consider three different pressure profiles from [16, 17, 25] in order to evaluate the theoretical uncertainty in the scaling of the tSZ skewness with σ_8. These profiles differ in how they are derived and in the ICM physics they assume. They thus provide a measure of the scatter in the scalings of the variance and skewness with σ_8 due to uncertainties in the gas physics.

Finally, in order to make a faithful comparison between the theory and data, we convolve Eq. (7.2) with the Fourier-space filter described in the subsequent data analysis sections of this paper. In addition, we account for the 12σ pixel fluctuation cutoff used in the data analysis (see below) by placing each "cluster" of mass M and redshift z in the integrals of Eq. (7.1) in an idealized ACT pixel and computing the observed temperature decrement, accounting carefully for geometric effects that can arise depending on the alignment of the cluster and pixel centers. If the calculated temperature decrement exceeds the 12σ cutoff, then we do not include this cluster in the integrals. These steps cannot be neglected, as the filter and cutoff reduce the predicted tSZ skewness amplitude by up to 95% compared to the pure theoretical value [26]. Most of this reduction is due to the filter, which modestly suppresses the temperature decrement profile of a typical cluster; this suppression strongly affects the skewness because it is a cubic statistic.

The analytic theory described above determines the scaling of the $N^{\rm th}$ tSZ moment with σ_8. In particular, we compute Eq. (7.1) with $N = 2$, $N = 3$, and $N = 6$ for each of the chosen pressure profiles while varying σ_8. The scalings of the variance ($N = 2$), the skewness ($N = 3$), and the sixth moment ($N = 6$, which we require for error calculation) with σ_8 are well-described by power laws for each of these profiles: $\left\langle \tilde{T}^{2,3,6} \right\rangle \propto \sigma_8^{\alpha_{2,3,6}}$. For the profile of [16], we find $\alpha_2 = 7.8$, $\alpha_3 = 11.1$, and $\alpha_6 = 16.7$; for the profile of [17], we find $\alpha_2 = 8.0$, $\alpha_3 = 11.2$, and $\alpha_6 = 15.9$; and for the

profile of [25], we find $\alpha_2 = 7.6$, $\alpha_3 = 10.7$, and $\alpha_6 = 18.0$. Note that the scaling of the variance matches the scaling of the tSZ power spectrum amplitude that has been found by a number of other studies, as expected (e.g., [25, 27]). The scaling of the unnormalized skewness is similar to that found by [28], who obtained $\alpha_3 = 10.25$. Also, note that the skewness scaling is modified slightly from its pure theoretical value [26] due to the Fourier-space filter and pixel fluctuation cutoff mentioned above. The overall conclusion is that the skewness scales with a higher power of σ_8 than the variance (or power spectrum). We use this scaling to derive a constraint on σ_8 from our measurement of the skewness below.

In addition, we compare the characteristic mass scale responsible for the tSZ skewness and tSZ variance (or power spectrum) signals. Analytic calculations show that the tSZ power spectrum amplitude typically receives $\approx 50\%$ of its value from halos with $M < 2$–3×10^{14} $\mathrm{M}_\odot/h$, while the tSZ skewness receives only $\approx 20\%$ of its amplitude from these less massive objects. This indicates that the clusters responsible for the tSZ skewness signal are better theoretically modeled than those responsible for much of the tSZ power spectrum, both because massive clusters have been observed more thoroughly, and because more massive clusters are dominated by gravitational heating and are less sensitive to non-linear energy input from active galactic nuclei, turbulence, and other mechanisms [18, 19]. We verify this claim when interpreting the skewness measurement below, finding that the systematic theoretical uncertainty (as derived from simulations) is slightly smaller than the statistical error from the measurement, though still non-negligible.

7.4 Map Processing

7.4.1 Filtering the Maps

The Atacama Cosmology Telescope [1, 3, 2] is a 6m telescope in the Atacama Desert of Chile, which operated at 148, 218, and 277 GHz using three 1024-element arrays of superconducting bolometers. The maps used in this analysis were made over three years of observation in the equatorial region during 2008–2010 at 148 GHz, and consist of six $3^\circ \times 18^\circ$ patches of sky at a noise level of ≈ 21 μK arcmin. In our source mask construction we also use maps of the same area made in 2008 at a frequency of 218 GHz. The maps were calibrated as in [29]. We apodize the maps by multiplying them with a mask that smoothly increases from zero to unity over 0.1° from the edge of the maps.

Although atmospheric noise is removed in the map-making process, we implement an additional filter in Fourier space to remove signal at multipoles below $\ell = 500$ (ℓ is the magnitude of the Fourier variable conjugate to sky angle). In addition, we remove a stripe for which $-100 < \ell_{\rm dec} < 100$ along the Fourier axis corresponding to declination to avoid contamination by scan noise. Furthermore, to increase the tSZ signal-to-noise, we apply a Wiener filter which downweights scales at which the tSZ signal is subdominant. This (non-optimal) filter is constructed by dividing the best-fit tSZ power spectrum from [13] by the total average power spectrum measured in the data maps, i.e. $C_\ell^{tSZ}/C_\ell^{tot}$. For multipoles above $\ell = 6 \times 10^3$, the tSZ signal is completely dominated by detector noise and point sources, and hence we remove all power above this multipole in the temperature maps. The final Fourier-space filter, shown in Fig. 1, is normalized such that its maximum value is unity. As it is constructed using the binned power spectrum of the data, it is not perfectly smooth; however, we apply the same filter consistently to data, simulations, and analytic theory, and thus any details of the filter do not bias the interpretation of our result.

After filtering, the edges of the maps are cut off to reduce any edge effects that might occur upon Fourier transforming despite apodization. Simulations verify that no additional skewness is introduced by edge effects into a trimmed map.

7.4.2 Removing Point Sources

In order to obtain a skewness signal due only to the tSZ effect, any contamination of the signal by point sources must be minimized. These objects consist of IR dusty galaxies and radio sources. We use two approaches to eliminate the point source contribution: template subtraction and masking using the 218 GHz channel.

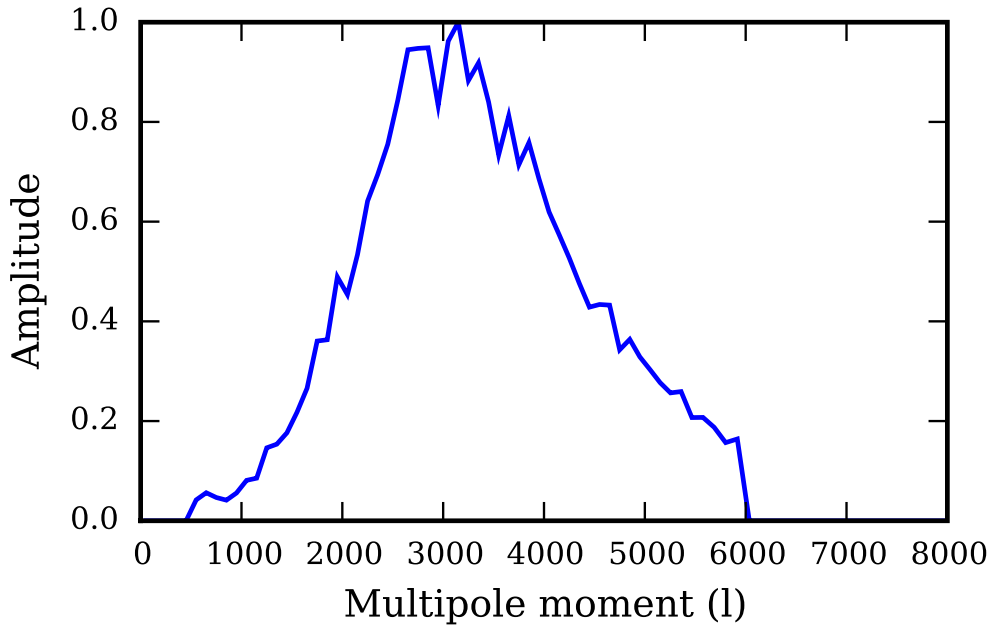

Figure 7.1: The Wiener filter applied to the ACT temperature maps before calculating the unnormalized skewness. This filter upweights scales on which the tSZ signal is large compared to other sources of anisotropy.

In the template subtraction method [30], which we use to remove resolved point sources (mainly bright radio sources), sources with a signal-to-noise (S/N) greater than five are first identified in a match-filtered map. A template with the shape of

the ACT beam is then scaled to the appropriate peak brightness of each source, and this profile is subtracted from the raw data. The process is iterated following the CLEAN algorithm [31] until no more sources can be identified. We verify that this procedure does not introduce skewness into the maps (e.g., through oversubtraction) by checking that similar results are obtained using a different procedure for reducing source contamination, in which we mask and in-paint pixels which contain bright sources with S/N > 5 [32].

We take a second step to suppress the lower-flux, unresolved point sources (mainly dusty galaxies) that remain undetected by the template subtraction algorithm. At 218 GHz, dusty galaxies are significantly brighter than at 148 GHz and the tSZ effect is negligible. We construct a dusty galaxy mask by setting all pixels (which are approximately 0.25 arcmin^2) to zero that have a temperature in the 218 GHz maps larger than a specified cutoff value. This cutoff is chosen to be 3.2 times the standard deviation of the pixel values in the filtered 148 GHz map (3.2σ). This procedure ensures regions with high flux from dusty galaxies are masked. We also set to zero all pixels for which the temperature is lower than the negative of this cutoff, so that the masking procedure does not introduce spurious skewness into the lensed CMB distribution, which is assumed to have zero intrinsic skewness. The mask is then applied to the 148 GHz map to reduce the point source contribution. Simulations ([33] for IR sources) verify that the masking procedure does not introduce spurious skewness into the 148 GHz maps.

Finally, all pixels more than twelve standard deviations (12σ) from the mean are also removed from the 148 GHz maps. Due to the ringing around very positive or negative pixels caused by the Wiener filter, the surrounding eight arcminutes of these points are also masked. This additional step slightly increases the S/N of the skewness measurement by reducing the dependence on large outliers, enhances the information content of low moments by truncating the tail of the pixel probability density function,

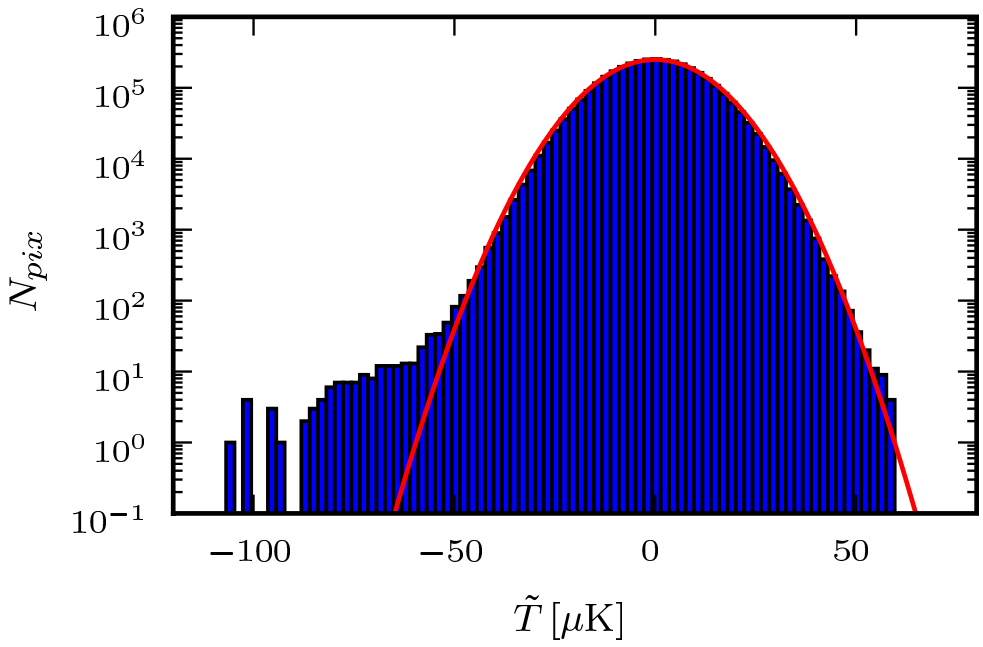

Figure 7.2: Histogram of the pixel temperature values in the filtered, masked ACT CMB temperature maps. A Gaussian curve is overlaid in red.

and ensures that any anomalous outlying points from possibly mis-subtracted bright radio sources do not contribute to the skewness signal. Overall, 14.5% of the 148 GHz map is removed by the masking procedure, though the removed points are random with respect to the tSZ field and should not change the signal.

7.5 Results

7.5.1 Evaluating the Skewness

We compute the unnormalized skewness of the filtered and processed 148 GHz maps by simply cubing and averaging the pixel values in real space. The result is $\langle \tilde{T}^3 \rangle = -31 \pm 6\ \mu\mathrm{K}^3$, a 5σ deviation from the null result expected for a signal without any non-Gaussian components. The skewness of the CMB temperature distribution in our filtered, processed maps is visible in the pixel value histogram shown in Fig. 2 (along

with a Gaussian curve overlaid for comparison). It is evident that the Gaussian CMB has been recovered on the positive side by point source masking, with the apparent truncation beyond 50 μK due to the minute probability of such temperatures in the Gaussian distribution. The likelihood corresponding to our measurement of the skewness is shown in Fig. 3.

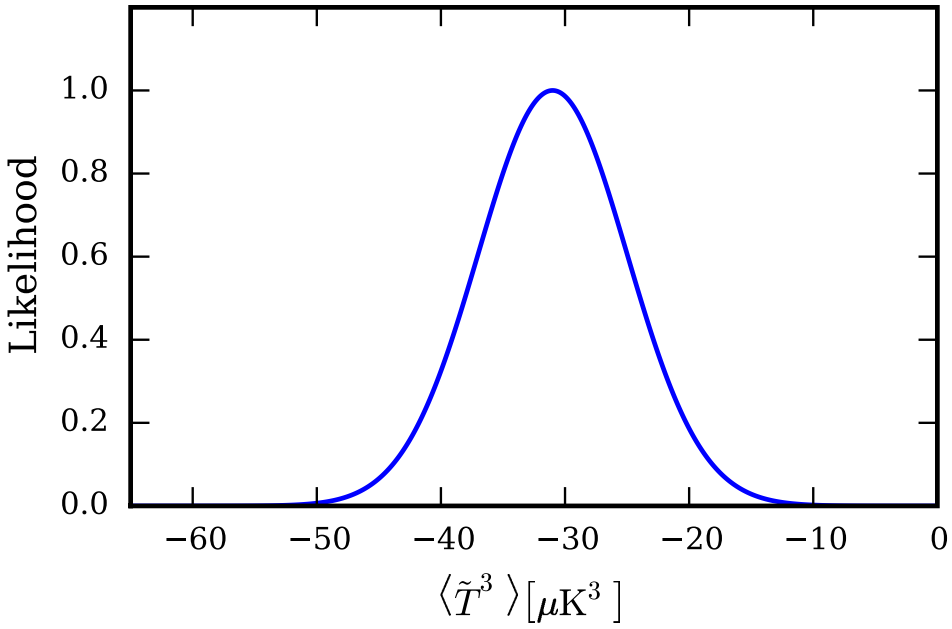

Figure 7.3: Likelihood of the skewness measurement described in the text (with Gaussian statistics assumed).

The "Gaussian statistics assumed" error on the skewness includes only Gaussian sources of noise. We calculate this error by using map simulations that consist of Gaussian random fields with the same power spectrum as that observed in the data, including beam effects. These simulations contain Gaussian contributions from IR, SZ, and radio sources, the primordial lensed CMB, and detector noise. This estimate thus does not include the error resulting from non-Gaussian corrections, which (after source subtraction) are due to the non-Gaussian tSZ signal. Though CMB lensing is also a non-Gaussian effect it does not contribute to the error on the skewness, as

the connected part of the six-point function is zero to lowest order in the lensing potential, and the connected part of the three-point function is also negligibly small (see [34] and references therein).

We calculate errors that include non-Gaussian corrections by constructing more realistic simulations. To construct such simulations, we add maps with simulated tSZ signal from [35], which assume $\sigma_8 = 0.8$, to realizations of a Gaussian random field which has a spectrum such that the power spectrum of the combined map matches that observed in the ACT temperature data. Given the simulated sky area, we obtain 39 statistically independent simulated maps, each of size 148 deg^2. By applying an identical procedure to the simulations as to the data, measuring the scatter amongst the patches, and appropriately scaling the error to match the 237 deg^2 of unmasked sky in the processed map, we obtain a full error (including non-Gaussian corrections) on the unnormalized skewness of 14 μK^3. While this error is a robust estimate it should be noted that the "error on the error" is not insignificant due to the moderate simulated volume available. The scatter of skewness values measured from each of the simulated maps is consistent with a Gaussian distribution. The estimate for the full error is coincidentally the same as the standard error, 14 μK^3, estimated from the six patches into which the data are divided. The full error is used below in deriving cosmological constraints from the skewness measurement.

7.5.2 The Origin of the Signal

Is the skewness dominated by massive clusters with large tSZ decrements – as suggested by theoretical considerations described earlier – or by more numerous, less massive clusters? To investigate this question, we mask clusters in our data which were found in the 148 GHz maps using a matched filter as in [36]. All clusters detected above a threshold significance value are masked; we vary this threshold and measure the remaining skewness in order to determine the origin of the signal.

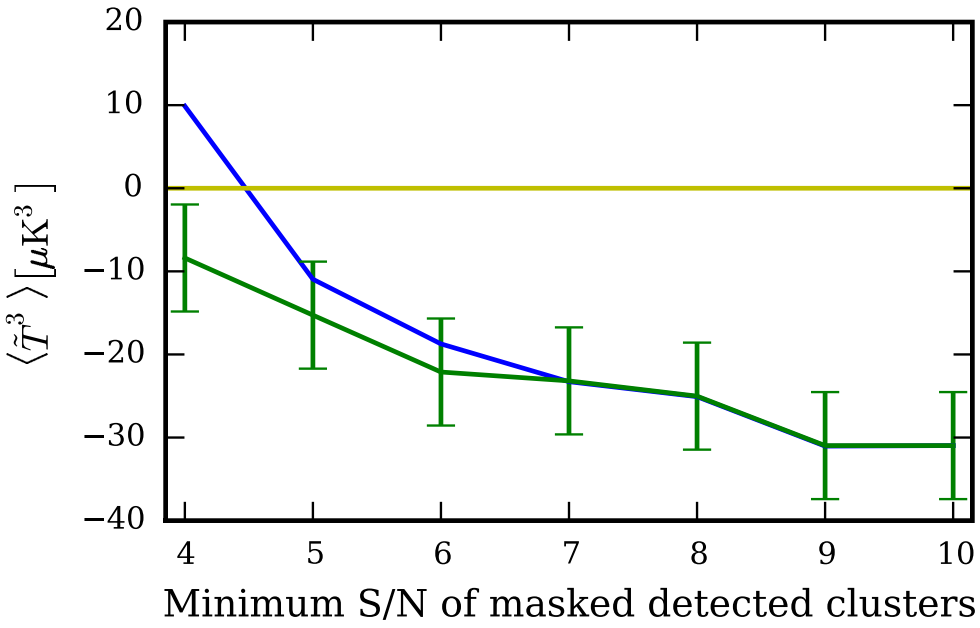

Figure 7.4: Plot of the skewness signal as a function of the minimum S/N of the clusters that are masked (this indicates how many known clusters are left in the data, unmasked). The blue line is calculated using the full cluster candidate catalog obtained via matched filtering, while the green line uses a catalog containing only optically-confirmed clusters [38]. Both lines have identical errors, but we only plot them for the green line for clarity. Confirmed clusters source approximately two-thirds of the signal, which provides strong evidence that it is due to the tSZ effect. Note that one expects a positive bias of $\approx 4\ \mu\mathrm{K}^3$ for the S/N = 4 point of the blue line due to impurities in the full candidate catalog masking the tail of the Gaussian distribution.

Fig. 4 shows a plot of the signal against the cluster detection significance cutoff. We include calculations using both the full cluster candidate catalog obtained via matched filtering as well a catalog containing only clusters confirmed optically using the methodology of [37] on the SDSS Stripe 82 [38]. The SDSS Stripe 82 imaging data cover $\approx 80\%$ of the total map area, and thus some skewness signal will necessarily arise from objects not accounted for in this catalog. The results for these two catalogs agree when masking clusters with S/N ≥ 7, but differ slightly when masking lower S/N clusters. This effect is likely due to the small shortfall in optical follow-up area

as well as a small number of false detections (i.e., impurity) in the candidate clusters that have not yet been optically followed up.

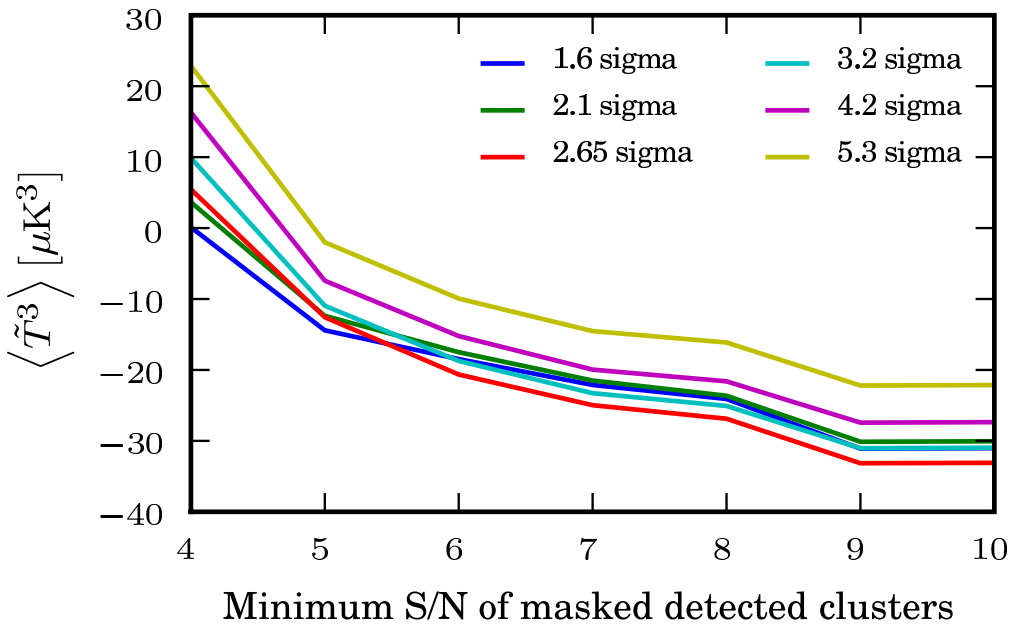

Figure 7.5: A test for IR source contamination: similar to the blue line in Fig. 4, but with a range of values of the cutoff used to construct an IR source mask in the 218 GHz band. Any cutoff below $\approx 3.2\sigma$ gives similarly negative results and thus appears sufficient for point source removal, where $\sigma = 10.3$ μK is the standard deviation of the 148 GHz maps. For comparison, the standard deviation of the 218 GHz maps is ≈ 2.2 times larger. The percentages of the map which are removed for the masking levels shown, from the least to the most strict cut, are 0.7, 2.5, 8.4, 14.5, 23.7, and 36.6%.

Using either catalog, Fig. 4 implies that just under half of the tSZ skewness is obtained from clusters that lie below a 5σ cluster detection significance, while the remainder comes from the brightest and most massive clusters. The results of [36] suggest that clusters detected at 5σ significance are roughly characterized by a mass $M_{500} = 5 \times 10^{14} M_{\odot}/h$, where M_{500} is the mass enclosed within a radius such that the mean enclosed density is 500 times the critical density at the cluster redshift. This value corresponds to a virial mass of roughly $M = 9 \times 10^{14} M_{\odot}/h$, which was

also found to be the mass detection threshold for high-significance ACT clusters in [37]. Fig. 4 thus demonstrates that roughly half of the tSZ skewness signal is due to massive clusters with $M \gtrsim 10^{15} M_{\odot}/h$. The theoretical calculations described earlier give similar results for the fraction of the signal coming from clusters above and below this mass scale, which is significantly higher than the characteristic mass scale responsible for the tSZ power spectrum signal.

Finally, the positive value in the full candidate catalog line shown in Fig. 4 when masking clusters above S/N = 4 is consistent with zero. When masking at this level (with the candidate catalog which contains some impurities), we slightly cut into the negative pixel values in the Gaussian component of Fig. 2, leading to a small spurious positive skewness. For the points we plot, we calculate that this bias is only non-negligible for the S/N = 4 cut, where it is $\approx 4\ \mu\mathrm{K}^3$. This bias effectively explains the small positive offset seen in Fig. 4. However, we discuss positive skewness due to any possible residual point source contamination below. Overall, the dependence of the measured skewness on cluster masking shown in Fig. 4 provides strong evidence that it is caused by the tSZ effect.

7.5.3 Testing for Systematic Infrared Source Contamination

Despite our efforts to remove point sources, a small residual point source contamination of the signal could remain, leading to an underestimate of the amplitude of the tSZ skewness. To investigate this systematic error source, we vary the level at which point sources are masked in the 218 GHz maps (the original level is 3.2 times the standard deviation of the pixel values in the filtered 148 GHz map (3.2σ), as described above). The results of this test are shown in Fig. 5, which uses the full catalog of cluster candidates as described in Fig. 4, since the optically-confirmed catalog does not yet cover the entire ACT map. Note that masking at 3.2σ results in a skewness measurement which agrees with its apparent asymptotic limit as the IR

contamination is reduced, within the expected fluctuations due to masking. While a slightly more negative skewness value can be measured for some masking levels stricter than the 3.2σ level chosen in the analysis, fluctuations upon changing the unmasked area of the sky are expected, so that it can not be rigorously inferred that IR contamination is reduced between 3.2σ and 2.65σ. Fig. 5 suggests that masking at the 3.2σ level sufficiently removes any contamination by IR sources, and stricter cuts will reduce the map area and increase statistical errors unnecessarily.

However, to further estimate the residual point source contamination in the 148 GHz maps, we process simulations of IR sources from [33] (with source amplitudes scaled down by 1.7 to match recent observations, as in [39]) with the same masking procedure as that applied to the data (described in §7.4.2), creating a mask in a simulated 218 GHz map, and applying it to a simulated IR source signal at 148 GHz. We find a residual signal of $\left\langle \tilde{T}^3 \right\rangle = 3.9 \pm 0.1\ \mu\mathrm{K}^3$. We treat this result as a bias in deriving cosmological constraints from the tSZ skewness in the following section.

We also investigate a linear combination of the 148 and 218 GHz maps that should have minimal IR source levels, namely, an appropriately scaled 218 GHz map subtracted from a 148 GHz map. Assuming that the spatial distribution of the point sources is not affected by the difference in observation frequency between 148 and 218 GHz and a single spectral index can be applied to all sources, a simple factor of ≈ 3.2 [13] relates a point source's signal in the two different frequency bands. We find that the appropriate linear combination (subtracting 1/3.2 times the 220 GHz map from the 148 GHz map) produces a signal in agreement with that resulting from the previously described masking procedure, although the additional noise present in the 218 GHz maps slightly reduces the significance of the detection.

7.6 Cosmological Interpretation

To obtain cosmological information from the measured amplitude of the unnormalized skewness, we compare our results with two different sets of tSZ simulations [33, 35]. Both sets of simulations are run with $\sigma_8 = 0.8$, but differ in their treatment of the ICM. The simulation of [35] is a fully hydrodynamic cosmological simulation that includes sub-grid prescriptions for feedback from active galactic nuclei, star formation, and radiative cooling. The simulation also captures non-thermal pressure support due to turbulence and other effects, which significantly alters the ICM pressure profile. The simulation of [33] is a large dark matter-only N-body simulation that is post-processed to include gas according to a polytropic prescription. This simulation also accounts for non-thermal pressure support (though with a smaller amount than [35]), and matches the low-redshift X-ray data presented in [17].

We perform the same filtering and masking as that applied to the data in order to analyze the simulation maps. For both simulations, the filtering reduces the signal by $\approx 95\%$ compared to the unfiltered value. For the simulations of [35], we measure $\left\langle \tilde{T}^3 \right\rangle^S = -37\ \mu\mathrm{K}^3$, with negligible errors (the superscript S indicates a simulated value). However, this value is complicated by the fact that these simulations only include halos below $z = 1$. An analytic estimate for the skewness contribution due to halos with $z > 1$ from Eq. (7.1) gives a 6% correction, which yields $\left\langle \tilde{T}^3 \right\rangle^S = -39\ \mu\mathrm{K}^3$. For the simulations of [33], we measure $\left\langle \tilde{T}^3 \right\rangle^S = -50\ \mu\mathrm{K}^3$, with errors also negligible for the purposes of cosmological constraints.

We combine these simulation results with our calculated scalings of the skewness and the sixth moment with σ_8 to construct a likelihood:

$$\mathcal{L}(\sigma_8) = \exp\left(-\frac{\left(\left\langle \tilde{T}^3 \right\rangle^D - \left\langle \tilde{T}^3 \right\rangle^{\mathrm{th}}(\sigma_8) \right)^2}{2\sigma^2_{\mathrm{th}}(\sigma_8)} \right) \tag{7.3}$$

where $\left\langle \tilde{T}^3 \right\rangle^D$ is our measured skewness value and the theoretically expected skewness as a function of σ_8 is given by

$$\left\langle \tilde{T}^3 \right\rangle^{\rm th}(\sigma_8) = \left\langle \tilde{T}^3 \right\rangle^S \left(\frac{\sigma_8}{0.8}\right)^{\alpha_3} . \tag{7.4}$$

The likelihood in Eq. (7.3) explicitly accounts for the fact that $\sigma^2_{\rm th}$, the variance of the skewness, depends on σ_8 — a larger value of σ_8 leads to a larger expected variance in the tSZ skewness signal. In particular, the variance of the tSZ skewness is described by a sixth moment, so it scales as $\sigma_8^{\alpha_6}$. As determined above, the Gaussian and non-Gaussian errors on the skewness are 6 μK^3 and $\sqrt{14^2 - 6^2}$ μK^3 = 12.6 μK^3, respectively. We approximate the dependence of the full error on σ_8 by assuming that only the non-Gaussian component scales with σ_8; while this is not exact, as some of the Gaussian error should also scale with σ_8, small differences in the size or scaling of the Gaussian error component cause negligible changes in our constraints on σ_8.

Finally, although we have argued previously that IR source contamination is essentially negligible, we explicitly correct for the residual bias as calculated in the previous section. Thus, we replace $\left\langle \tilde{T}^3 \right\rangle^D = -31$ μK^3 with $\left\langle \tilde{T}^3 \right\rangle^D_{corr} = -31 - 3.9$ μK^3 in Eq. (7.3). (Note that this bias correction only shifts the central value derived for σ_8 below by roughly one-fifth of the 1σ confidence interval.) Moreover, in order to be as conservative as possible, we also model the effect of residual point sources by including an additional IR contamination error (with the same value as the residual IR source contamination, 3.9 μK^3) in our expression for the variance of the skewness:

$$\sigma^2_{\rm th}(\sigma_8) = 6^2 \ \mu{\rm K}^6 + 12.6^2 \left(\frac{\sigma_8}{0.8}\right)^{\alpha_6} \ \mu{\rm K}^6 + 3.9^2 \ \mu{\rm K}^6. \tag{7.5}$$

Using the likelihood in Eq. (7.3), we obtain confidence intervals and derive a constraint on σ_8. Our likelihood and hence our constraints depend in principle on which simulation we use to calculate $\left\langle \tilde{T}^3 \right\rangle^S$, as well as on the values we choose for

α_3 and α_6. Using the simulations of [35] and the scalings determined above for the profile from [16], we find $\sigma_8 = 0.79^{+0.03}_{-0.03}$ (68% C.L.) $^{+0.06}_{-0.06}$ (95% C.L.). In Table I, we compare the constraints on σ_8 obtained from the use of different scalings and simulated skewness values; the constraints are insensitive to both the pressure profile used to derive the scaling laws and the choice of simulation used to compute the skewness.

For comparison, the final release from the *Chandra* Cluster Cosmology Project found $\sigma_8 = 0.803 \pm 0.0105$, assuming $\Omega_m = 0.25$ (there is a strong degeneracy between σ_8 and Ω_m for X-ray cluster measurements that probe the mass function) [40]. Perhaps more directly comparable, recent studies of the tSZ power spectrum have found $\sigma_8 = 0.77 \pm 0.04$ (statistical error only) [13] and $\sigma_8 = 0.807 \pm 0.016$ (statistical error and approximately estimated systematic error due to theoretical uncertainty) [41]. Our results are also comparable to recent constraints using number counts of SZ-detected clusters from ACT and SPT, which found $\sigma_8 = 0.851 \pm 0.115$ (fully marginalizing over uncertainties in the mass-SZ flux scaling relation) [42] and $\sigma_8 = 0.807 \pm 0.027$ (marginalizing over uncertainties in an X-ray-based mass-SZ flux scaling relation) [43], respectively. Although more than half of the tSZ skewness signal that we measure is sourced by detected clusters (i.e., the same objects used in the number counts analyses), our method also utilizes cosmological information from clusters that lie below the individual detection threshold, which gives it additional statistical power. Finally, note that we have fixed all other cosmological parameters in this analysis, as σ_8 is by far the dominant parameter for the tSZ skewness [44]. However, marginalizing over other parameters will slightly increase our errors.

To evaluate the theoretical systematic uncertainty in the amplitude of the filtered skewness due to unknown ICM astrophysics, we test the effect of different gas prescriptions by analyzing simulations from [35] with all forms of feedback, radiative cooling and star formation switched off, leading to an adiabatic ICM gas model. For

these adiabatic simulations we find $\left\langle \tilde{T}^3 \right\rangle^S = -56\ \mu\mathrm{K}^3$ (after applying the 6% correction mentioned earlier), which for the skewness we measure in our data would imply $\sigma_8 = 0.77^{+0.02}_{-0.02}$ (68% C.L.)$^{+0.05}_{-0.05}$ (95% C.L.). Turning off feedback and all subgrid physics is a rather extreme case, so the systematic theoretical uncertainty for a

	Battaglia $\left\langle \tilde{T}^3 \right\rangle^S$	Sehgal $\left\langle \tilde{T}^3 \right\rangle^S$
Battaglia α_3, α_6	$0.79^{+0.03\ +0.06}_{-0.03\ -0.06}$	$0.77^{+0.03\ +0.05}_{-0.02\ -0.05}$
Arnaud α_3, α_6	$0.79^{+0.03\ +0.06}_{-0.03\ -0.06}$	$0.77^{+0.02\ +0.05}_{-0.02\ -0.05}$
K-S α_3, α_6	$0.79^{+0.03\ +0.07}_{-0.03\ -0.06}$	$0.77^{+0.03\ +0.06}_{-0.03\ -0.05}$

Table 7.1: Constraints on σ_8 derived from our skewness measurement using two different simulations and three different scalings of the skewness and its variance with σ_8. The top row lists the simulations used to calculate the expected skewness for $\sigma_8 = 0.8$ [35, 33]; the left column lists the pressure profiles used to calculate the scaling of the skewness and its variance with σ_8 [16, 17, 25]. The errors on σ_8 shown are the 68% and 95% confidence levels.

typical simulation with some form of feedback should be slightly smaller than the statistical error from the measurement, though still non-negligible. This contrasts with measurements of σ_8 via the tSZ power spectrum, for which the theoretical systematic uncertainty is comparable to or greater than the statistical uncertainty [13, 41]. As highlighted earlier, this difference can be traced to the dependence of the power spectrum amplitude on the ICM astrophysics within low-mass, high-redshift clusters. The skewness, on the other hand, is dominated by more massive, lower-redshift clusters that are less affected by uncertain non-gravitational feedback mechanisms and are more precisely constrained by observations. Nonetheless, as the statistical uncertainty decreases on future measurements of the tSZ skewness, the theoretical systematic error will quickly become comparable, and thus additional study of the ICM electron pressure profile will be very useful.

7.7 Conclusions

As the thermal Sunyaev-Zel'dovich field is highly non-Gaussian, measurements of non-Gaussian signatures such as the skewness can provide cosmological constraints that are competitive with power spectrum measurements. We have presented a first measurement of the unnormalized skewness $\left\langle \tilde{T}^3(\hat{\mathbf{n}}) \right\rangle$ in ACT CMB maps filtered for high signal to noise. As this is a purely non-Gaussian signature, primordial CMB and instrumental noise cannot be confused with or bias the signal, unlike measurements of the tSZ power spectrum. We measure the skewness at 5σ significance: $\left\langle \tilde{T}^3(\hat{\mathbf{n}}) \right\rangle = -31 \pm 6\ \mu\mathrm{K}^3$ (Gaussian statistics assumed). Including non-Gaussian corrections increases the error to $\pm\ 14\ \mu\mathrm{K}^3$. Using analytic calculations and simulations to translate this measurement into constraints on cosmological parameters, we find $\sigma_8 = 0.79^{+0.03}_{-0.03}$ (68% C.L.) $^{+0.06}_{-0.06}$ (95% C.L.), with a slightly smaller but non-negligible systematic error due to theoretical uncertainty in the ICM astrophysics. This detection represents the first realization of a new, independent method to measure σ_8 based on the tSZ skewness, which has different systematic errors than several other common methods. With larger maps and lower noise, tSZ skewness measurements promise significantly tighter cosmological constraints in the near future.

7.8 Acknowledgements

As this manuscript was being prepared, we learned of related theoretical work by the authors of [44], and we acknowledge very helpful discussions with the members of this collaboration. This work was supported by the U.S. NSF through awards AST-0408698, PHY-0355328, AST-0707731 and PIRE-0507768, as well as by Princeton Univ., the Univ. of Pennsylvania, FONDAP, Basal, Centre AIUC, RCUK Fellowship (JD), NASA grant NNX08AH30G (SD, AH, TM), NSERC PGSD (ADH), NSF AST-0546035 and AST-0807790 (AK), NSF PFC grant PHY-0114422 (ES), KICP Fel-

lowship (ES), SLAC no. DE-AC3-76SF00515 (NS), ERC grant 259505 (JD), BCCP (SD), and the NSF GRFP (BDS, BLS). We thank B. Berger, R. Escribano, T. Evans, D. Faber, P. Gallardo, A. Gomez, M. Gordon, D. Holtz, M. McLaren, W. Page, R. Plimpton, D. Sanchez, O. Stryzak, M. Uehara, and Astro-Norte for assistance with ACT. ACT operates in the Parque Astronómico Atacama in northern Chile under the auspices of Programa de Astronomía, a program of the Comisión Nacional de Investigación Científica y Tecnológica de Chile (CONICYT).

References

[1] Fowler, J. W., Niemack, M. D., Dicker, S. R., et al. 2007, Applied Optics, 46, 3444

[2] Dunner, R., Hasselfield, M., Marriage, T. M., et al. in prep.

[3] Swetz, D. S., Ade, P. A. R., Amiri, M., et al. 2011, ApJS, 194, 41

[4] Carlstrom, J. E., Ade, P. A. R., Aird, K. A., et al. 2011, PASP, 123, 568

[5] Schaffer, K. K., Crawford, T. M., Aird, K. A., et al. 2011, ApJ, 743, 90

[6] Zel'dovich, Y. B., & Sunyaev, R. A. 1969, Ap&SS, 4, 301

[7] Sunyaev, R. A., & Zel'dovich, Y. B. 1970, Ap&SS, 7, 3

[8] Staniszewski, Z., Ade, P. A. R., Aird, K. A., et al. 2009, ApJ, 701, 32

[9] Vanderlinde, K., Crawford, T. M., de Haan, T., et al. 2010, ApJ, 722, 1180

[10] Hincks, A. D., Acquaviva, V., Ade, P. A. R., et al. 2010, ApJS, 191, 423

[11] Marriage, T. A., Acquaviva, V., Ade, P. A. R., et al. 2011, ApJ, 737, 61

[12] Sehgal, N., Trac, H., Acquaviva, V., et al. 2011, ApJ, 732, 44

[13] Dunkley, J., Hlozek, R., Sievers, J., et al. 2011, ApJ, 739, 52

[14] Keisler, R., Reichardt, C. L., Aird, K. A., et al. 2011, ApJ, 743, 28

[15] Rubiño-Martín, J. A., & Sunyaev, R. A. 2003, Mon. Not. R. Astron. Soc, 344, 1155

[16] Battaglia, N., Bond, J. R., Pfrommer, C., & Sievers, J. L. 2011, arXiv:1109.3711

[17] Arnaud, M., Pratt, G. W., Piffaretti, R., et al. 2010, A&A, 517, A92

[18] Shaw, L. D., Nagai, D., Bhattacharya, S., & Lau, E. T. 2010, ApJ, 725, 1452

[19] Battaglia, N., Bond, J. R., Pfrommer, C., & Sievers, J. L. 2011, arXiv:1109.3709

[20] Hajian, A., Viero, M. P., Addison, G., et al. 2012, ApJ, 744, 40

[21] Komatsu, E., Dunkley, J., Nolta, M. R., et al. 2009, ApJS, 180, 330

[22] Komatsu, E., & Kitayama, T. 1999, ApJ, 526, L1

[23] Tinker, J., Kravtsov, A. V., Klypin, A., et al. 2008, ApJ, 688, 709

[24] Sheth, R. K., & Tormen, G. 2002, Mon. Not. R. Astron. Soc, 329, 61

[25] Komatsu, E., & Seljak, U. 2002, Mon. Not. R. Astron. Soc, 336, 1256

[26] Hill, J. C., & Sherwin, B. D. 2012, arXiv:1205.5794

[27] Trac, H., Bode, P., & Ostriker, J. P. 2011, ApJ, 727, 94

[28] Holder, G. P., McCarthy, I. G., & Babul, A. 2007, Mon. Not. R. Astron. Soc, 382, 1697

[29] Hajian, A., Acquaviva, V., Ade, P. A. R., et al. 2011, ApJ, 740, 86

[30] Marriage, T. A., Baptiste Juin, J., Lin, Y.-T., et al. 2011, ApJ, 731, 100

[31] Högbom, J. A. 1974, A&AS, 15, 417

[32] Bucher, M., & Louis, T. 2011, arXiv:1109.0286

[33] Sehgal, N., Bode, P., Das, S., et al. 2010, ApJ, 709, 920

[34] Lewis, A., & Challinor, A. 2006, Physics Reports, 429, 1

[35] Battaglia, N., Bond, J. R., Pfrommer, C., Sievers, J. L., & Sijacki, D. 2010, ApJ, 725, 91

[36] Marriage, T. A., Acquaviva, V., Ade, P. A. R., et al. 2011, ApJ, 737, 61

[37] Menanteau, F., González, J., Juin, J.-B., et al. 2010, ApJ, 723, 1523

[38] Menanteau, F., et al. in prep.

[39] van Engelen, A., Keisler, R., Zahn, O., et al. 2012, arXiv:1202.0546

[40] Vikhlinin, A., Kravtsov, A. V., Burenin, R. A., et al. 2009, ApJ, 692, 1060

[41] Reichardt, C. L., Shaw, L., Zahn, O., et al. 2011, arXiv:1111.0932

[42] Sehgal, N., Trac, H., Acquaviva, V., et al. 2011, ApJ, 732, 44

[43] Reichardt, C. L., Stalder, B., Bleem, L. E., et al. 2012, arXiv:1203.5775

[44] Bhattacharya, S., Nagai, D., Shaw, L., Crawford, T., & Holder, G. P. 2012, arXiv:1203.6368

Appendix A

Lensing Simulation and Power Spectrum Estimation for High Resolution CMB Polarization Maps

A.1 Abstract

We present efficient algorithms for CMB lensing simulation and power spectrum estimation for flat-sky CMB polarization maps. We build a pure B-mode estimator to remedy E to B leakage due to partial sky coverage. We show that our estimators are unbiased, and consistent with the projected errors. We demonstrate our algorithm using simulated observations of small sky patches with realistic noise and weights for upcoming CMB polarization experiments.

A.2 Introduction

The recent measurements of the cosmic microwave background (CMB) power spectrum by the Atacama Cosmology Telescope [ACT, 11], South Pole Telescope [SPT, 24], and the *Planck* satellite [1] at small angular scales have provided important confirmation of the standard ΛCDM cosmological model, extending the measurements by the *WMAP* satellite [15, 3], and earlier observations. The next generation of CMB experiments are focused on measuring the polarization of the CMB. The anisotropies are only ∼10% polarized so an accurate measurement of the polarization power spectrum is challenging. A number of ground-based experiments are targeting this signal, with POLARBEAR [17], SPTpol [2], and ACTPol [20] designed to measure scales of a few arcminutes or less. These experiments aim to constrain the cosmological model by measuring the 'E-mode' power spectrum that provides an independent probe of the scalar modes measured through the temperature fluctuations, and by measuring the 'B-modes' generated due to the gravitational lensing of E-modes by the dark matter distribution along the line-of-sight. These lensing B-modes are generated at small scales, and are more easily accessible to high resolution ground-based telescopes than the larger scale primordial B-modes directly sourced by gravitational waves.

In this appendix we describe the estimation of E and B-mode power spectra from realistic observations of the CMB sky. The number of pixels for high resolution experiments is of order $\approx 10^7$, so a direct maximum likelihood method is computationally too expensive. Instead we rely on pseudo C_ℓ estimators [5]. One of the main challenges in estimating the pseudo B-mode power spectrum arises since the E and B mode decomposition of the polarization field on a incomplete sky induces leakage between the two modes. The discontinuity at the edges of the map mixes E and B modes, increasing the variance of the B-mode power spectrum. Smith [22] and Smith & Zaldarriaga [23] provide a general solution to this problem by defining a pure B-mode power spectrum estimator that is not contaminated by this mixing.

In Section 2, we adapt their algorithm for flat sky maps, and demonstrate that the algebra simplifies considerably under the flat-sky approximation.

In Section 3, we introduce a novel technique for generating high resolution lensed CMB maps. Different methods have been proposed to do this, often using a remapping between pixels [18] and an interpolation scheme. We present a hybrid method that combines pixel remapping and a Taylor series decomposition of the lensed field. In Section 4, we use simulated observations from the ACTPol experiment to generate non-uniform realizations of the experimental noise. We then test our lensing simulation and power spectrum estimation method, and its optimality, using Monte Carlo simulations.

A.3 E/B leakage in the flat sky approximation

In this section we review the issue of leakage of power between polarization types due to incomplete sky coverage. This issue has been discussed in previous studies targeting observations over large areas [e.g., 19, 22, 23, 13, 9, 25, 8, 7, 14]. We demonstrate how the 'pure' estimators of the different polarization types can be applied in the flat-sky approximation, relevant to small patches of the sky.

A.3.1 Notation

For linear polarization, the Stokes parameter Q quantifies the polarization in the x-y direction and U quantifies it along axes rotated by 45°. Following e.g., [6], the polarization tensor is given by

$$P_{ab}(\vec{x}) = \frac{1}{2}\begin{pmatrix} Q(\vec{x}) & U(\vec{x}) \\ U(\vec{x}) & -Q(\vec{x}) \end{pmatrix}. \tag{A.1}$$

Any 2×2 symmetric traceless tensor can be uniquely decomposed into two parts of the form $\mathcal{E}_{ab}A = (-\partial_a\partial_b + \frac{1}{2}\delta_{ab}\nabla^2)A$ and $\mathcal{B}_{ab}B = \frac{1}{2}(\epsilon_{ac}\partial^c\partial_b + \epsilon_{bc}\partial^c\partial_a)B$ where A and B are scalar functions [e.g., 16]. The Fourier modes $e^{i\vec{\ell}\vec{x}}$ provide a basis for a scalar function in the plane, so one can define

$$\begin{aligned} ({}^{E}e^{i\vec{\ell}.\vec{x}})_{ab} &= N_{\vec{\ell}}\mathcal{E}_{ab}(e^{i\vec{\ell}\vec{x}}) = N_{\vec{\ell}}\left(\ell_a\ell_b - \frac{\vec{\ell}^2}{2}\delta_{ab}\right)e^{i\vec{\ell}\vec{x}} \\ ({}^{B}e^{i\vec{\ell}.\vec{x}})_{ab} &= M_{\vec{\ell}}\mathcal{B}_{ab}(e^{i\vec{\ell}\vec{x}}) = -\frac{M_{\vec{\ell}}}{2}\left(\epsilon_{ac}\ell^c\ell_b + \epsilon_{bc}\ell^c\ell_a\right)e^{i\vec{\ell}\vec{x}}, \end{aligned} \tag{A.2}$$

where N and M are normalization coefficients that satisfy the orthogonality relation

$$\int d^2x({}^{E}e^{i\vec{\ell}\vec{x}})^*_{ab}({}^{E}e^{i\vec{\ell}'\vec{x}})^{ab} = \delta(\vec{\ell} - \vec{\ell}'), \tag{A.3}$$

and similarly for ${}^{B}e^{i\vec{\ell}\vec{x}}$. Expanding the polarization field in this basis, it can be expressed as a combination of parity even (E) and odd (B) modes

$$\begin{aligned} P_{ab}(\vec{x}) &= \frac{1}{\sqrt{2}}\int d\vec{\ell}E(\vec{\ell})({}^{E}e^{i\vec{\ell}\vec{x}})_{ab} + B(\vec{\ell})({}^{B}e^{i\vec{\ell}\vec{x}})_{ab}, \\ E(\vec{\ell}) &= \frac{2}{\ell^2}\int d^2xP_{ab}(\vec{x})\mathcal{E}^{ab}(e^{-i\vec{\ell}\vec{x}}), \\ B(\vec{\ell}) &= \frac{2}{\ell^2}\int d^2xP_{ab}(\vec{x})\mathcal{B}^{ab}(e^{-i\vec{\ell}\vec{x}}). \end{aligned} \tag{A.4}$$

This is equivalent to the spin formalism introduced by Seljak & Zaldarriaga [21]. Defining ϕ_ℓ as the angle between the vector $\vec{\ell}$ and the ℓ_x axis, E and B take the simple form

$$\begin{aligned} E(\vec{\ell}) &= Q(\vec{\ell})\cos 2\phi_\ell + U(\vec{\ell})\sin 2\phi_\ell, \\ B(\vec{\ell}) &= -Q(\vec{\ell})\sin 2\phi_\ell + U(\vec{\ell})\cos 2\phi_\ell \end{aligned} \tag{A.5}$$

or equivalently $E(\vec{\ell}) \pm iB(\vec{\ell}) = e^{\mp 2i\phi_\ell}(Q(\vec{\ell}) \pm iU(\vec{\ell}))$.

A.3.2 Partial sky coverage

Observations with modern high resolution experiments are typically performed on a small fraction of the sky, of area Ω [e.g., 24, 11]. The observed region can be described by a window function

$$W(\vec{x}) = \begin{cases} w(\vec{x}) & \text{if } \vec{x} \in \Omega \\ 0 & \text{otherwise} \end{cases} \tag{A.6}$$

which modifies the observed Q and U components such that $\tilde{Q}(\vec{x}) = W(\vec{x})Q(\vec{x})$ and $\tilde{U}(\vec{x}) = W(\vec{x})U(\vec{x})$. Propagating the effects of the window function into the $\tilde{E}$ and $\tilde{B}$ modes calculated as in Eqn. A.5, the window functions mix E and B modes to give the modified modes

$$\begin{aligned} \tilde{E}(\vec{\ell}) &= \int d\vec{\ell'} W(\vec{\ell} - \vec{\ell'})[E(\vec{\ell'}) \cos 2(\phi_{\ell'} - \phi_\ell) - B(\vec{\ell'}) \sin 2(\phi_{\ell'} - \phi_\ell)], \\ \tilde{B}(\vec{\ell}) &= \int d\vec{\ell'} W(\vec{\ell} - \vec{\ell'})[E(\vec{\ell'}) \sin 2(\phi_{\ell'} - \phi_\ell) + B(\vec{\ell'}) \cos 2(\phi_{\ell'} - \phi_\ell)]. \end{aligned} \tag{A.7}$$

The power spectra of these modified modes are then

$$\begin{aligned} \langle \tilde{E}(\vec{\ell}) \tilde{E}^*(\vec{\ell}) \rangle &= \int d\vec{\ell'} |W(\vec{\ell} - \vec{\ell'})|^2 [C_{EE}(\ell') \cos^2 2(\phi_{\ell'} - \phi_\ell) + C_{BB}(\ell') \sin^2 2(\phi_{\ell'} - \phi_\ell)], \\ \langle \tilde{B}(\vec{\ell}) \tilde{B}^*(\vec{\ell}) \rangle &= \int d\vec{\ell'} |W(\vec{\ell} - \vec{\ell'})|^2 [C_{EE}(\ell') \sin^2 2(\phi_{\ell'} - \phi_\ell) + C_{BB}(\ell') \cos^2 2(\phi_{\ell'} - \phi_\ell)]. \end{aligned} \tag{A.8}$$

Since C_{EE} is expected to be an order of magnitude larger than C_{BB}, this mixing therefore leads to significant contamination of the B-modes by the leaked-in E-modes. This is illustrated in Figure A.1, which also highlights that the leakage is localized close to the edges of the map, or to the edges of holes due to masking of bright point

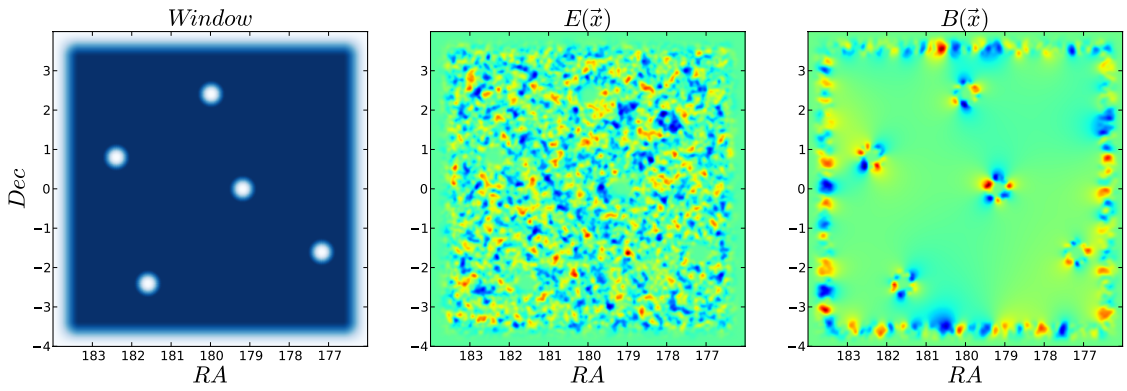

Figure A.1: Effect of sky cuts on the polarization pattern. A pure E-mode signal on the sky is observed through a window with a point source mask (left) leading to the estimated E-mode (centre) and B-mode (right) maps. The leaked E-modes show up as spurious signal in the B-mode map localized around the discontinuities of the window function.

sources. This leakage will increase the variance of the measured C_{BB}, even when an unbiased estimator is constructed for C_{BB} and C_{EE} by inverting the convolutions.

A.3.3 Pure estimators

A solution to the problem of E/B mixing has been proposed by Smith [22], Smith & Zaldarriaga [23]. Rather than deconvolving $E(\ell)$ and $B(\ell)$, the window function can be included directly in the projection operator (Eqn. A.4), such that

$$E^{pure}(\vec{\ell}) = \frac{2}{\ell^2}\int d^2x P^{ab}(\vec{x})\mathcal{E}_{ab}(W(\vec{x})e^{-i\vec{\ell}\vec{x}}) \quad (A.9)$$

$$B^{pure}(\vec{\ell}) = \frac{2}{\ell^2}\int d^2x P^{ab}(\vec{x})\mathcal{B}_{ab}(W(\vec{x})e^{-i\vec{\ell}\vec{x}}). \quad (A.10)$$

Using this method, any ambiguous modes are projected out and pure E and B modes are recovered. The window function and its first derivative must be zero at the edges of the map to avoid generating spurious B modes.

Here we show how this method can be simply applied in the flat sky approximation. By applying the product rule to the differential projection operators on the right hand

sides of the above equations, we obtain expressions for the pure E and B modes. The $B^{pure}(\vec{\ell})$ mode is given by

$$\begin{aligned} B^{pure}(\vec{\ell}) &= \frac{2}{\ell^2}\int d^2x W(\vec{x})P^{ab}(\vec{x})\mathcal{B}_{ab}(e^{-i\vec{\ell}\vec{x}}) + \frac{1}{\ell^2}\int d^2x \left[2Q\partial_x\partial_y W + U(\partial_y^2-\partial_x^2)W\right] e^{-i\vec{\ell}\vec{x}} \\ &- \frac{2i}{\ell}\int d^2x \left[Q(\vec{x})(\partial_y W\cos\phi_\ell + \partial_x W\sin\phi_\ell) + U(\vec{x})(\partial_y W\sin\phi_\ell - \partial_x W\cos\phi_\ell)\right] e^{-i\vec{\ell}\vec{x}}. \end{aligned} \tag{A.11}$$

The first term is the standard "naive" B mode estimator and the second and third terms cancel the window-induced leakage from E to B modes, involving derivatives of the window function. This expression is convenient for numerical uses as it does not require the calculation of derivatives of noisy data. The pure estimator removes the E/B leakage, but the remaining mode coupling effect induced by applying a window to the observed sky still needs to be deconvolved.

To work out this effect, we can simplify the algebra if we express the pure estimator in term of the χ variables [e.g., 19], with

$$\begin{aligned} \chi_E(\vec{x}) &= -\frac{1}{2}\left[\bar{\eth}\bar{\eth}(Q+iU)(\vec{x}) + \eth\eth(Q-iU)(\vec{x})\right], \\ \chi_B(\vec{x}) &= \frac{i}{2}\left[\bar{\eth}\bar{\eth}(Q+iU)(\vec{x}) - \eth\eth(Q-iU)(\vec{x})\right], \end{aligned} \tag{A.12}$$

where the spin raising and spin lowering operators are defined as $\eth = -(\partial_x + i\partial_y)$, and $\bar{\eth} = -(\partial_x - i\partial_y)$. After some algebra we find simple expressions for the two pure modes,[1]

$$\begin{aligned} B^{pure}(\vec{\ell}) &= \frac{1}{\ell^2}\int d\vec{x}\chi_B(\vec{x})W(\vec{x})e^{-i\vec{\ell}\vec{x}}, \\ E^{pure}(\vec{\ell}) &= \frac{1}{\ell^2}\int d\vec{x}\chi_E(\vec{x})W(\vec{x})e^{-i\vec{\ell}\vec{x}}. \end{aligned} \tag{A.13}$$

[1]This is most directly verified by inserting the definition of $\chi_{B/E}$ into the above integrals and integrating by parts twice; the result obtained is identical to the original form of the pure estimators.

The simple expressions for the pure estimators using the χ variables are convenient for computing this mode-to-mode coupling. Noting that

$$\begin{aligned}\chi_E(\vec{x}) &= \int d\vec{\ell} E(\vec{\ell}) \ell^2 e^{i\vec{\ell}\vec{x}}, \\ \chi_B(\vec{x}) &= \int d\vec{\ell} B(\vec{\ell}) \ell^2 e^{i\vec{\ell}\vec{x}},\end{aligned} \tag{A.14}$$

we find that the coupling between modes is

$$\begin{aligned}\langle B^{pure}(\vec{\ell}) B^{*pure}(\vec{\ell}) \rangle &= \frac{1}{\ell^4} \left\langle \int d\vec{x} \chi_B(\vec{x}) W(\vec{x}) e^{-i\vec{\ell}\vec{x}} \int d\vec{x'} \chi_B(\vec{x'}) W(\vec{x'}) e^{i\vec{\ell}\vec{x'}} \right\rangle, \\ &= \frac{1}{\ell^4} \int d\vec{\ell'} |W(\vec{\ell} - \vec{\ell'})|^2 \ell'^4 C_{BB}(\vec{\ell'})\end{aligned} \tag{A.15}$$

for the B-modes, and

$$\langle E^{pure}(\vec{\ell}) E^{*pure}(\vec{\ell}) \rangle = \frac{1}{\ell^4} \int d\vec{\ell'} |W(\vec{\ell} - \vec{\ell'})|^2 \ell'^4 C_{EE}(\vec{\ell'}) \tag{A.16}$$

for the E-modes. Here we have used $\langle \chi_B(\vec{\ell'}) \chi_B^*(\vec{\ell''}) \rangle = \delta(\vec{\ell'} - \vec{\ell''}) \ell'^4 C_{BB}(\vec{\ell'})$. In practice using the pure E mode power spectrum estimator is unnecessary since the B-to-E leakage is small so the advantage of using a pure estimator is lost and results in a loss of sensitivity. We choose to use a hybrid approach [14], where the B mode power spectrum is computed using the pure formalism (Eqn. A.11) and the E modes power spectrum is computed via the standard pseudo power spectrum formalism.

A.4 Generating gravitationally lensed simulations

On their way from the surface of last scattering, the photons are deflected by the gravitational field of the intervening large scale structure. Accurate lensing simulations are essential for recovering the statistical property of the observed CMB. In the weak field limit, the lensing results in a simple remapping of the temperature by a

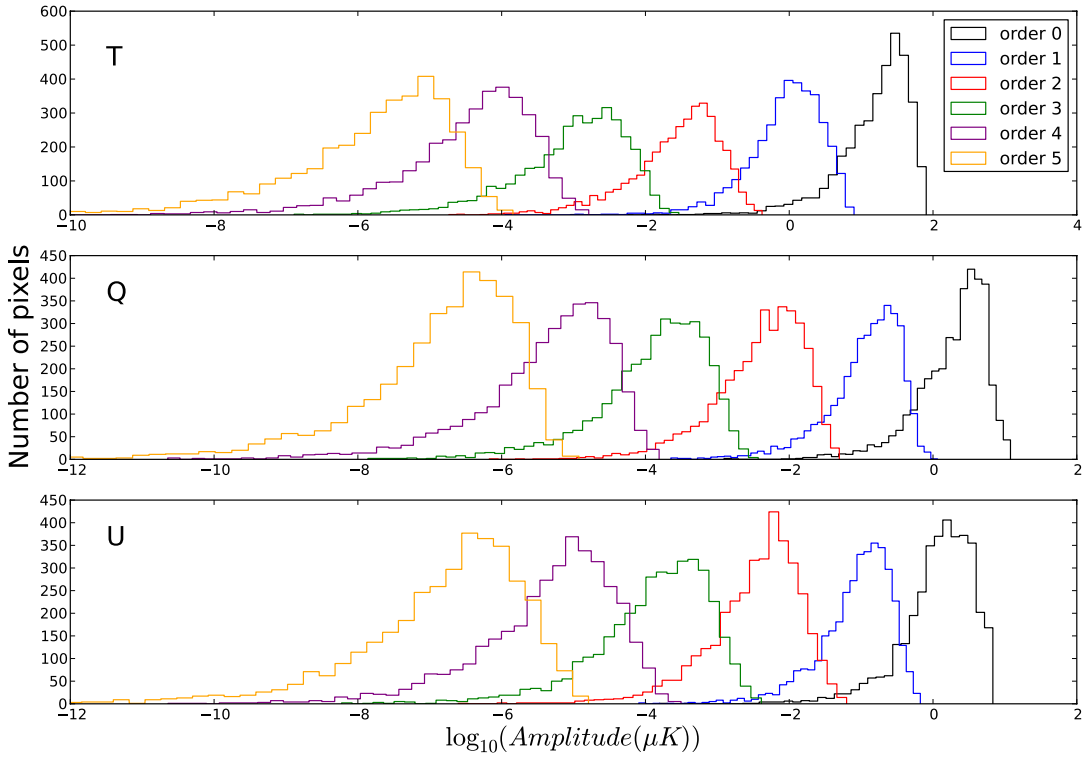

Figure A.2: Convergence of the Taylor series in pixel space. We represent the contribution of each higher order term of the Taylor series by showing the histogram of its pixel distribution. The convergence of the series is fast, each term being ≈ 60 times smaller than the preceding one. The contribution of the third order term is of order $10^{-1}\mu$K for T and $10^{-2}\mu$K for Q and U.

deflection angle $\vec{\alpha} = \nabla\phi$, where ϕ is the lensing potential, a line of sight integral over the matter distribution. The same applies to the polarisation field:

$$\begin{aligned} \tilde{T}(\vec{x}) &= T(\vec{x} + \nabla\phi) \\ \tilde{P}_{ab}(\vec{x}) &= P_{ab}(\vec{x} + \nabla\phi). \end{aligned} \tag{A.17}$$

This conceptually simple remapping is complicated by the fact that we cannot work directly with the continuous real-space map, only with discrete pixelizations of it. Three main approaches have been suggested for implementing this remapping in simulations [18]:

1. **Go directly from frequency domain to the lensed positions**, i.e. $T(\vec{x}+\vec{\alpha}) = \sum_{\vec{\ell}} \mathcal{F}^{-1}_{\vec{\ell}}(\vec{x}+\vec{\alpha}) T_{\vec{\ell}}$, where $\mathcal{F}^{-1}_{\vec{\ell}}(\vec{x})$ is the inverse Fourier transform operator, and $T_{\vec{\ell}}$ are the harmonic coefficients of the unlensed map. This approach is exact, but computationally inefficient because the shifted positions will not in general form a regular grid, and one hence cannot use Fast Fourier Transforms (FFT).

2. **Taylor expand the field**: This is straightforward, but has been found to converge slowly at small scales.

3. **Pixel remapping**: Truncate the displacement to the nearest pixel, and read off the corresponding pixel value. This remapping must be done at much higher resolution than the physical scales of interest in the map in order to avoid pixelization errors, and hence comes at a large cost both in terms of CPU-time and memory. It is therefore sometimes combined with pixel-space interpolation schemes.

We present a simple modification to the Taylor expansion method that addresses its slow convergence. In general, the Taylor expansion of a function $f(x)$ around a point x_0 becomes less accurate as the distance from x_0 grows, and conversely, the expansion can be truncated earlier if one can expand around a point close to where one wishes to evaluate the function. The Taylor remapping method above expands $T(\vec{x}+\vec{\alpha})$ around the point $\vec{\alpha} = 0$, and the reason for the slow convergence is that $\vec{\alpha}$ can be relatively large. A better choice is to expand around the pixel center $\vec{\alpha}_0$ closest to $\vec{\alpha}$, which is already exactly available, resulting in the following expansion

$$\begin{aligned} \tilde{T}(\vec{x}) = T(\vec{x}+\vec{\alpha}_0+\vec{\Delta\alpha}) &= T(\vec{x}+\vec{\alpha}_0) + \Delta\alpha^c [\partial_c T](\vec{x}+\vec{\alpha}_0) \\ &+ \frac{1}{2}\Delta\alpha^c \Delta\alpha^d [\partial_c \partial_d T](\vec{x}+\vec{\alpha}_0) + ... \end{aligned} \tag{A.18}$$

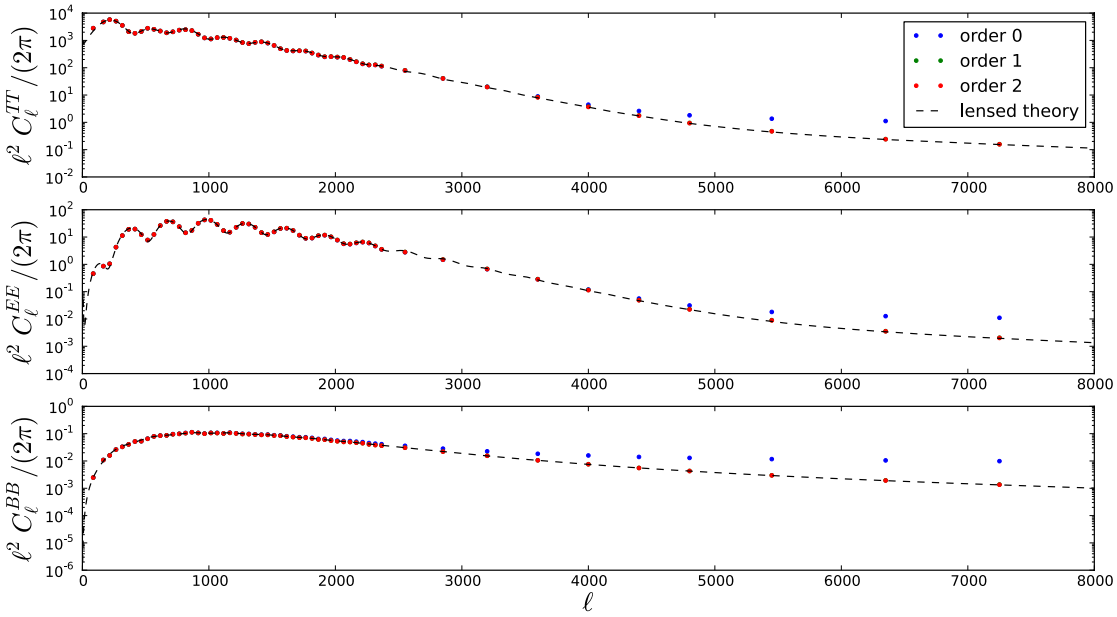

Figure A.3: Convergence of the Taylor series: power spectra. We compute the temperature (TT) and polarization (EE, BB) power spectra of the series truncated at different orders. Convergence is achieved by second order in the expansion.

The derivatives can be computed in Fourier space

$$\tilde{T}(\vec{x}) \;=\; T(\vec{x}+\vec{\alpha}_0) + \sum_{n=1}^{\infty} \frac{i^n}{n!} \left[\int (\Delta\alpha^x \ell_x + \Delta\alpha^y \ell_y)^n T(\vec{\ell}) e^{i\vec{\ell}\vec{x}} d\vec{\ell} \right]_{\vec{x}+\vec{\alpha}_0} \tag{A.19}$$

In practice we truncate the expansion at order N

$$\tilde{T}_N(\vec{x}) \;=\; \sum_{n=0}^{N} \sum_{k\leq n} \frac{(\Delta\alpha^x)^{n-k}(\Delta\alpha^y)^k}{k!(n-k)!} \mathcal{F}^{-1}(i^n \ell_x^{n-k} \ell_y^k \mathcal{F}T)(\vec{x}+\vec{\alpha}_0). \tag{A.20}$$

Here we use the FFT to compute each of the derivatives. Expanding around $\vec{\alpha}_0$ ensures that the Taylor expansion will at most need to extrapolate by half a pixel in any direction, which ensures that all scales present in the input map will converge rapidly. This is effectively a hybrid between the pixel remapping and Taylor expansion methods, but unlike normal pixel remapping one does not need to work at higher resolution than the map that is being lensed. Each term in this expansion can be

computed at the cost of $(n+1)$ FFT. When expanding around $\vec{\alpha}_0$, we find that the series converges rapidly. In Figure A.2 we show the pixel histograms of a part of the maps for each of the first 6 terms in the expansion. We find that the contribution falls by a factor of ~ 60 for each order for a $13^\circ \times 13^\circ$ lensed noiseless CMB simulation with 0.5' pixel size.

We also computed the bias for each order using 60 such simulations, shown in Figure A.3, and found that truncating the series at second order is an excellent approximation for any realistic CMB experiment. For comparison, the old method of expanding around $\vec{\alpha} = 0$ requires more than 20 orders to converge at this resolution, which given the quadratic scaling of the method corresponds to a performance difference of a factor of ~ 50. Using this method, lensing a $13^\circ \times 13^\circ$ patch of the sky at 0.5' resolution takes only a few seconds on one processor, and only requires a few times the memory that a single map takes up. While the method is formulated in the context of the flat sky in this case, it also generalizes trivially to the full, curved sky.

A.5 Implementation on realistic observations

High resolution ground-based experiments are observing small patches of the sky, measuring both the temperature and polarization of the CMB. There are also a set of lower resolution experiments underway targeting larger regions of sky in order to constrain or measure gravitational waves, but these will require analysis on the curved sky. In this section we test our power spectrum estimation method on simulated data, using a specific example of a subset of observations expected from the ACTPol experiment where the flat-sky approximation is appropriate.

Here we assume that 4 patches of the sky, for a total area of ~ 300 deg^2, are observed to a noise level of 5.7 μK/arcmin in temperature. The expected coverage of a patch is non-uniform due to the scanning strategy of the telescope; the expected

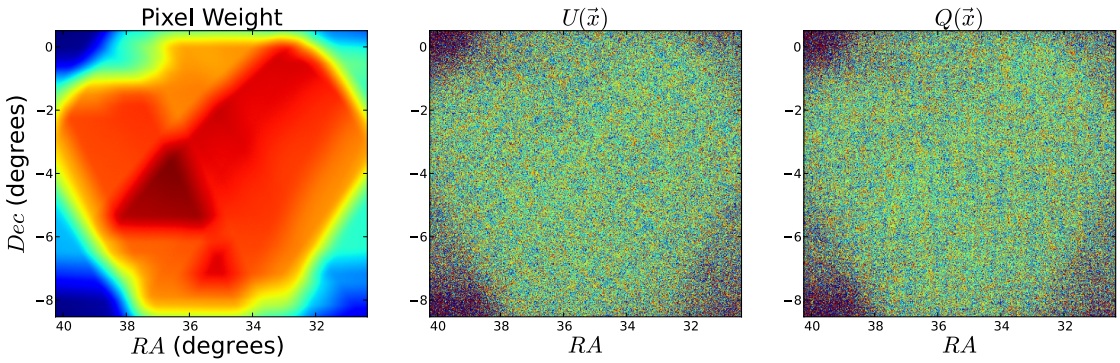

Figure A.4: Realization of the noise, for a U and Q map (centre and right) generated using a simulated pixel weight map (left). This represents the number of observations per pixel for an inhomogeneous survey, and is taken from a simulation for the ACTPol experiment.

statistical weight associated with each pixel is shown in the left panel of Figure A.4 for one of the patches. ACTPol will also target a larger region of the sky. For comparison, the PolarBear experiment is targeting three 225 deg^2 regions at 6 μK/arcmin sensitivity in temperature [17], and SPTPol have initially targeted a 100 deg^2 region, with the goal to cover 625 deg^2 to 5 μK/arcmin [2].

A.5.1 Estimated power spectra

We simulate data for each patch of sky in four subsets, generating independent maps of identical coverage and equal depth as in Das et al. [12, 11]. We refer to each subset as a 'split'. We convolve the simulation with a spherically symmetric gaussian beam with FWHM of 1′, and we simulate an inhomogeneous noise realization by convolving the weight map for each patch with a 5.7 μK/arcmin noise realization. We 'prewhiten' the temperature maps as defined in Das, Hajian & Spergel [10]. Here, the maps are convolved in real space with kernels designed to make the power spectrum as flat as possible, to reduce aliasing of power due to the point source mask. We then apply a 5' (apodized with a 0.3° cosine kernel) point source mask to account for the possible contamination from polarized extragalactic point sources.

We compute the binned cross-power spectrum $C_b^{iX\times jY}$ between maps i and j, for polarization types X and Y, using the pure estimators for B (Eqn. A.11) and a standard Fourier transform for T and E as discussed in section 2. The estimated spectrum is then given by

$$\widetilde{C}_b^{iX\times jY} = \sum_{b'} M_{bb'}^{XY} C_{b'}^{iX\times jY}, \tag{A.21}$$

where the mode coupling matrix is

$$M_{bb'}^{XY} = \sum_{\vec{\ell},\vec{\ell}'} P_{b\vec{\ell}} |W^{XY}(\vec{\ell}-\vec{\ell}')|^2 \left(\frac{\ell'}{\ell}\right)^{\beta_{XY}} (F_{\ell'}^{XY})^2 Q_{\vec{\ell}'b'}. \tag{A.22}$$

Here $\beta_{XY} = 2[\delta_{BX} + \delta_{BY}]$, i.e., for the pure-mode BB spectrum $\beta = 4$, but $\beta = 0$ for TT and EE. The window function $W^{XY}(\vec{\ell})$ is a product of the point source mask, the $n_{\rm obs}$ weight map, and a 0.7° cosine apodization at the edges (Smith & Zaldarriaga [23]), with a geometrical correction for the E modes (Eqn. A.7). The function F_ℓ^{XY} is the product of the beam, a pixel window function and the transfer function of the prewhitener for the temperature power spectrum. Here $P_{b\vec{\ell}}$ is a binning matrix, and $Q_{\vec{\ell}b}$ is an interpolation matrix, the binning being defined as a set of annuli in the 2 dimensional power spectrum space. Here we choose a minimal bin size of $\Delta\ell = 100$. Each of the mode coupling matrices is computed exactly and inverted in order to recover an unbiased spectrum.

We compute the spectra for 720 realizations of the noise and CMB, each with a different realization of the gravitational lensing potential. The cosmological model we use is the best-fitting ΛCDM model with no tensor contribution, so the B-mode signal comes only from gravitational lensing. The mean recovered spectra for TT, EE, BB, and the cross-correlation spectra are shown in Figure A.5, together with the estimated 1σ error bar for a single realization derived from the scatter of the simulations. The

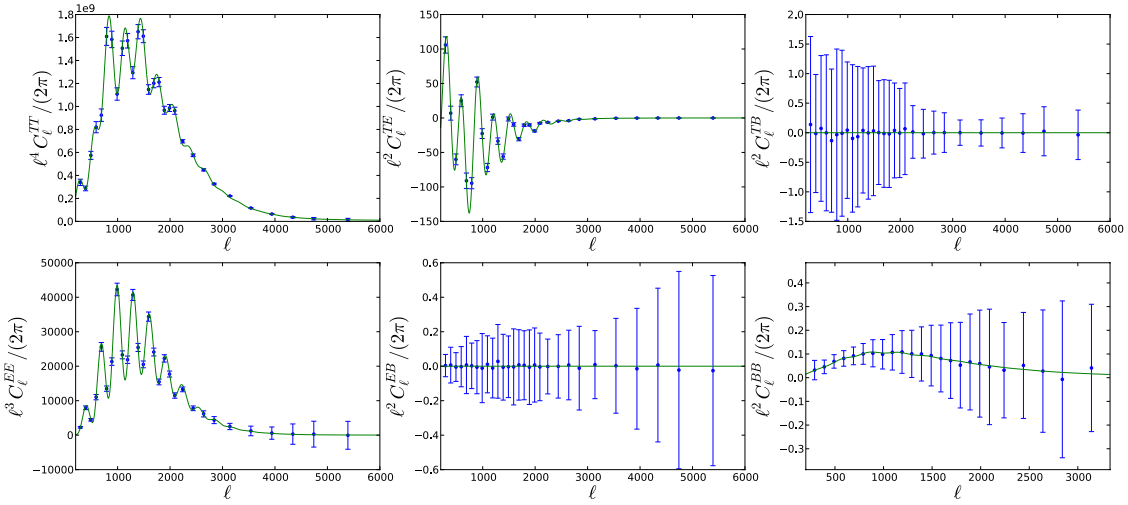

Figure A.5: Power spectra estimated from temperature and polarization maps. This shows the average binned spectra estimated from 720 Monte Carlo simulations, with errors estimated from the 1σ dispersion. The B-mode spectra are derived using the pure estimator, to avoid leakage from the E-mode spectrum.

recovered power spectra are consistent with the input power spectra at the 0.1 σ level in the interval $500 < \ell < 6000$.

A.5.2 Power spectrum uncertainties

Using the Monte Carlo simulations, we can compare the errors derived from the internal scatter, with an analytic estimate. This provides a measure of the optimality of this method. The analytic covariance in a single bin assuming no leakage is given by

$$\begin{aligned}\Theta_{bb}^{(X\times Y);(W\times Z)} &= \frac{1}{\nu_b}\left(C_b^{X\times W}C_b^{Y\times Z}+C_b^{X\times Z}C_b^{Y\times W}\right)\\ &+ \frac{1}{\nu_b n_d}\left(C_b^{X\times W}N_b^{Y\times Z}+C_b^{Y\times Z}N_b^{X\times W}+C_b^{X\times Z}N_b^{Y\times W}+C_b^{Y\times W}N_b^{X\times Z}\right)\\ &+ \frac{1}{\nu_b n_d(n_d-1)}\left(N_b^{X\times W}N_b^{Y\times Z}+N_b^{X\times Z}N_b^{Y\times W}\right), \qquad \text{(A.23)}\end{aligned}$$

where n_d is the number of splits and ν_b is the number of modes per bin, corrected for the effect of the window function. $C_b^{Y\times Z}$ is the theoretical power spectrum, and $N_b^{Y\times Z}$ is the noise power spectrum, given by $C_{b,\mathrm{auto}}^{Y\times Z} - C_{b,\mathrm{cross}}^{Y\times Z}$. The derivation of this expression is given in the Appendix. This does not include the non-Gaussian part of the covariance due to the effect of lensing, described in Benoit-Levy, Smith & Hu [4]. This is a subdominant part of the error for the noise levels we consider here, but introduces correlations between bins. We find that the analytic error bars agree with the 1σ dispersion from the simulations at the 15% level for $500 < \ell < 6000$, as shown in Figure A.6, indicating that all sources of leakage on these scales are subdominant. The error is dominated by cosmic variance at large scales, but at smaller scales is noise dominated. This agreement is promising and demonstrates the power of the pure estimator to recover the B-mode spectrum. In practice these spectra will be used to construct a likelihood for testing cosmological models, such that

$$-2\ln L = (\tilde{C}_b - C_b^{\mathrm{th}})^T Q^{-1} (\tilde{C}_b - C_b^{\mathrm{th}}). \tag{A.24}$$

The full covariance matrix, Q, can be estimated numerically from the simulations, or analytically, and the binned theory spectra C_b^{th} computed using bandpower window functions. The realistic likelihood will also include the lensing deflection spectrum, estimated from higher point statistics of the map, and appropriate cross-correlations.

A.6 Conclusions

A number of issues arise in the analysis of high resolution CMB polarization maps, one of the most significant being the leakage of E-mode into B-mode polarization due to observing a limited region of sky. In this appendix we have described a simple method for estimating the power spectrum in the flat sky approximation that minimizes this leakage. It draws on an existing all-sky method using a 'pure' estimator for the

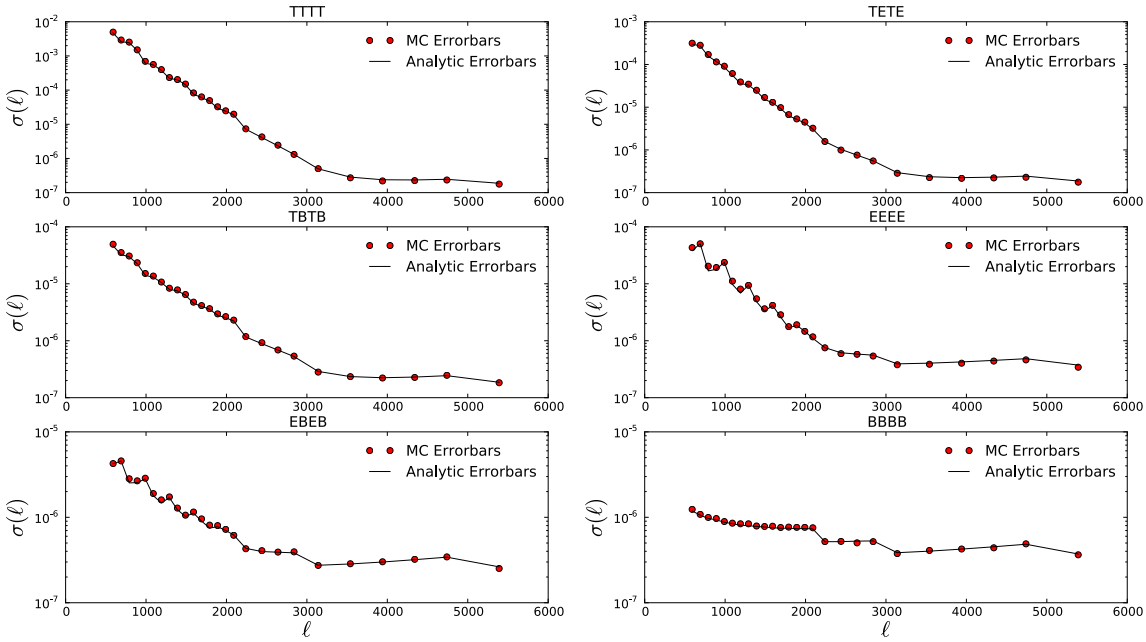

Figure A.6: Comparison between Monte Carlo scatter and analytic errors for each cross spectrum for one of the patches. They agree at the 15 per cent level for $500 < \ell < 6000$, indicating that all sources of leakage are subdominant for these modes, The analytic estimate does not include the non-Gaussian contribution from lensing, but the noise in our simulation is high enough for this effect to be subdominant.

B-mode, and simplifies the approach for the flat sky. This will be appropriate for small regions observed by current CMB experiments including ACTPol, SPTPol, and PolarBear. Using a suite of Monte Carlo simulations with realistic noise levels for upcoming experiments, we have demonstrated our ability to recover unbiased and quasi-optimal power spectra.

To test the robustness of any power spectrum method requires accurate simulations. The B-mode polarization spectrum at small angular scales is sourced solely from the gravitational lensing of the E-mode signal. We have shown how high resolution lensed CMB maps can be rapidly and accurately simulated using a hybrid approach between pixel remapping and interpolation in harmonic space. This method, which has advantages over the standard pixel-space interpolation approach, also has the potential to be extended to full sky spherical maps.

A.7 Acknowledgements

We thank David Spergel and Jeff McMahon for useful discussions and Mike Nolta for providing simulated coverage for the upcoming ACTPol experiment. SD acknowledges support from the David Schramm Fellowship at Argonne National Laboratory and the Berkeley Center for Cosmological Physics fellowship. Funding from ERC grant 259505 supports JD, TL and SN.

A.8 Error Calculation

Here we derive an analytic expression for the expected error bars on each of the cross-power spectrum, X, Y, W and Z stand for T, E and B. The variance is given by

$$\begin{aligned}\Theta_{bb}^{(X\times Y);(W\times Z)} &= \langle (C_b^{(X\times Y)} - \langle C_b^{(X\times Y)}\rangle)(C_b^{(W\times Z)} - \langle C_b^{(W\times Z)}\rangle)\rangle \\ &= \frac{1}{N}\frac{1}{\nu_b^2}\sum_{i,j,k,l}^{n_d}\sum_{\vec{\ell}\in b}\sum_{\vec{\ell}'\in b}\left(\left\langle X_{\vec{\ell}}^{*i}Y_{\vec{\ell}}^{j}W_{\vec{\ell}'}^{*k}Z_{\vec{\ell}'}^{l}\right\rangle - \left\langle C_b^{(iX\times jY)}\right\rangle\left\langle C_b^{(kW\times lZ)}\right\rangle\right) \\ &\times \ (1-\delta_{ij})(1-\delta_{kl}). \end{aligned} \tag{A.25}$$

The Kronecker symbol removes the auto power spectra. n_d represents the number of splits we are cross correlating and ν_b the number of modes in the annuli b. The general normalization is

$$N = \sum_{i,j,k,l}^{n_d}(1-\delta_{ij})(1-\delta_{kl}) = \sum_{i,j,k,l}^{n_d}(1-\delta_{ij}-\delta_{kl}+\delta_{ij}\delta_{kl}) = n_d^4 - 2n_d^3 + n_d^2. \tag{A.26}$$

Applying Wick's theorem,

$$\begin{aligned}\Theta_{bb}^{(X\times Y);(W\times Z)} &= \frac{1}{N}\frac{1}{\nu_b}\sum_{i,j,k,l}^{n_d}\left[\left\langle C_b^{(iX\times kW)}\right\rangle\left\langle C_b^{(jY\times lZ)}\right\rangle + \left\langle C_b^{(iX\times lZ)}\right\rangle\left\langle C_b^{(jY\times kW}\right\rangle\right] \\ &\times \ (1-\delta_{ij})(1-\delta_{kl}). \end{aligned} \tag{A.27}$$

We can decompose the estimated power spectrum into signal and noise, such that

$$\left\langle C_b^{(iX\times kW)} \right\rangle = C_b^{X\times W} + \delta_{ik} N_b^{X\times W}, \tag{A.28}$$

and then we can decompose $\Theta_{bb}^{(X\times Y);(W\times Z)}$ in three terms

$$\begin{aligned}
\Theta_{bb}^{(X\times Y);(W\times Z)} &= \frac{1}{\nu_b}\left(C_b^{X\times W} C_b^{Y\times Z} + C_b^{X\times Z} C_b^{Y\times W}\right) \\
+ \quad & \frac{1}{N}\frac{1}{\nu_b}\sum_{i,j,k,l}^{n_d}\left(C_b^{X\times W}\delta_{jl} N_b^{Y\times Z} + C_b^{Y\times Z}\delta_{ik} N_b^{X\times W} + C_b^{X\times Z}\delta_{jk} N_b^{Y\times W} + C_b^{Y\times W}\delta_{il} N_b^{X\times Z}\right) \\
\times \quad & (1-\delta_{ij})(1-\delta_{kl}) \\
+ \quad & \frac{1}{N}\frac{1}{\nu_b}\sum_{i,j,k,l}^{n_d}\left(\delta_{ik} N_b^{X\times W}\delta_{jl} N_b^{Y\times Z} + \delta_{il} N_b^{X\times Z}\delta_{jk} N_b^{Y\times W}\right) \times (1-\delta_{ij})(1-\delta_{kl}).
\end{aligned} \tag{A.29}$$

Finally, using

$$\sum_{i,j,k,l}^{n_d} \delta_{jl}\left(1-\delta_{ij}-\delta_{kl}+\delta_{ij}\delta_{kl}\right) = n_d^3 - 2n_d^2 + n_d, \tag{A.30}$$

and

$$\sum_{i,j,k,l}^{n_d} \delta_{ik}\delta_{jl}\left(1-\delta_{ij}-\delta_{kl}+\delta_{ij}\delta_{kl}\right) = n_d^2 - n_d, \tag{A.31}$$

the variance is given by

$$\begin{aligned}
\Theta_{bb}^{(X\times Y);(W\times Z)} &= \frac{1}{\nu_b}\left(C_b^{X\times W} C_b^{Y\times Z} + C_b^{X\times Z} C_b^{Y\times W}\right) \\
&+ \frac{1}{\nu_b n_d}\left(C_b^{X\times W} N_b^{Y\times Z} + C_b^{Y\times Z} N_b^{X\times W} + C_b^{X\times Z} N_b^{Y\times W} + C_b^{Y\times W} N_b^{X\times Z}\right) \\
&+ \frac{1}{\nu_b n_d(n_d-1)}\left(N_b^{X\times W} N_b^{Y\times Z} + N_b^{X\times Z} N_b^{Y\times W}\right).
\end{aligned} \tag{A.32}$$

References

[1] Ade P., et al., 2013, arXiv:1303.5075

[2] Austermann J., Aird K., Beall J., Becker D., Bender A., et al., 2012, Proc. SPIE, 8452, 84520E

[3] Bennett C., Larson D., Weiland J., Jarosik N., Hinshaw G., et al., 2012

[4] Benoit-Levy A., Smith K. M., Hu W., 2012, Phys.Rev., D86, 123008

[5] Bond J., Jaffe A. H., Knox L., 1998, Phys.Rev., D57, 2117

[6] Born M., Wolf E., 1980, Principles of Optics Electromagnetic Theory of Propagation, Interference and Diffraction of Light

[7] Bowyer J., Jaffe A. H., Novikov D. I., 2011, MasQU: Finite Differences on Masked Irregular Stokes Q, U Grids. Astrophysics Source Code Library

[8] Bunn E. F., 2011, PRD, 83, 083003

[9] Cao L., Fang L.-Z., 2009, Astrophys.J, 706, 1545

[10] Das S., Hajian A., Spergel D. N., 2009, Phys. Rev. D, 79, 083008

[11] Das S., Louis T., Nolta M. R., Addison G. E., Battistelli E. S., et al., 2013

[12] Das S., Marriage T. A., Ade P. A., Aguirre P., Amir M., et al., 2011, Astrophys.J., 729, 62

[13] Grain J., Tristram M., Stompor R., 2009, PRD, 79, 123515

[14] Grain J., Tristram M., Stompor R., 2012, PRD, 86, 076005

[15] Hinshaw G., et al., 2003, Astrophys.J.Suppl., 148, 135

[16] Kamionkowski M., Kosowsky A., Stebbins A., 1997, Phys.Rev., D55, 7368

[17] Kermish Z., Ade P., Anthony A., Arnold K., Arnold K., et al., 2012

[18] Lewis A., 2005, Phys.Rev., D71, 083008

[19] Lewis A., Challinor A., Turok N., 2002, PRD, 65, 023505

[20] Niemack M., Ade P., Aguirre J., Barrientos F., Beall J., et al., 2010, Proc. SPIE, 7741, 77411S

[21] Seljak U., Zaldarriaga M., 1997, Phys.Rev.Lett., 78, 2054

[22] Smith K. M., 2006, Phys.Rev., D74, 083002

[23] Smith K. M., Zaldarriaga M., 2007, Phys.Rev., D76, 043001

[24] Story K., Reichardt C., Hou Z., Keisler R., Aird K., et al., 2012

[25] Zhao W., Baskaran D., 2010, PRD, 82, 023001

Appendix B

Methods for CMB Lensing Estimation without Sensitivity to Foregrounds

B.1 Lensing Biases from Foregrounds

Foreground sources such as SZ clusters, radio sources and dusty sources all induce signal into CMB temperature maps. As lensing estimation uses a quadratic combination of temperature modes, the foregrounds signals persist in the estimated lensing map, albeit in an altered form due to their processing through the lensing estimator. This contamination can cause biases in both CMB lensing auto- and cross-correlations (see e.g. Chapter 3 or [1, 2, 3, 4, 5]). In both cases, the source of these biases is the fact that foreground sources introduce a spurious part into the temperature four-point-function (relevant for measurements of the lensing power spectrum) and the galaxy/tracer-temperature-temperature three-point function (relevant for cross correlation).

More concretely, for the quadratic estimator

$$\hat{\phi}(\mathbf{L}) = \int \frac{d^2\mathbf{l}}{(2\pi)^2} f(\mathbf{l},\mathbf{L}) T(\mathbf{l}) T(\mathbf{L}-\mathbf{l}), \tag{B.1}$$

the foreground sources, which we take to contribute an amount $P(\hat{\mathbf{n}})$ to the observed temperature map, cause a bias in lensing power spectrum measurements of

$$\int \frac{d^2\mathbf{l}}{(2\pi)^2} \frac{d^2\mathbf{l}'}{(2\pi)^2} f(\mathbf{l},\mathbf{L}) f(\mathbf{l}',\mathbf{L}) \ \langle P^*(\mathbf{l}) P^*(\mathbf{L}-\mathbf{l}) P(\mathbf{l}') P(\mathbf{L}-\mathbf{l}') \rangle \tag{B.2}$$

plus additional terms consisting of four-point functions involving both P and the true CMB temperature T.

Similarly, foreground sources can bias cross-correlations of a mass-tracer density field $g(\hat{\mathbf{n}})$ with CMB lensing by

$$\int \frac{d^2\mathbf{l}}{(2\pi)^2} f(\mathbf{l},\mathbf{L}) \ \langle P(\mathbf{l}) P(\mathbf{L}-\mathbf{l}) g^*(\mathbf{L}) \rangle \tag{B.3}$$

B.2 Immunizing the Lensing Estimator to Foreground Contamination

B.2.1 Poisson Foregrounds

For many contaminants (e.g. radio sources or the cosmic infrared background), a dominant form of these contamination four- and three-point functions are the Poisson or 1-halo contributions. These contributions are also the simplest to treat analytically as they are approximately constant (C or D respectively) over relevant scales, i.e.

$$\langle P(\mathbf{l}) P(\mathbf{L}-\mathbf{l}) g^*(\mathbf{L}) \rangle_{\rm conn} = C; \quad \langle P^*(\mathbf{l}) P^*(\mathbf{L}-\mathbf{l}) P(\mathbf{l}') P(\mathbf{L}-\mathbf{l}') \rangle_{\rm conn} = D. \tag{B.4}$$

The fact that Poisson-distributed fields have a constant four- or three-point function can be seen by considering the constant Fourier transform of random distributions of delta functions.

We would like to modify the existing lensing reconstruction procedure so that the biases from Poisson foregrounds are removed. To remove biases in cross-correlations and reduce the biases in auto-correlations, it can be seen (by setting the correlation functions in Eqs. (B.2) and (B.3) to a constant) that the following simple foreground immunization condition must be satisfied by the reconstruction weight function f:

$$F[f] \equiv \int \frac{d^2\mathbf{l}}{(2\pi)^2} f(\mathbf{l}, \mathbf{L}) = 0 \tag{B.5}$$

We now rederive a modified lensing estimator with a new weight function f, which has the least possible variance given that it must now satisfy the immunization condition. This additional condition can easily be incorporated in the estimator variance-minimization formalism described in Chapter 2.

In Chapter 2, we show that the variance of the conventional quadratic estimator for the lensing potential is given by

$$V[f](\mathbf{L}) \;=\; 2 \int \frac{d^2\mathbf{l}}{(2\pi)^2} f^2(\mathbf{l}, \mathbf{L}) C_l C_{|\mathbf{L}-\mathbf{l}|} \tag{B.6}$$

and that the requirement that the estimator be unbiased implies that

$$I[f] \equiv \int \frac{d^2\mathbf{l}}{(2\pi)^2} f(\mathbf{l}, \mathbf{L}) K(\mathbf{l}, \mathbf{L}) = 1 \tag{B.7}$$

where

$$K(\mathbf{l}, \mathbf{L})\phi(\mathbf{L}) = \left[(\mathbf{L} - \mathbf{l}) \cdot \mathbf{L}\; \tilde{C}_{\mathbf{l}-\mathbf{L}} + \mathbf{l} \cdot \mathbf{L}\; \tilde{C}_l \right] \phi(\mathbf{L}) \tag{B.8}$$

and tildes denote unlensed, noiseless power spectra.

To derive the estimator in the absence of foregrounds, we calculated the estimator weight function f by minimizing $V[f] - \lambda I[f]$. We now derive a modified f which reduces foreground sensitivity by adding a new Lagrange multiplyer μ for the foreground immunization condition and minimizing

$$V[f] - \lambda I[f] - \mu F[f] \tag{B.9}$$

with the additional constraint equations $I = 1;\ F = 0$.

We obtain the following expression for the minimum variance f which still satisfies the foreground immunization condition:

$$f(\mathbf{l}, \mathbf{L}) = \frac{K(\mathbf{l}, \mathbf{L}) - Q(\mathbf{L})}{2C_\ell C_{|\mathbf{L}-\mathbf{l}|}} H(L) \tag{B.10}$$

where

$$H(L) = \left[\int \frac{d^2\mathbf{l}}{(2\pi)^2} \frac{(K(\mathbf{l}, \mathbf{L}) - Q(\mathbf{L}))K(\mathbf{l}, \mathbf{L})}{2C_\ell C_{|\mathbf{L}-\mathbf{l}|}} \right]^{-1} \tag{B.11}$$

and

$$Q(\mathbf{L}) = \frac{\int \frac{d^2\mathbf{l}}{(2\pi)^2} \frac{K(\mathbf{l},\mathbf{L})}{2C_\ell C_{|\mathbf{L}-\mathbf{l}|}}}{\int \frac{d^2\mathbf{l}}{(2\pi)^2} \frac{1}{2C_\ell C_{|\mathbf{L}-\mathbf{l}|}}} \tag{B.12}$$

This expression can be easily explained. Neglecting for a moment the normalization factor H, in this estimator one is simply subtracting a term $Q/2C_\ell C_{|\mathbf{L}-\mathbf{l}|}$ from the filter function, i.e. a constant in $\mathbf{l}$ over inverse power spectrum weights. This is exactly the optimal estimator to estimate the level of a constant three-point function. Essentially the additional term is just an estimator for the level of the connected/constant part multiplied by an integral (the numerator of Q) giving the response of the usual lensing estimator to a constant three point function; i.e. this expression estimates the level of contamination, calculates its effect on the usual lensing estimator and subtracts this contamination off from the original estimate. The normalization is also modified; this is due to the fact that the estimator for the constant three-point

level also will pick up some contribution from the lensing signal. This contribution is absorbed in the modified normalization factor in order to keep the estimator unbiased.

We note that our formalism recovers, through a different derivation, the same estimator as the "bias-hardened" approach of [6] applied to Poisson foregrounds.

B.2.2 General Foregrounds

We now consider CMB lensing foregrounds which are not simply Poisson distributed, but instead have more complicated (yet reasonably well-understood) bispectra or trispectra, such as clustered point sources or, to a lesser extent, the SZ effect. For a more general bispectrum $B(\mathbf{l}, \mathbf{L})$, we now require the following constraint equation to be satisfied to ensure that the lensing estimator has no response to foregrounds in cross-correlation:

$$F_B[f] \equiv \int \frac{d^2\mathbf{l}}{(2\pi)^2} f(\mathbf{l}, \mathbf{L}) B(\mathbf{l}, \mathbf{L}) = 0, \tag{B.13}$$

Repeating the previous calculation with this new constraint equation, we obtain a similar but more general result:

$$f_B(\mathbf{l}, \mathbf{L}) = \frac{K(\mathbf{l}, \mathbf{L}) - B(\mathbf{l}, \mathbf{L}) Q(\mathbf{L})}{2 C_\ell C_{|\mathbf{L}-\mathbf{l}|}} H(L) \tag{B.14}$$

where

$$H_B(L) = \left[\int \frac{d^2\mathbf{l}}{(2\pi)^2} \frac{(K(\mathbf{l}, \mathbf{L}) - B(\mathbf{l}, \mathbf{L}) Q(\mathbf{L})) K(\mathbf{l}, \mathbf{L})}{2 C_\ell C_{|\mathbf{L}-\mathbf{l}|}} \right]^{-1} \tag{B.15}$$

and

$$Q_B(\mathbf{L}) = \frac{\int \frac{d^2\mathbf{l}}{(2\pi)^2} \frac{B(\mathbf{l},\mathbf{L}) K(\mathbf{l},\mathbf{L})}{2 C_\ell C_{|\mathbf{L}-\mathbf{l}|}}}{\int \frac{d^2\mathbf{l}}{(2\pi)^2} \frac{B^2(\mathbf{l},\mathbf{L})}{2 C_\ell C_{|\mathbf{L}-\mathbf{l}|}}} \tag{B.16}$$

References

[1] Smith, K. M., Zahn, O., & Doré, O. 2007, Phys. Rev. D, 76, 043510

[2] Hirata, C. M., Ho, S., Padmanabhan, N., Seljak, U., & Bahcall, N. A. 2008, Phys. Rev. D, 78, 043520

[3] van Engelen, A., Keisler, R., Zahn, O., et al. 2012, arXiv:1202.0546

[4] Bleem, L. E., van Engelen, A., Holder, G. P., et al. 2012, arXiv:1203.4808

[5] Planck Collaboration, Ade, P. A. R., Aghanim, N., et al. 2013, arXiv:1303.5077

[6] Namikawa, T., Hanson, D., & Takahashi, R. 2013, Mon. Not. R. Astron. Soc, 431, 609